

RADIATIVE TRANSFER IN THE ATMOSPHERES
OF VENUS AND THE EARTH

A Dissertation

by

CHARLES NATHAN ADAMS

Submitted to the Graduate College of
Texas A&M University in
partial fulfillment of the requirement for the degree of
DOCTOR OF PHILOSOPHY

December, 1974

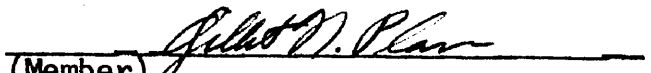
Major Subject: Physics

RADIATIVE TRANSFER IN THE ATMOSPHERES
OF VENUS AND THE EARTH

A Dissertation
by
CHARLES NATHAN ADAMS

Approved as to style and content by:

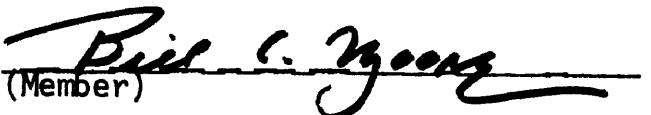

(Chairman of Committee)


(Member)


(Head of Department)


(Member)


(Member)


(Member)

December, 1974

437682

ABSTRACT

Radiative Transfer in the Atmospheres
of Venus and the Earth

(December, 1974)

Charles Nathan Adams,

B. S., Texas Tech University;

M. S., North Texas State University;

Directed by: Dr. George W. Kattawar

The flux and polarization reflected from a spherically symmetric planetary atmosphere is calculated by the Monte Carlo technique. Spherical geometry is used throughout the calculation with no plane-parallel approximations. The scattering angle for the photons is chosen from an appropriate single-scattering function calculated from Mie theory. The photons are followed through all orders of multiple scattering. Models considered for the Venus atmosphere include several single-layered models with various particle size distributions and one multilayered model. The results, when compared with experimental observations, suggest that the clouds are composed of particles having a mean radius of the order of $1\ \mu$ and a refractive index in the range from 1.45-1.6. Differences between theory and experiment may result from aspherical particles and a variation of the composition and size distribution of the particles with height in the atmosphere.

The radiance and color of the twilight sky are calculated for single scattered radiation with the use of spherically symmetric models of the earth's atmosphere. Spherical geometry is used throughout the calculations with no plane parallel approximations. Refraction effects are taken into account through fine subdivision of the atmosphere into spherical shells of fixed index of refraction. Snell's law of refraction is used to calculate a new direction of travel each time that a photon traverses the interface between layers. Five different models of the atmosphere were used: a pure molecular scattering atmosphere; molecular atmosphere plus ozone absorption; three models with aerosol concentrations of 1, 3, and 10 times normal together with molecular scattering and ozone absorption. The results of the calculations are shown for various observation positions and local viewing angles in the solar plane for wavelengths in the range of 0.40 to 0.75 μ .

ACKNOWLEDGEMENTS

I would like to express my appreciation to Professor George W. Kattawar, my research advisor, for his enduring patience and constructive advice throughout this entire research project. Also to Professor Gilbert N. Plass, Chairman of the Department of Physics and co-advisor, for his time and assistance throughout this research project. Their personal advice and research funding made this project possible. I also wish to thank the Data Processing Centers of Texas A&M University, The University of Texas at Austin, and the National Center of Atmospheric Research, Boulder, Colorado for the use of their facilities in finishing the calculations.

CONTENTS

Chapter	Page
I Introduction.	1
II The Method of Solution.	6
a) The Model Atmospheres	7
b) Detector Bands.	9
III Atmospheric Parameters.	12
a) Optical Thickness	12
b) Extinction Coefficients	13
c) Scattering and Absorption Cross-Section	14
d) Scattering Functions and Phase Matrix	15
e) Planet Surface.	15
IV Computational Techniques.	17
a) Photon History.	18
b) Generating Desired Distribution from a Uniform Distribution.	20
c) Point Distribution Method	21
d) Generation by Inversion	25
e) Photon Selection.	26
f) Pathlength Selection.	29
g) Tau Calculations.	31
h) Outgoing Photon	31
i) Incoming Photon	34
j) Determination of the Scattering Point	35
V Mie Scattering.	38

VI	Cloud Models.	39
	a) Single Layer: Model-1 (M-1)	39
	b) Single Layer: Model-2 (M-2)	47
	c) Single Layer: Model-3 (M-3)	56
	d) Single Layer: Model-4 (M-4)	61
	e) Three Layers: Model-5 (M-5)	65
VII	Conclusion.	71
VIII	Twilight.	74
IX	Computational Techniques.	76
X	Atmospheric Models.	82
XI	Calculated Radiance	89
XII	Chromaticity.	103
	a) Model A. Molecular atmosphere without ozone	103
	b) Model B. Molecular atmosphere with ozone.	111
	c) Model C. Molecular atmosphere, ozone, normal aerosol amount.	114
	d) Model D. Molecular atmosphere, ozone, three times normal aerosol amount	117
	e) Model E. Molecular atmosphere, ozone, ten times normal aerosol amount	119
XIII	Conclusions	121
XIV	Bibliography.	122

LIST OF TABLES

Table		Page
I.	Single Scattering Albedo ω_0 and Computed Bond Albedo for Various Models.	43
II.	Colorimetry Values for Model A.	104
III.	Colorimetry Values for Model B.	105
IV.	Colorimetry Values for Model C.	106
V.	Colorimetry Values for Model D.	107
VI.	Colorimetry Values for Model E.	108

LIST OF FIGURES

Figure	Page
1. Comparison of Monte Carlo solutions and the plane-parallel solution integrated over the visible crescent.	4
2. Same as Figure 1 with $\tau=1.0$	5
3. Planet Atmosphere system with local and fixed coordinate systems.	8
4. Point rejection technique showing that point \bar{R}_j would be rejected from the sequence	22
5. Selection and determination of incident point on the atmosphere	27
6. Geometry for an outgoing photon	33
7. Geometry for an incoming photon	36
8. Single-scattering phase function for model M-1 at 0.55μ with particle size distribution $n(r) \propto r^6 e^{-6r}$ and refractive index $N=(1.50,0.00)$	40
9. Degree of polarization for model M-1 at 0.55μ	41
10. Comparison of the degree of polarization versus phase angle for model M-1 with experimental observations for $\lambda=0.55 \mu$	44
11. Comparison of the least-squares visual magnitude as measured by Knuckles et. al. (1961) and the Monte Carlo solutions (histogram) for model M-1 at 0.55μ	46
12. Same as Figure 8 but for 0.34μ	48
13. Same as Figure 9 but for 0.34μ	49
14. Same as Figure 10 with a 6% admixture of Rayleigh scattering at 0.34μ	50

15.	Single scattering phase function for model M-1 at 0.99 μ	51
16.	Degree of polarization for model M-1 at 0.99 μ	52
17.	Monte Carlo results for model M-1 at 0.99 μ	53
18.	Monte Carlo results for model M-2 at 0.34 μ with 6% Rayleigh	54
19.	Monte Carlo results for model M-2 at 0.55 μ	55
20.	Monte Carlo results for model M-2 at 0.99 μ	57
21.	Monte Carlo results for model M-3 at 0.34 μ	58
22.	Monte Carlo results for model M-3 at 0.55 μ	59
23.	Monte Carlo results for model M-3 at 0.99 μ	60
24.	Monte Carlo results for model M-4 at 0.34 μ	62
25.	Monte Carlo results for model M-4 at 0.55 μ	63
26.	Monte Carlo results for model M-4 at 0.99 μ	64
27.	Monte Carlo results for model M-5 at 0.34 μ	67
28.	Monte Carlo results for model M-5 at 0.55 μ	68
29.	Monte Carlo results for model M-5 at 0.99 μ	70
30.	Geometry of direct solar flux to scattering point on line of sight and then to observer on the surface of the earth	78
31.	Optical thickness through the entire atmosphere in a vertical direction as a function of wavelength for Models A-E.	84

32. Shadow height in km as a function of θ , the zenith angle of observation. The solar horizon is at the right and the antisolar horizon at the left. The dashed curves are calculated without refraction, while the solid curves include the effect of the refraction of the light rays by the earth's atmosphere 85
33. Transmission from outside atmosphere to perigee point. Curves are shown for Models A, C, D, and E (the curve for Model B is the same as that for Model A on the scale of the figure) and for $\lambda = 0.45 \mu$ 87
34. Same as Figure 33 except $\lambda = 0.75 \mu$ 88
35. Radiance as a function of wavelength (microns) for Model A and $\theta_0 = 90^\circ$. The zenith angle of the direction of observation in the solar half plane is marked on each curve 90
36. Radiance as a function of wavelength (microns) for Model A and $\theta_0 = 90^\circ$. The zenith angle of the direction of observation in the antisolar half plane is marked on each curve 91
37. Radiance for Model B and $\theta_0 = 90^\circ$ 93
38. Radiance for Model C and $\theta_0 = 90^\circ$ 94
39. The differential radiance per kilometer (measured along the slant path) as a function of the vertical height to the scattering volume measured along the earth's local radius through the infinitesimal volume. The results are for Model C, $\theta_0 = 90^\circ$, and $\lambda = 0.4 \mu$. Results are shown for $\theta = 85^\circ, 70^\circ, 40^\circ, 0^\circ, -40^\circ, -70^\circ, -85^\circ$ (negative values are in the antisolar half plane). 95
40. Radiance for Model B and $\theta_0 = 96^\circ$ 99
41. Radiance for Model C and $\theta_0 = 96^\circ$ for solar half plane 100
42. Radiance for Model C and $\theta_0 = 96^\circ$ for antisolar half plane 101

49. Chromaticity diagram for Model C and $\Theta_0=96^\circ$116
50. Chromaticity diagram for Model D and $\Theta_0=92^\circ$
and 96°118
51. Chromaticity diagram for Model E and $\Theta_0=92^\circ$
and 96°120

I. INTRODUCTION

Lyot (1929) made the first high precision polarimetric measurements of the planet Venus. More recently Dollfus (1955, 1966) and Coffeen and Gehrels (1969) have continued this work. The degree of polarization has been measured for various wavelengths from 0.34μ to 0.99μ . This data narrowly restricts the allowed optical properties of the cloud constituents. Coffeen (1969) using contour maps of single scattered polarization from spherical particles concludes that the particles have very little absorption, with real refractive indices between 1.43 and 1.55 and mean diameters of $2.5 \pm 0.5 \mu$. These conclusions are based primarily on single scattering calculations.

The recent work of Hansen and Arking (1971) includes multiple scattering. They use the plane parallel solutions obtained by the doubling method and then integrate them over the visible crescent. They obtain good agreement with observation using a size distribution given by

$$n(r) \propto r^6 e^{-br} \quad (1)$$

where r denotes the particle radius and the modal radius r_m is given by

$$r_m = G/b \quad (2)$$

They use a parameter \bar{r} which is the radius averaged over the size distribution with the cross section used as a weighting factor. With a value of $\bar{r}=1.1\mu$ and a real refractive index of 1.44 at 0.99μ , 1.45 at 0.55μ , and 1.46 at 0.36μ they were able to fit the observations quite well at these three wavelengths. Although the index of refraction may vary slightly with wavelength in this region, it is not permissible to assume the same value for \bar{r} at each wavelength since this actually corresponds to the use of a different particle size distribution at each wavelength. The real atmosphere has only one particle size distribution (at least at each altitude); \bar{r} varies with wavelength, whereas Hansen and Arking assumed that it is constant. The agreement between their results and experimental values would not have been as good if they had used the same particle size distribution at each wavelength.

The development of a general purpose computer code is to be described for the purpose of calculating the flux and polarization for all orders of multiple scattering. The photon is followed in a spherical coordinate system so that all effects due to the spherical geometry of the planet are treated exactly. For each atmospheric model the same index of refraction and particle size distribution is used at each wavelength. Models considered for the Venus atmosphere include several single layered models with various particle size distributions and one multilayered model.

The resulting program was tested by a comparison with the results of Adams and Kattawar (1970) and Kattawar and Adams (1971) for the

degree of polarization of the light scattered by a plane-parallel atmosphere with a Rayleigh phase matrix; these results were then integrated over the visible crescent. These results, computed from the equations of radiative transfer, are compared with the Monte Carlo solutions in Figure 1 for an optical depth $\tau=0.2$ with ground albedos $A=0.0$ and 0.55 and for an optical depth $\tau=1.0$ with ground albedos $A=0.0$ and 0.8 as shown in Figure 2. As can be seen from the figures, the agreement is quite good. The Bond albedos also agreed to two significant figures. The fluxes calculated by the two methods also agreed well, but are not presented here since the degree of polarization is a much more sensitive test.

The polarization computed from results for a plane-parallel atmosphere integrated over the visible crescent appears to agree at all phase angles with the Monte Carlo results for the spherical geometry of the Venus atmosphere when a Rayleigh phase function is used. Such agreement is not anticipated for aerosol phase functions with strong forward scattering, particularly for phase angles greater than 140° . At these phase angles photons incident on the atmosphere at an angle near the horizon undergo fewer collisions within the spherical atmosphere than within the equivalent integrated plane-parallel atmosphere because of the large probability of small angle aerosol scattering. Thus calculations must be made in a spherical geometry for large phase angles when there is aerosol scattering.

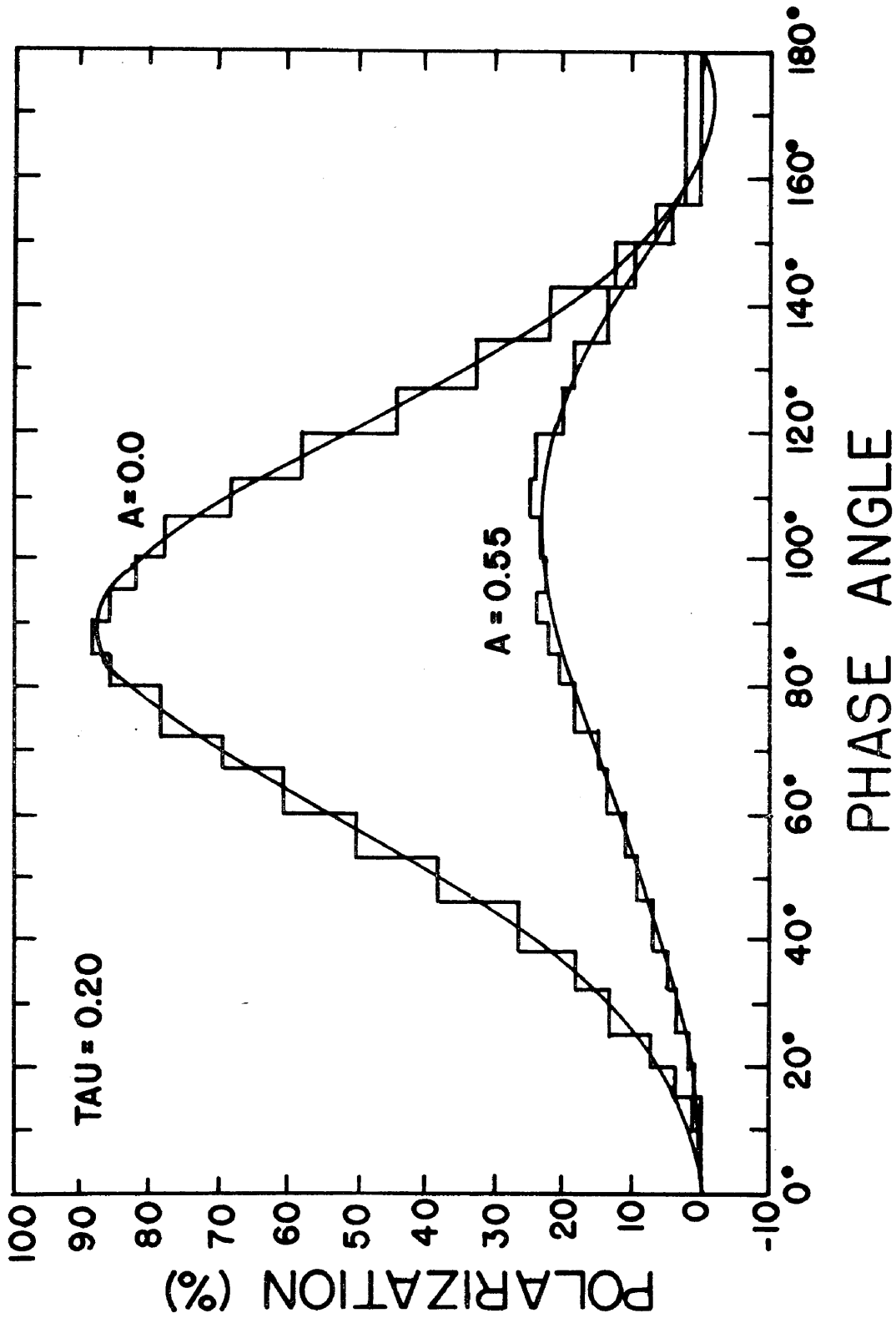


Figure 1 - Comparison of Monte Carlo solutions and the plane-parallel solution integrated over the visible crescent

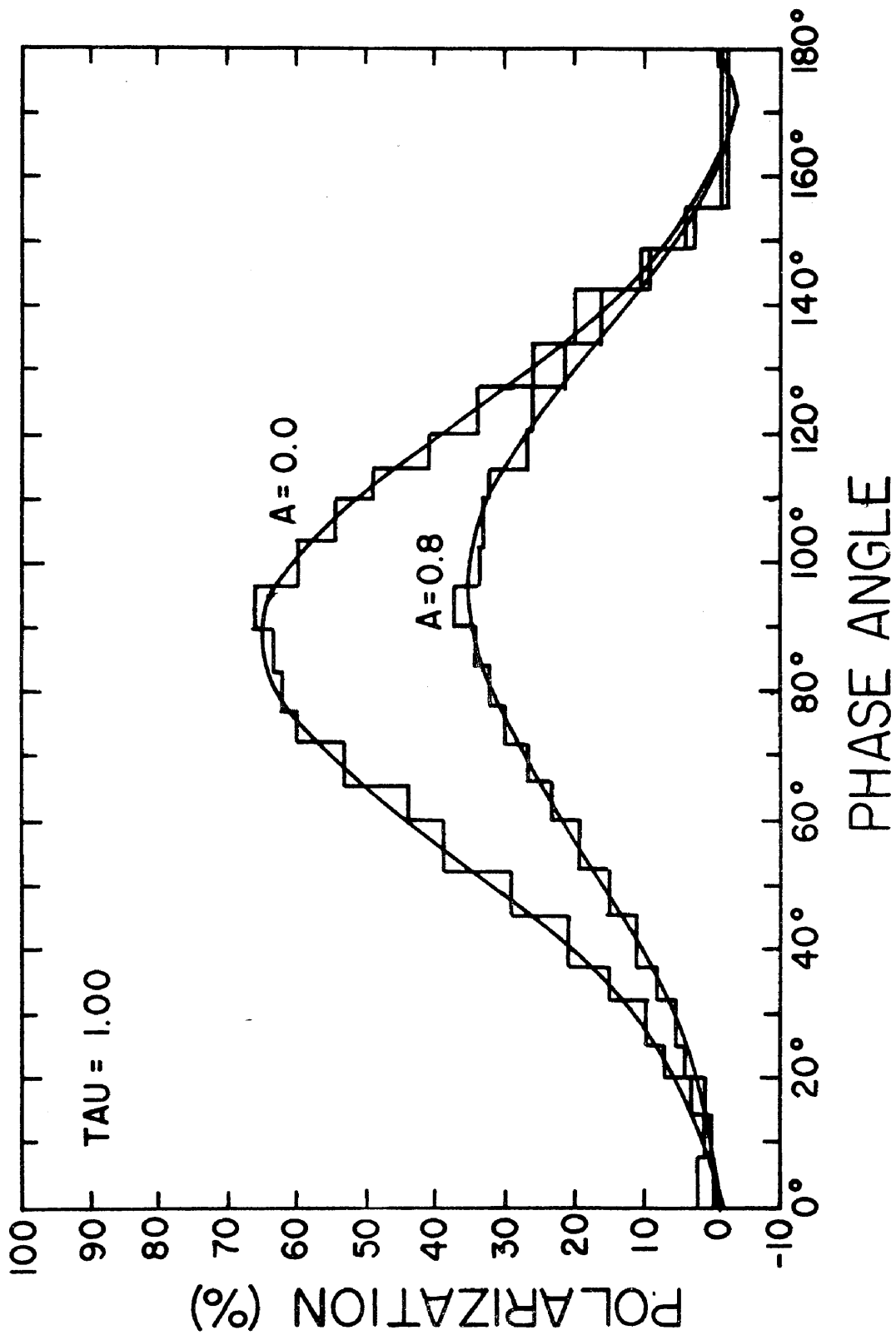


Figure 2 - Same as Figure 1 with $\tau = 1.0$

II. THE METHOD OF SOLUTION

The Monte Carlo technique was chosen for the solution of light transport problems in real spherical atmospheres since it had already been used successfully by Kattawar and Plass (1968,1971) and Plass and Kattawar (1969,1970) to calculate the flux density and polarization reflected and transmitted in plane-parallel planetary atmospheres. Both the plane-parallel and spherical geometry approaches have relative advantages.

The plane-parallel approach has the advantage of producing a simpler mathematical representation with correspondingly simpler forms of solutions as opposed to the results of the spherical approach. However, the plane-parallel model is representative of reality only over small surface areas of a planet with restricted viewing angles at the surface and levels within and above the atmosphere. The plane-parallel approach is unable to describe some of the more interesting effects of atmospheric radiation due to spherical geometry as is encountered in twilight phenomena. The spherical approach provides a more realistic model, capable of including most atmospheric effects, both reflected and transmitted. If Monte Carlo techniques are applied, the complexity of the model is limited primarily by practicality. Even using the Monte Carlo method, the spherical problems of radiative transfer are very difficult to solve.

a) The Model Atmospheres

The model atmospheres, to be considered in the problems of the earth and Venus atmospheres, are taken to be spherical shells concentric with the planet. The planet radius is in kilometers, although any system of units may be used for convenience. The atmospheric radii are also given in the same units with the total extent of the planetary atmosphere determined by practicality of the physical and optical parameters known or calculated for the atmospheric model to be studied. Physical units are used throughout the calculations, although arbitrary units may be used as long as the proper ratios of the physical dimensions involved are preserved.

Figure 3 illustrates the upper hemisphere of the planet-atmosphere system with the atmospheric thickness exaggerated for clarity.

All coordinates and direction cosines are determined relative to a coordinate system fixed within the planet with origin located at the planet center. This system is also illustrated in Figure 3. Points within the atmosphere or on the surface of the planet are specified in Cartesian coordinates relative to the fixed system.

The incident solar flux upon the planet and atmosphere is parallel to the fixed z-axis with direction cosine of unity relative to this axis. It is assumed parallel, unpolarized, and of unit strength to closely approximate the solar flux from the sun.

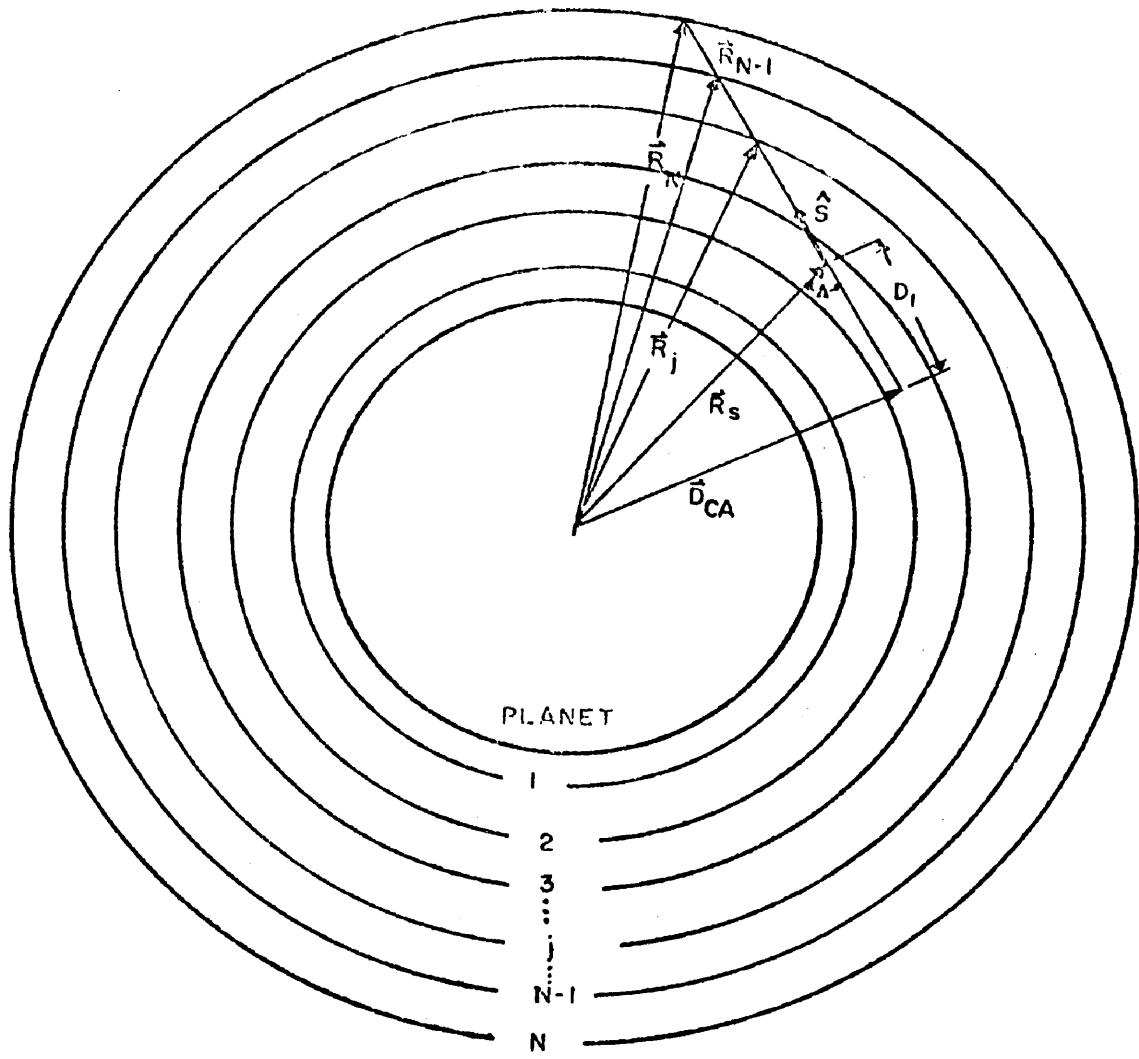


Figure 3 - Planet atmosphere system

The atmospheric geometry is such that the spherical atmosphere is divided into a number of concentric spherical zones which are analogous to the parallel planes of the plane-parallel model of Kattawar and Plass (1966).

Each atmospheric zone is referenced by the index of the outer-most radius of the zone. That is, the i -th zone contains all points of radius r such that

$$R_{i-1} < r < R_i \quad (3)$$

where R_j is the radius of the j -th zone. The planet surface, a sphere with radius R_p , is considered the inner boundary of the first zone. The outer-most zone is considered to have the radius of the planet atmosphere, R_A .

All atmospheric zones have some associated optical thickness τ'_i and physical thickness t_i . For a total atmospheric optical thickness τ , divided into N zones, it is required that

$$\tau = \sum_{i=1}^N \tau'_i \quad (4)$$

All atmospheric parameters are considered constant within each zone, but may vary from one zone to the next.

b) Detector Bands

For atmospheric problems requiring solutions of reflected light intensities and polarizations at the upper boundary of the atmosphere, the outer rim of the atmosphere may be divided into a number of detector bands. The outer rim of the atmosphere is

divided into NDET bands. These bands are of equal width in μ_0 , where μ_0 is the cosine of the nadir angle θ_0 . Equal spacing in μ_0 ensures that the detector bands have equal areas. The assumption of azimuthal symmetry relative to the incident direction requires that all points with the same ϕ in a given detector band are equivalent. Although those with different ϕ are not equivalent within a given band, practicality requires that they be treated as such.

The detector bands allow determination of the angular dependence of emergent intensities on the planet nadir angle θ_0 , where θ_0 is shown in Figure 3. Any reasonable number of bands may be used and is limited by current internal program values.

To determine the angular dependence of the emergence, local coordinate systems are constructed at these points. In these local systems the angular dependencies may be ascertained.

A local coordinate system with origin at the detector point is shown in Figure 3. The local $x'y'$ plane is tangent to the atmospheric rim, and the z' axis is perpendicular to the plane in an outward direction. The x' -axis is required to be in a plane containing the radius vector to the point of emergence and the planet z -axis. This x' -axis is so directed that the incident flux makes a local angle of zero relative to it.

It is impractical to determine the angular dependence in the local system for all possible angles of emergence. The local

system is divided into a number of solid angles for which all photons passing through the corresponding solid angle are treated as equivalent.

The range of Θ values for each solid angle of the local detector is determined by the range of the cosine of the local maximum zenith angle, $\Theta_{i,max}$, and the cosine of the local minimum zenith angle, $\Theta_{i,min}$, where i is the corresponding number for the angular bin. The range of the ϕ bins is determined by the local azimuth angle. As azimuthal symmetry is assumed for the model atmosphere, no distinction need be made as to which side of the x' -axis the bins lie.

In a similar manner, detectors may be specified on the surface of the planet to determine values of transmitted and reflected light parameters.

III. ATMOSPHERIC PARAMETERS

In the solution of any radiative transfer problem, it is necessary to completely describe the atmospheric parameters essential to account for the physical process of light transport phenomena. This chapter will characterize these parameters necessary for any model atmosphere.

a) Optical Thickness

One optical property of the transport medium of the atmosphere is defined in terms of a parameter called the optical thickness. The optical thickness, $\tau(s, s')$, along a straight line connecting points s and s' in an optical material is defined by Chandrasekhar (1960) by the equation

$$\tau(s, s') = \int_s^{s'} K \rho \, ds \quad (5)$$

where K is the mass absorption and scattering coefficient, ρ the density of the medium, and ds the element of integration along the line connecting points s and s' . The product $K\rho$ shall be combined to form a single coefficient termed the extinction coefficient, β , thus

$$\tau(s, s') = \int_s^{s'} \beta(h) \, dh \quad (6)$$

where $\beta(h)$ is the extinction coefficient at the point h .

The total optical atmospheric depth of the planetary atmosphere, τ , may be specified as any reasonable value. For simulation of real physical conditions in the earth's atmosphere, the optical thickness may range from a value of less than one-tenth to over a hundred. The model atmospheres of Venus have values on the order of fifty. A more quantitative discussion will be given later on the selection and determination of the values to be used in the calculations for each atmosphere.

b) Extinction Coefficients

The atmospheric extinction coefficients may be determined for an ideal atmosphere by the method of Collins and Wells (1966) or from tables of measured values such as those of Eltermann (1968).

Once the total atmospheric τ is selected, the extinction coefficient for each atmospheric zone may be computed in the following manner. Let h be the vertical height above the planet surface, and $\beta(h)$ the extinction coefficient at h . The dependence of β on h is approximated for an ideal atmosphere by

$$\beta(h) = \alpha e^{-Bh} \quad (7)$$

where α is determined by the total tau, τ , and B is a constant determining the height dependence of the atmospheric density. The reciprocal of B is called the scale height of the atmosphere.

Alpha is determined by the requirement that

$$\tau = \int_0^{h'} \alpha e^{-Bh} dh, \quad (8)$$

where h' is the maximum height of the atmosphere, and B is

positive. This has the solution

$$\tau = -(\alpha/B) e^{-Bh'} + (\alpha/B) \quad (9)$$

For large h' , the value of α may be closely approximated by

$$\alpha = B\tau. \quad (10)$$

The extinction coefficient for the i -th zone, β_i , may be determined by picking the $\beta(h)$ within each zone such that

$$\tau = \sum_{i=1}^N \beta_i t_i \quad (11)$$

is satisfied, where t_i is the physical thickness of each zone and N is the number of zones for the model atmosphere. Note that the units for the β_i , $i=1,2,\dots,N$ are length^{-1} .

The extinction coefficients for each zone of the earth atmospheric model were determined from tables of measured values by Eltermann (1968). Since no such measurements exist at the present for the atmosphere of Venus, these parameters are determined by the previously outlined method for an ideal atmosphere with a total atmospheric tau of fifty and with a parametric value of one-tenth for B . The total physical thickness of the Venus atmosphere was taken to be ninety kilometers with a planet radius of 6050 kilometers.

c) Scattering and Absorption Cross-Sections

The scattering and absorption cross-sections for Rayleigh and Mie scattering events within a planetary atmosphere are necessary for calculation of emergent and transmitted radiation within the model atmospheres. For the atmosphere of Venus, these parameters

are estimated and the calculations are performed for theoretical values of measured flux and polarization of the emergent radiation from the atmosphere as it would be measured on the earth. The results of these calculations are then compared with the physical measurements of Coffeen and Gehrels (1969) and appropriate adjustments are made to the atmospheric parameters to obtain improved agreement.

d) Scattering Functions and Phase Matrix

The scattering functions and phase matrices for aerosols are those computed by a program using Mie theory for analytical particle size distributions with a given complex index of refraction. This code was developed by Kattawar and Plass (1967a,1967b) and modified by C. N. Adams for rapid display of polarization phase curves for analysis of single scattering and prediction of multiple scattering results.

The nature of aerosols and their distributions will be discussed in detail in the models for the atmospheres of Venus and the earth.

e) Planet Surface

The optical properties of the planet's surface may also be taken into account for computations involving real or ideal atmospheres. The most used model for a planetary surface is the Lambert surface for which the reflected incident radiation is distributed with equal intensity in all directions. This type of

surface was used in the initial calculations for an ideal Rayleigh atmosphere. For optically thick atmospheres, or in the case of Venus, the properties of the ground have very little effect upon the reflected light from the atmosphere. A ground albedo of zero was used, i.e., the ground was assumed to be a perfect absorber of radiation for all wavelengths, in the Venus calculations in order to reduce required computing time for continuing a photon history.

IV. COMPUTATIONAL TECHNIQUES

The Monte Carlo code which simulates the light scattering process is described in this chapter. Implementation of the algorithm has been effected by several programs written by C. N. Adams for several computer systems. The programming language used was FORTRAN IV with machine dependent modifications to effect implementation on Control Data Corporation systems.

The separate computations required for the Monte Carlo simulation process are presented in the order in which they occur in the execution of a typical program run. This is done because each computation is logically dependent upon those preceding it. The order of discussion should aid in the understanding of the complexity of the problem and computing requirements.

Point rejection schemes and inversion techniques are used in the model to reproduce theoretical distribution functions for the simulation of natural events in the light scattering process.

Several variance reducing techniques are used in the algorithm. Each technique has two parts. These are sampling from a biased distribution and then removing the bias in an appropriate manner. The modelling distribution is biased in such a way to increase the population of events occurring in regions of interest and to also reduce computational time in the execution of the program. Such a bias effectively increases the population of events in the

desired region, thus decreasing the variance. This bias must be removed after the desired computations have been performed in order to produce unbiased results. The bias removal is effected by assigning to each event a statistical weight determined by the true probability of its occurrence. Examples of this may be seen in the photon pathlength selections to be discussed.

a) Photon History

The Monte Carlo technique may be used to solve problems in radiative transfer by tracing histories, i.e., sequences of events that statistically occur to photons traveling through a medium or the atmosphere. The photon path is followed accurately in three dimensions after entrance into the planetary atmosphere from the sun. From the point of entrance into the atmosphere, the point of first collision of the photon is chosen along the path of travel for the photon. The direction cosines of the photon are given with respect to a fixed Cartesian coordinate system with origin at the planet center.

Either the photon makes its first collision in the atmosphere or at the planet surface. In the latter case the photon is reemitted according to Lambert's law, i.e., the intensity of the light reflected from the surface is constant in all directions with no polarization.

If the first collision of the photon is at a point in the atmosphere, the appropriate scattering event is determined by

the physical parameters of the atmosphere at the collision point and a selection of either molecular or aerosol scattering is made. Next a scattering angle for the photon is chosen from the cumulative distribution function for the appropriate type of scattering event and is dependent upon the initial polarization state of the photon before the collision occurred. A detailed discussion of this selection process will be given in a later section. The new three-dimensional path of the photon is determined using the previous direction cosines, the scattering angle with respect to the previous direction of travel, and an azimuthal angle determined in the interval from 0 to 2π . The next collision point is then determined and the entire process described for travel from one collision point to another collision point is repeated.

When the photon is traveling in an upward direction, the method of forced collisions or sampling from a biased distribution is used, so that the photon is never actually lost since a collision process must occur before passing through the outer boundary of the atmosphere by use of this method. To remove any bias that may be introduced using this technique, a statistical weight is associated with each photon. This weight, which is initially unity, is adjusted whenever a forced collision is made so that the resulting contributions to detectors are appropriately corrected. All photons are traced until their weight falls below a predetermined value which is a parameter read into the computer program. The photons may make numerous collisions within the atmosphere and also many collisions

with the planet surface before the history is terminated. This method assures that all higher order collisions which may contribute to the intensity and polarization are included in the calculation.

b) Generating Desired Distribution from a Uniform Distribution

A great deal has been written about methods of generating a uniformly distributed pseudo-random sequence of numbers, that is, one in which the probability of a number falling in a given interval is proportional to the width of the interval and does not depend upon the location of the interval. Such methods include the Von Neumann midsquare method, power residue methods, and various other means of generating a pseudo-random sequence of numbers. The uniform type of distribution is rarely found in nature and a method must be found by which the desired distribution may be modeled from this distribution.

If conditions are such that the probability of random variable T falling in the interval T to $T + dT$ is given by the integral:

$$\int_T^{T+dT} f(t) dt, \quad (12)$$

then $f(t)$ is called the probability density function for the random variable.

It must follow that

$$\int_{-\infty}^{\infty} f(t) dt = 1. \quad (13)$$

There exist several mathematical techniques for the generation of a sequence of numbers such that the fractional number contained in any interval approximates the value of the integral (13) above.

c) Point Distribution Method

A desired distribution may be generated by two uniformly distributed random numbers, R_1 and R_2 , meeting the conditions $0 \leq R_2 \leq Y_{\max}$ and $X_{\min} \leq R_1 \leq X_{\max}$, where $Y_{\max} \leq f(t)$ for all values of t and X_{\max} is sufficiently large so that the probability of t falling to the right of X_{\max} , i.e., $t > X_{\max}$, is negligible. Then if $f(R_1) \geq R_2$, R_1 is accepted as a member of the sequence, otherwise it is rejected. Then it is obvious that the number selected in any interval is proportional to the area under the curve in that interval, which is precisely the distribution desired.

In Figure 4, using the point rejection technique, point R_1 would be accepted in the sequence, but \bar{R}_1 would be rejected.

It is this method which is used to model the $3/16 (1 + \cos^2 \theta)$ phase function for the scattering angle for Rayleigh (Molecular) scattering and also for the bivariate distribution for determination of the azimuthal angle when a scattering event does occur.

Let a two-dimensional random vector (ξ, η) have joint probability function $f(x, y)$.

The partial probability density function of random variable η may be found by

$$f(\eta) = \int_{-\infty}^{\infty} f(x, \eta) dx. \quad (14)$$

The set of random numbers $\{R_i\}$ may be sampled to determine a set $\{y_i\}$ where the density is $f_{\eta}(y)$.

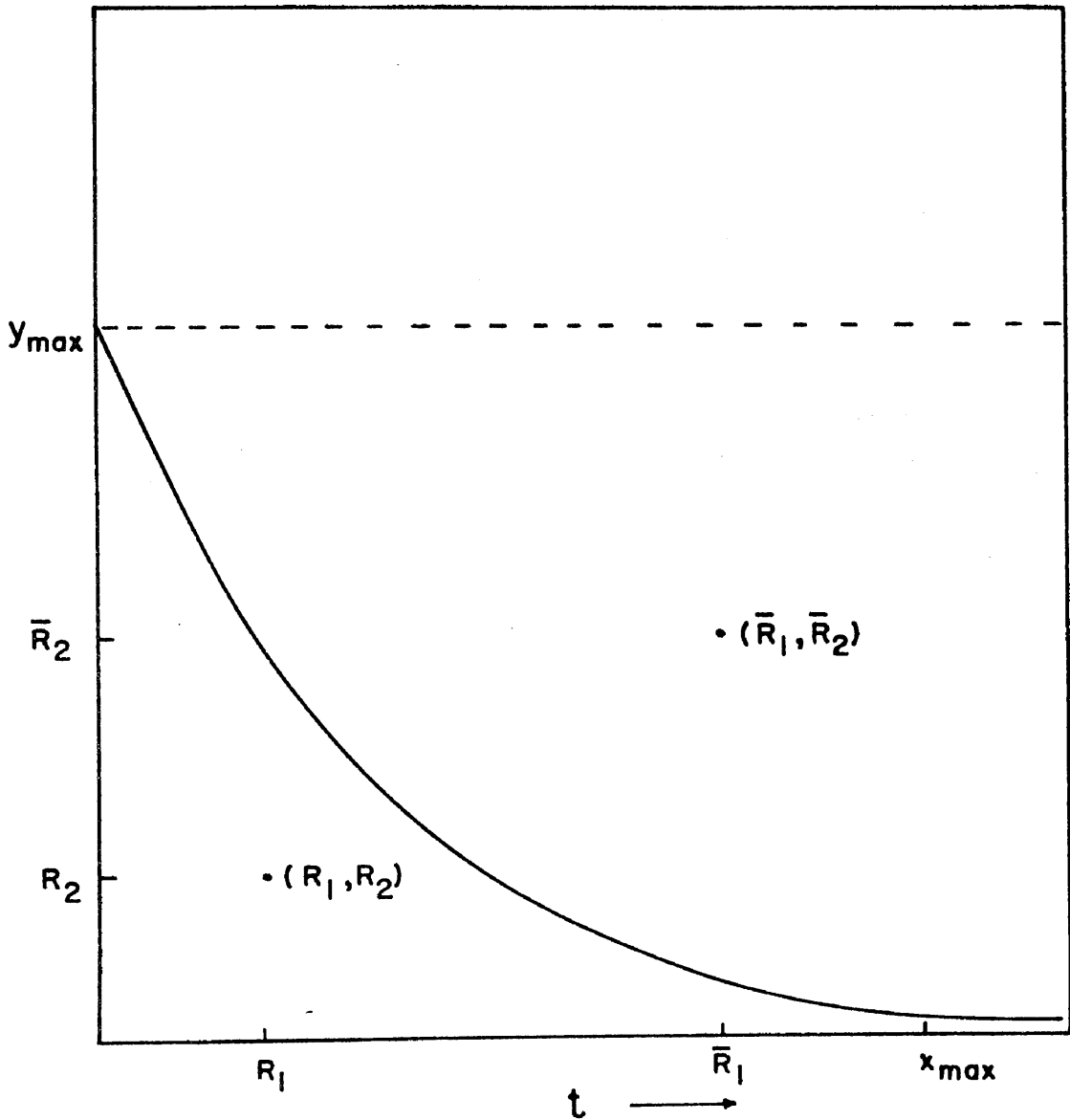


Figure 4 - Point rejection technique showing that point \bar{R}_1 would be rejected from the sequence

Consider

$$f_{\mu_j}(x | \mu_j) = f(x, \mu_j) / f_{\mu_j}(\mu_j) \quad (15)$$

Another number is sampled from the set $\{R_i\}$ to determine x_j , whose density function is $f_{\mu_j}(x | y_j)$.

It can be shown that the sequence of pair of numbers (x_j, y_j) produced in this manner has joint density function $f(x, y)$.

For matrix operations involved in scattering with polarization

$$L(\phi) = \begin{bmatrix} 1 & 0 & 0 & 0 \\ 0 & \cos(2\phi) & \sin(2\phi) & 0 \\ 0 & -\sin(2\phi) & \cos(2\phi) & 0 \\ 0 & 0 & 0 & 1 \end{bmatrix} \quad (16)$$

$$II = \begin{bmatrix} I \\ Q \\ U \\ V \end{bmatrix} \quad (17)$$

$$P(\mu) = \begin{bmatrix} P_{11} & P_{12} & 0 & 0 \\ P_{21} & P_{22} & 0 & 0 \\ 0 & 0 & P_{33} & P_{34} \\ 0 & 0 & P_{43} & P_{44} \end{bmatrix} \quad (18)$$

and

$$II'(\mu, \phi) = P(\mu) L(\phi) II. \quad (19)$$

Looking at the transformation of the intensity component only

$$I'(\mu, \phi) = I P_{11}(\mu) + \{ Q \cos(2\phi) + U \sin(2\phi) \} P_{12}(\mu) \quad (20)$$

thus

$$I'_{\mu}(\mu) = \int_0^{2\pi} I'(\mu, \phi) d\phi = 2\pi I P_{11}(\mu). \quad (21)$$

Select μ'_j from distribution $P_{11}(\mu)$. For selection of ϕ once μ_i is determined

$$I'_{\xi}(\phi | \mu'_j) = I'(\mu'_j, \phi) / I'_n(\mu'_j) \quad (22)$$

thus

$$I'_{\xi}(\phi | \mu'_j) = \frac{I P_{11}(\mu'_j) + \{Q \cos 2\phi + U \sin 2\phi\} P_{12}(\mu'_j)}{2\pi I P_{11}(\mu'_j)} \quad (23)$$

Let $I=1$, then the above reduces to

$$I'_{\xi}(\phi | \mu'_j) = \frac{1}{2\pi} \left\{ 1 + \frac{P_{12}(\mu'_j)}{P_{11}(\mu'_j)} [Q \cos 2\phi + U \sin 2\phi] \right\} \quad (24)$$

To determine the maximum value $I'_{\xi}(\phi | \mu'_j; j)$ for fixed μ'_j ,

$$\frac{\partial}{\partial \phi} (I'(\phi | \mu'_j)) = 0 = -2Q \sin 2\phi + 2U \cos 2\phi \quad (25)$$

or

$$\tan 2\phi = U/Q. \quad (26)$$

Substituting the above expression into $I'_{\xi}(\phi | \mu'_j)$ yields

$$I'_{\xi}(\phi | \mu'_j)_{\max} = \left\{ 1 + \frac{P_{12}(\mu'_j)}{P_{11}(\mu'_j)} [Q + U^2/Q] \cos 2\phi \right\}, \quad (27)$$

but

$$\cos 2\phi = (\sec 2\phi)^{-1}, \quad (28)$$

or

$$\cos 2\phi = \pm (1 + \tan^2 2\phi)^{-1/2}, \quad (29)$$

$$\cos 2\phi = \pm (1 + U^2/Q^2)^{-1/2}, \quad (30)$$

thus

$$I'_{\xi}(\phi | \mu'_j)_{\max} = \frac{1}{2\pi} \left\{ 1 + \frac{P_{12}(\mu'_j)}{P_{11}(\mu'_j)} [Q^2 + U^2]^{1/2} \right\}. \quad (31)$$

But $P_{11}(\mu'_j)$ is normalized to unity, thus

$$I'_{\xi}(\phi | \mu'_j)_{\max} = \frac{1}{2\pi} \left\{ 1 + |P_{12}(\mu'_j)| [Q^2 + U^2]^{1/2} \right\}. \quad (32)$$

This technique yields the correct form for the bivariate distribution to determine azimuthal rotation in the processing of a scattering event.

d) Generation by Inversion

By integrating $\int_0^x f(t)dt$, setting the resulting integral equal to a uniformly distributed random number in the interval from 0 to 1, the value of x then determined will have the desired distribution.

The probability that x' is in the interval $(x, x + \Delta x)$ is given by

$$P\{x \leq x' \leq x + \Delta x\} = \int_x^{x+\Delta x} f(t) dt. \quad (33)$$

Let

$$y = \int_0^x f(t) dt \quad (34)$$

and

$$y + \Delta y = \int_0^{x+\Delta x} f(t) dt, \quad (35)$$

then for some random number RN , such that $0 < RN < 1$, the probability of finding RN in the interval $(y, y + \Delta y)$ is given by

$$P\{y \leq RN \leq y + \Delta y\} = \Delta y \quad (36)$$

but,

$$\Delta y = \int_x^{x+\Delta x} f(t) dt, \quad (37)$$

thus,

$$P\{y \leq RN \leq y + \Delta y\} = P\{x \leq x' \leq x + \Delta x\}. \quad (38)$$

This method is faster and a great deal more efficient than the point rejection technique, provided of course the probability density function $f(t)$ can be integrated and x solved in terms of an inverse function $F^{-1}(RN)$ such that

$$x = F^{-1}(RN). \quad (39)$$

It is this technique which is used in the selection of optical

path lengths traversed by photons in the atmosphere.

e) Photon Selection

The first step in the simulation of the scattering sequence is the selection of a photon whose simulated history is to be followed. Both its direction and coordinates must be chosen.

Each photon is incident in the positive z direction in the planet system. Hence if we let \hat{s} be a unit vector in the photon direction and

$$\hat{s} = a\hat{x} + b\hat{y} + c\hat{z}, \quad (40)$$

where a, b, and c are the direction cosines of \hat{s} in the fixed planet system. For the initial incident photon, a and b are zero while c is unity.

Assuming uniform incident flux and azimuthal symmetry, a photon has uniform probability of incidence on any element of a plane area perpendicular to \hat{s} . As the photon is actually incident on the atmosphere, it must be incident on the rim of a disk of radius r, perpendicular to \hat{s} . This radius must be determined as shown in Figure 5.

For increased flexibility in atmospheric studies, such as needed for solution of twilight problems by Monte Carlo techniques, it is desired to be able to bias the r distribution so that r may be selected in the range

$$R' \leq r \leq R_A, \quad (41)$$

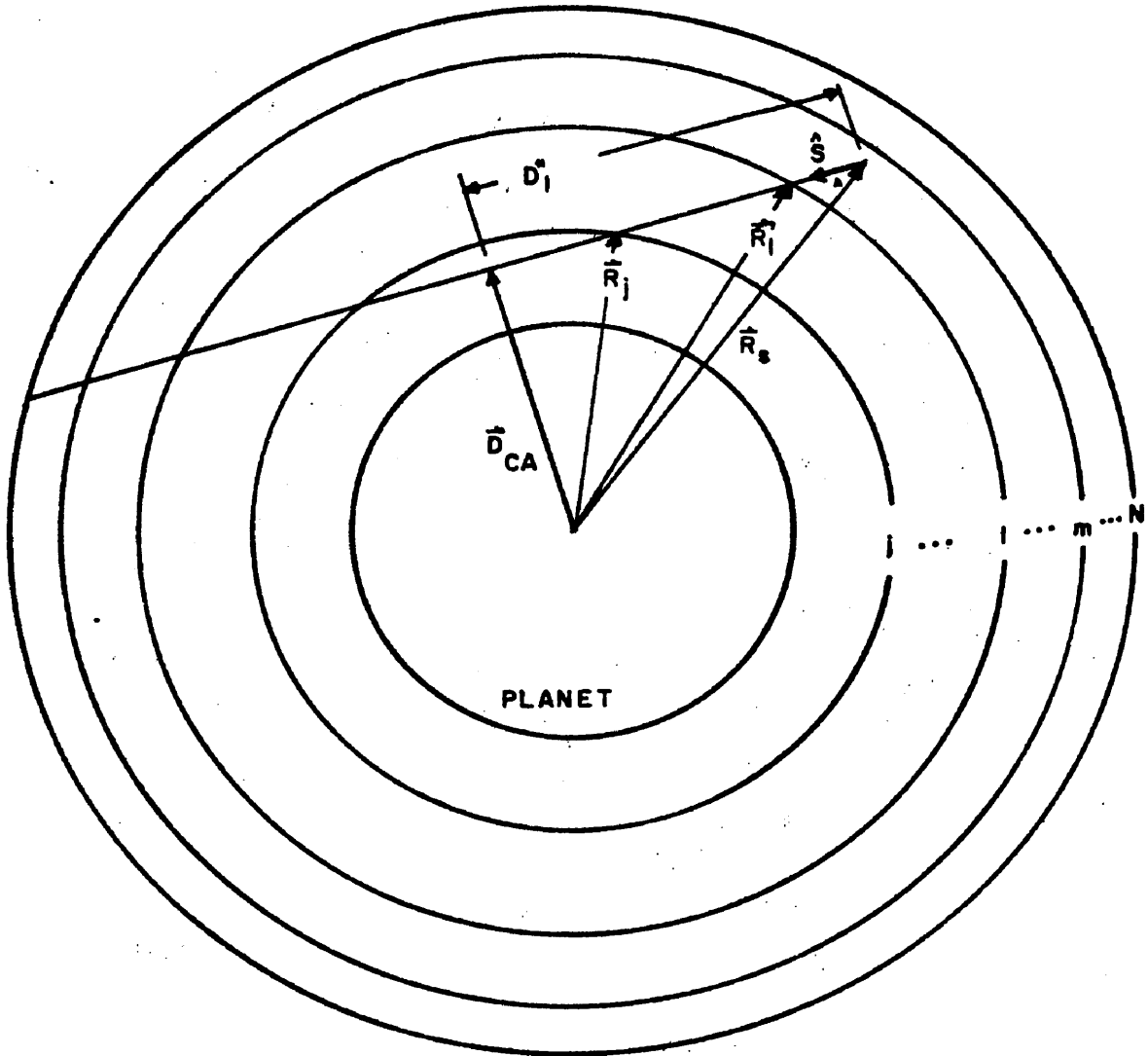


Figure 5 - Selection and determination of incident point on the atmosphere

where R' is in the range

$$0 \leq R' \leq R_A, \quad (42)$$

and R_A is the radius of the atmosphere. Requiring that

$$N \int_{R'}^{R_A} 2r dr = 1 \quad (43)$$

results in

$$N = (R_A^2 - R'^2)^{-1}. \quad (44)$$

Thus by the method of inversion for the selection of by a random number RN results in

$$RN = (r^2 - R'^2)(R_A^2 - R'^2)^{-1} \quad (45)$$

Solving this expression for r , the distribution modelling formula is found to be

$$r = (R' + RN(R_A^2 - R'^2))^{1/2}. \quad (46)$$

For R' not zero, sampling r in this manner introduces bias into the calculation. The bias may be removed by a statistical weight factor, w , given by

$$w = P\{0 \leq r \leq R_A\} / P\{R' \leq r \leq R_A\} \quad (47)$$

thus

$$w = 1 - R'^2 / R_A^2. \quad (48)$$

For R' equal to zero the weight is unity. Not only does this allow a shifting of r as desired, but it also has the effect of reducing the variance in certain regions of interest. This procedure was introduced by Hammersley and Handscomb (1964).

To complete the specification of the point of incidence of a photon history, an azimuthal angle must be chosen. If ϕ is the angle between r and the planet y -axis, then ϕ must be uniformly

distributed in the interval from 0 to 2π . Gamma is specified by

$$\gamma = 2\pi RN \quad (49)$$

where RN is a random number in the interval from 0 to 1. The coordinates of the point of incidence, (x,y,z) , are given by

$$x = r \sin \gamma \quad (50)$$

$$y = r \cos \gamma \quad (51)$$

$$z = (R_A^2 - r^2)^{1/2}. \quad (52)$$

f) Pathlength Selection

To decrease the computational time, it is necessary to require that no photon escape the atmosphere. If this is not done, a significant number of incident photons escape before experiencing a collision. The requirement is satisfied in the determination of ρ , the optical pathlength traversed by a photon before collision. Two exponential distributions in optical pathlength are used, one of which is biased to ensure that the photons remain within the atmosphere.

If a line along the direction vector \hat{s} of the photon intersects the planet surface, the unbiased distribution is used. In this case the photon cannot escape without scattering either in the atmosphere or from the ground. Solving the equation

$$RN = \int_0^{\rho} e^{-x} dx, \quad (53)$$

where RN is a random number, gives a means of sampling from the exponential distribution. The solution for ρ is

$$\rho = -\ln(1-RN) \quad (54)$$

If RN is distributed uniformly in the interval (0,1), then (1-RN) is also uniformly distributed in the interval (0,1). Thus

$$\rho = -\ln(RN) \quad (55)$$

also gives an unbiased sampling from the exponential distribution as desired.

A means of sampling from the truncated distribution is needed when the photon does not see the planet surface along its path and has a finite probability of escaping without a collision process in the atmosphere. This is accomplished by solving the equation

$$RN = (1 - e^{-\tau_{max}})^{-1} \int_0^{\rho} e^{-x} dx \quad (56)$$

where τ_{max} is the total optical pathlength through the atmosphere along \hat{s} . The solution for ρ is

$$\rho = -\ln(1 - RN(1 - e^{-\tau_{max}})). \quad (57)$$

If RN is a random number in the interval (0,1), then

$$0 < \rho < \tau_{max}. \quad (58)$$

In the limit as τ_{max} increases without bound, the unbiased distribution is produced.

Sampling from the truncated distribution introduces a removable bias. The bias is removed by initializing the statistical weight to unity for the incident photons. Every time the optical pathlength ρ is sampled from the truncated exponential distribution,

the photon's statistical weight is reduced by the factor $(1 - e^{-\tau_{\max}})$. This is the probability that a collision will occur before the photon escapes the atmosphere.

The above method is described by Cashwell and Everett (1959) and used by Kattawar and Plass (1968) and Collins and Wells (1971).

g) Tau Calculations

The optical pathlength τ , traversed in passing through the atmospheric zones, is used in the selection of ϵ , determination of the statistical weight, computation of scattering point coordinates, and calculations of emergent fluxes and intensities.

The tau calculations fall into two main categories. These categories involve the strictly outgoing photon and the incoming photon.

Let \vec{R}_S be the radius vector from the planet center to the point where a photon begins movement in the \hat{s} direction, and let \hat{R}_S be a unit vector along \vec{R}_S . A photon is strictly outgoing if

$$\cos \Delta \geq 0 \quad (59)$$

where

$$\cos \Delta \triangleq \hat{R}_S \cdot \hat{s} . \quad (60)$$

Otherwise, the photon is said to be incoming.

h) Outgoing Photon

For the treatment of an outgoing photon, consider a plane passing through the radius vector \vec{R}_S and containing the photon

direction vector \hat{s} . This geometric configuration and cross-section is illustrated in Figure 6.

The photon is located in the j -th zone and is traveling in direction \hat{s} . To calculate the total optical tau to the outer atmospheric boundary, the physical distance through each zone must be calculated and used to determine the optical thickness of the zone along the photon path. This is accomplished easily by use of the Pythagorean theorem and vector properties. Let

$$\Delta' = \pi/2 - \Delta, \quad (61)$$

$$|\vec{D}_{CA}| = |\vec{R}_S| \cos \Delta' \quad (62)$$

and

$$D_1 = (\vec{R}_S \cdot \vec{R}_S - \vec{D}_{CA} \cdot \vec{D}_{CA})^{1/2}. \quad (63)$$

The distance from the point \vec{R}_S to the boundary of the j -th zone along the photon path is given by

$$D = (\vec{R}_S \cdot \vec{R}_S - \vec{D}_{CA} \cdot \vec{D}_{CA})^{1/2} - D_1. \quad (64)$$

For \vec{R}_S in the j -th zone, the total optical pathlength along \hat{s} , τ_{\max} , is given by

$$\tau_{\max} = \sum_{i=j}^N (D_i - D_{i-1}) \beta_i + (D_j - D_1) \beta_j. \quad (65)$$

This maximum optical thickness along the photon path is used for sampling from the truncated exponential distribution and adjustment of the appropriate photon statistical weight as previously discussed.

After sampling from the biased distribution, similar calculations are performed to determine the physical distance traversed by the photon in traveling an optical distance ρ .

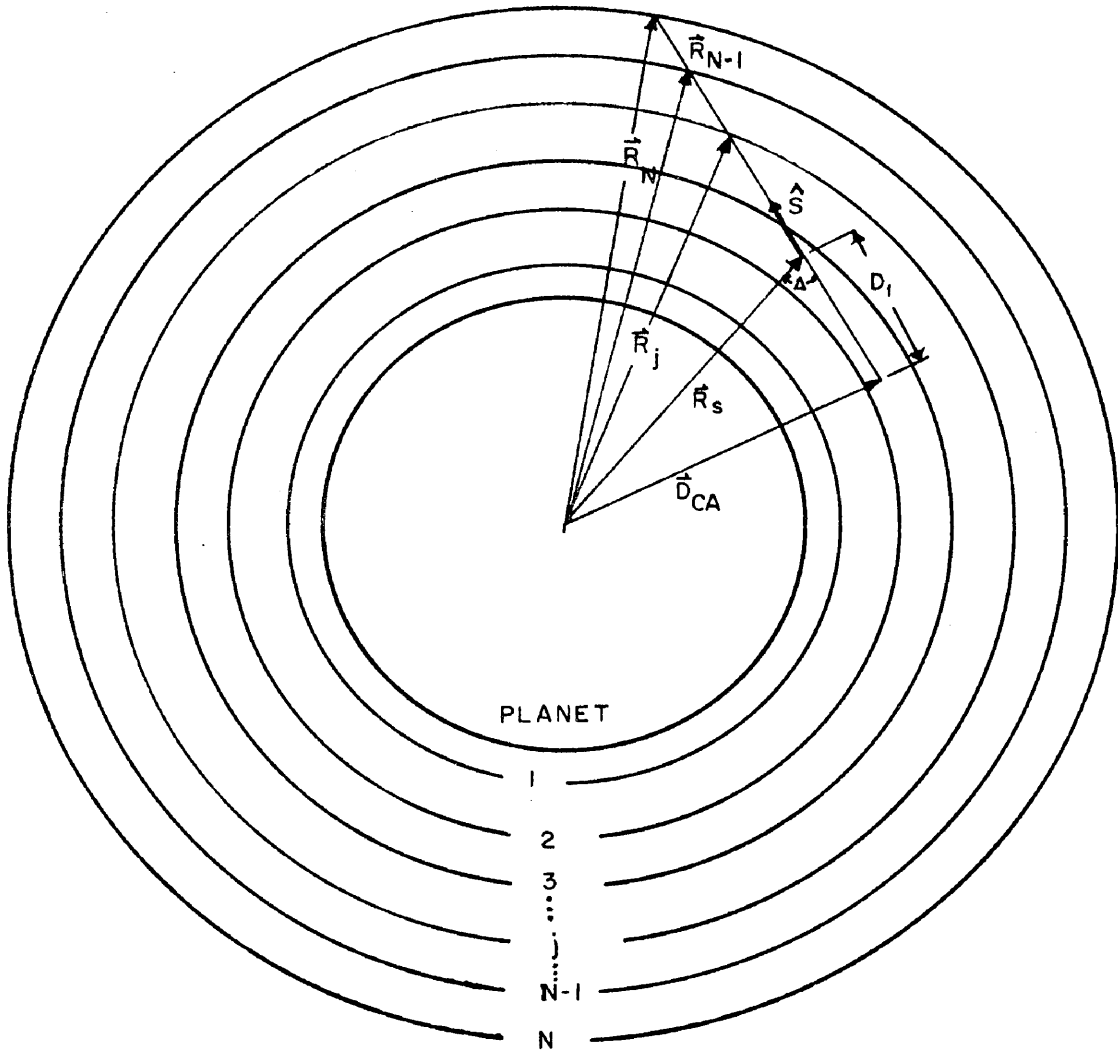


Figure 6 - Geometry for an outgoing photon

i) Incoming Photon

In the case of an incoming photon, where

$$\cos \Delta < 0, \quad (66)$$

a complication arises since the extended path of the photon may or may not intersect the planet surface. In Figure 7 the geometry of the problem is shown in a plane containing the vectors \vec{R}_S and \hat{s} .

Let \vec{D}_{CA} be the vector to the point for the distance of closest approach of the photon path and assume this point is in the j-th zone. Thus

$$|\vec{D}_{CA}| = |\vec{R}_S| \sin \Delta \quad (67)$$

$$D_1' = |\vec{R}_S| \cos \Delta \quad (68)$$

where

$$\Delta = \cos^{-1} (-\vec{R}_S \cdot \hat{s}). \quad (69)$$

Note also that

$$D_1' = (\vec{R}_S \cdot \vec{R}_S - \vec{D}_{CA} \cdot \vec{D}_{CA})^{1/2} \quad (70)$$

The distance from the point \vec{R}_S to the boundary of the k-th zone along the photon path is given by

$$D_k' = (\vec{R}_S \cdot \vec{R}_S - \vec{D}_{CA} \cdot \vec{D}_{CA})^{1/2} \quad (71)$$

For \vec{R}_S in the m-th zone, the total optical pathlength along \hat{s} to \vec{D}_{CA} is given by

$$\tau' = D_{m+1} \beta_m + \sum_{i=j+1}^{m-1} (D_i - D_{i+1}) \beta_i + (D_1' - D_j) \beta_j. \quad (72)$$

The remaining optical thickness, τ'' , from the point \vec{D}_{CA} to the boundary of the atmosphere is calculated in the same manner as

as an outgoing photon to yield

$$\tau_{\max} = \tau' + \tau'' \quad (73)$$

This allows a sampling of ϱ from the truncated exponential distribution for forced scattering before exit from the atmosphere using appropriate statistical weight adjustment.

For the case where the photon path is intersected by the planet surface,

$$|\bar{D}_{CA}| < R_p \quad (74)$$

and the optical thickness to the planet surface, τ' , is given by

$$\tau' = D'_m \beta_m + \sum_{i=2}^{m-1} (D_i - D_{i-1}) \beta_i + (D'_1 - D_1) \beta_1 \quad (75)$$

In this case, the sampling of ϱ is from an unbiased exponential distribution to allow for the probability of a photon striking the planet surface.

j) Determination of the Scattering Point

Once the optical pathlength to collision, ϱ , has been determined, the coordinates of the scattering point may be calculated. Beginning at the point \vec{R}_S , the optical thickness τ is computed along \hat{s} to each zone boundary. At each zone the cumulative τ is compared to ϱ and the distance, D , is also accumulated. If $\tau < \varrho$, the calculation continues until a τ value is reached such that $\tau \geq \varrho$. Thus, if $\tau \geq \varrho$ in the j -th zone, the total physical distance along \hat{s} to the scattering point is

$$D_\tau = D - (\tau - \varrho) / \beta_j. \quad (76)$$

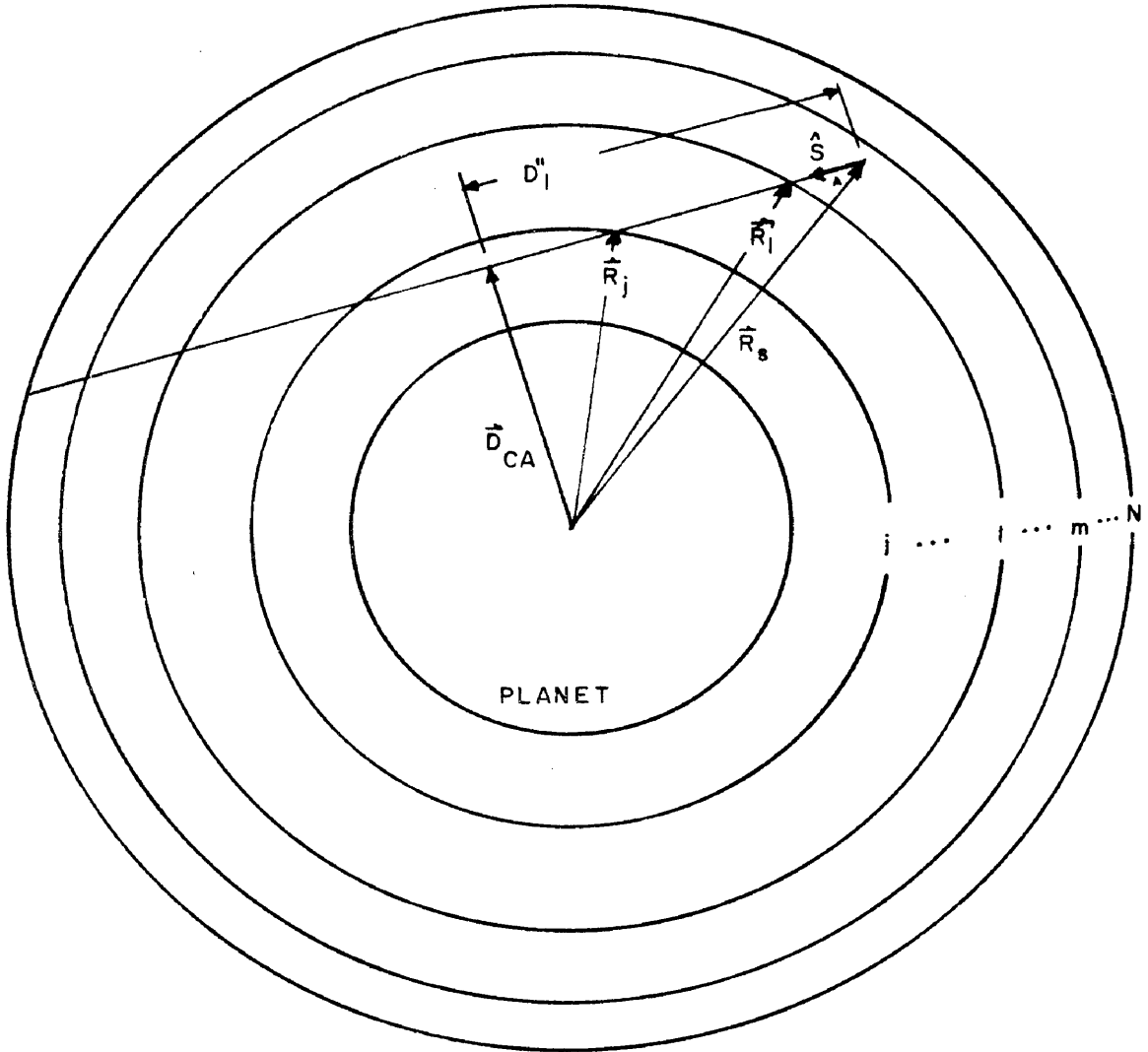


Figure 7 - Geometry for an incoming photon

The next scattering point may be given by

$$\vec{R} = \vec{R}_s + D \hat{s}, \quad (77)$$

where \vec{R}_s is the current position vector for the photon and \hat{s} is the unit direction vector for the photon.

Should the photon encounter the planet surface before traveling optical distance ϱ , then the calculations are terminated with $D_{\mathcal{N}}$ equal to the distance from \vec{R}_s to the surface along \hat{s} . The point at which the photon strikes the planet surface is given by (73).

V. MIE SCATTERING

Since the Monte Carlo calculations could only be done for a limited number of cases, each having one or more layers of particles with a definite size distribution and index of refraction, it was necessary to first study contour plots of the single scattered polarization as a function of the size parameter ($x=2\pi r/\lambda$) where r denotes the particle radius and λ is the wavelength. Because of the rapid fluctuations in the results of the Mie theory as x is varied, it is necessary to integrate the results over a range of values of x . The contour plots of Coffeen (1969 and private communication) were used and also generated plots from the Mie code of Kattawar and Plass (1967a, 1967b) with smaller integration intervals than were used by Coffeen. Agreement is shown with Coffeen in that it is impossible to represent the variation of the polarization with phase angle and wavelength with a real index of refraction equal to 1.33. In order to match the measured polarization curves, it is necessary to choose a particle size distribution with a modal radius of about 1μ and real indices of refraction in the approximate range 1.45 to 1.60.

VI. CLOUD MODELS

a) Single Layer: Model-1 (M-1)

The first particle size distribution chosen is one of those proposed by Deirmendjian (1964) for water droplet clouds on earth, namely

$$n(r) \propto r^6 e^{-6r} \quad (78)$$

This distribution has a modal radius $r_m = 1\mu$ and a mean radius $\langle r \rangle = 1.17\mu$. The range of integration over the distribution was from $r=0.03$ to $r=10.5\mu$ and a refractive index of $N_1=1.5$ and $N_2=0.0$ (real and imaginary parts respectively) was used.

Figure 8 shows the single scattering phase function and Figure 9 the single scattering polarization for $\lambda = 0.55\mu$. The degree of polarization used here is the conventional Rubenson definition; namely

$$P = (I_r - I_\parallel) / (I_r + I_\parallel) \quad (79)$$

where the subscripts r and \parallel refer to directions perpendicular and parallel to the scattering plane respectively.

The observations of Lyot (1929) and Coffeen and Gehrels (1969) show four neutral points occurring at phase angles of 8° , 23° , 146° , and 173° and two maxima located at phase angles of 15° ($P=1.5\%$) and 160° ($P=1.8\%$). The single scattered polarization shown in Figure 9 is zero near these neutral points and has maxima at the

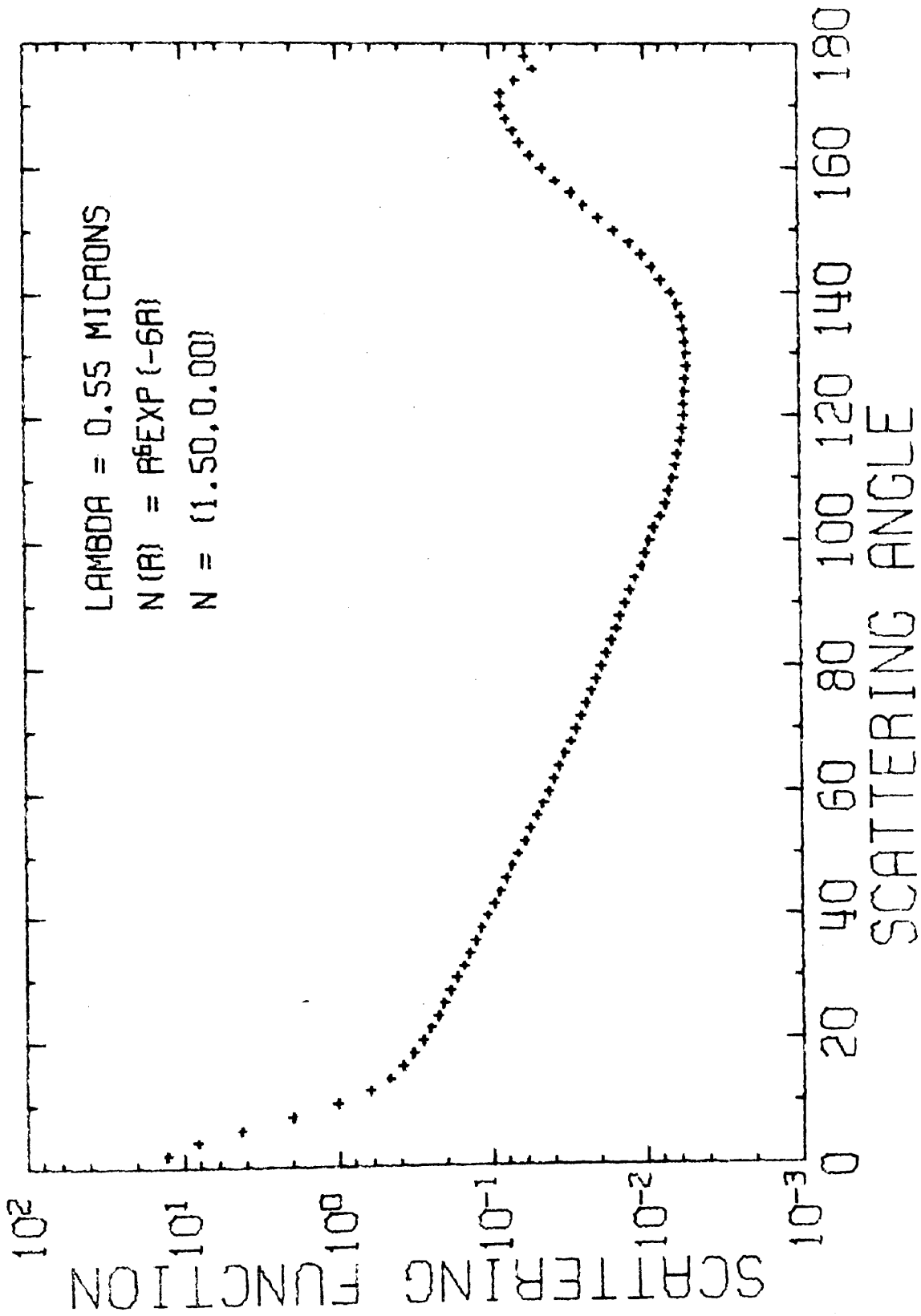


Figure 8 - Single-scattering phase function for model M-1 at 0.55 μ with particle size distribution $n(r) \propto r^6 e^{-6r}$ and refractive index $N=(1.50, 0.00)$

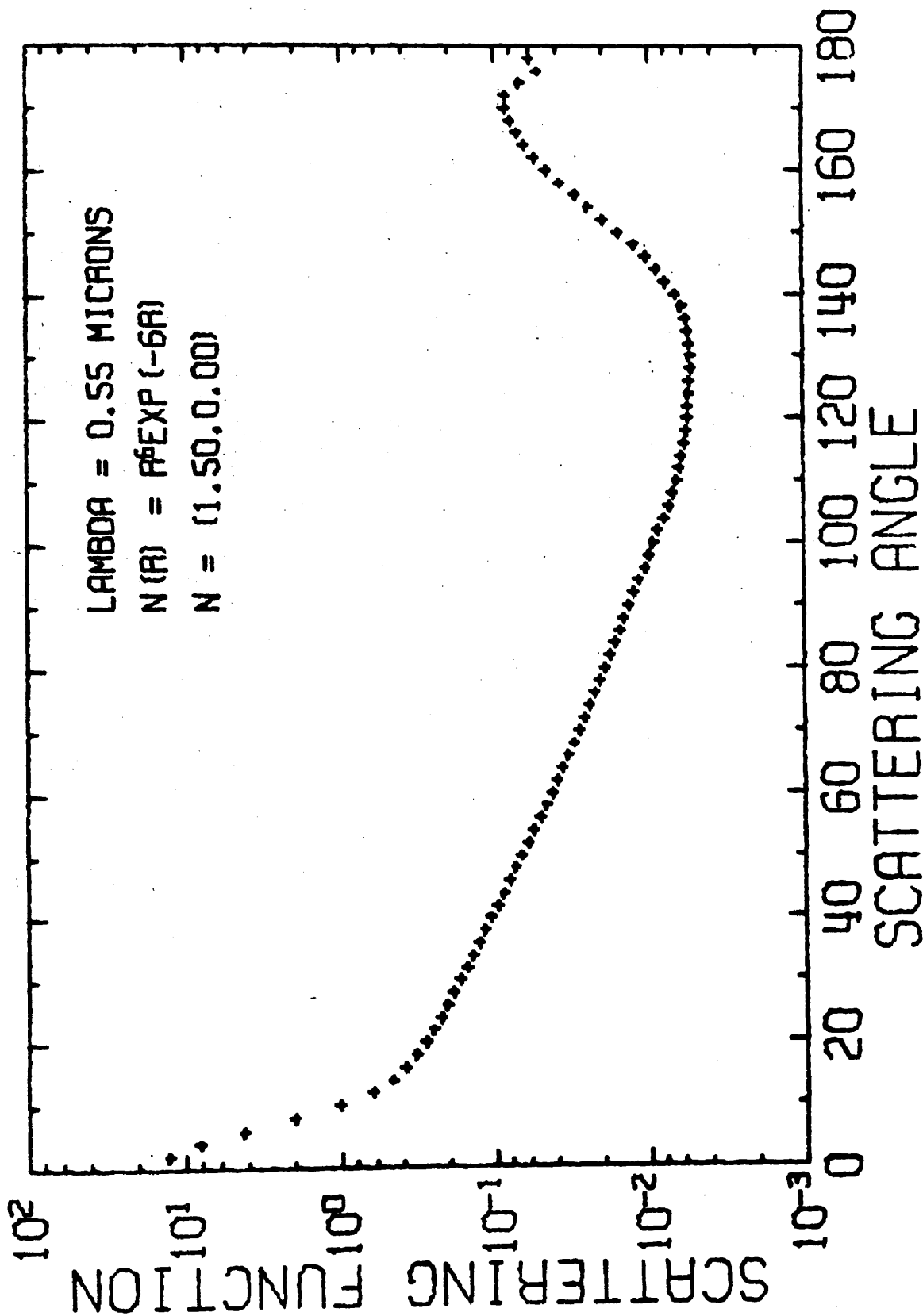


Figure 9 - Degree of polarization for model M-1 at 0.55 μ

correct angles. In order to complete the description of the cloud model, the total optical thickness, single scattering albedo, and extinction coefficient versus height have to be specified. The optical thickness has to be substantial due to the fact that the single scattering polarization curve is much higher than the observations; the value $\tau = 50.0$ is used. The extinction coefficient is assumed to have the following form

$$\beta_{\text{EXT}} \propto e^{-z/h}, \quad (80)$$

where z measures the height above the ground in km. The scale height for the concentration variation of the atmosphere was calculated from Johnson (1968); a value of 10 km is used. The radius of the planet Venus is taken as 6050 km. The optical depth versus height is computed from

$$\tau = 50 e^{(-0.1 z)}. \quad (81)$$

Although this is only an approximate representation of the atmosphere, a more accurate description is not necessary for these calculations. The single scattering albedo is obtained by matching the calculated spherical (Bond) albedos to those presented by Irvine (1968). For this model at $\lambda = 0.55 \mu$, $\omega_0 = 0.9994$ gives a spherical albedo $A = 0.876$ (see Table I) which is consistent with Irvine's data.

The polarization versus phase angle curve obtained from the Monte Carlo calculation for this model is presented in Figure 10 along with the observational data of Lyot (1929) and Coffeen and

TABLE I. Single Scattering Albedo ω_0 and
Computed Bond Albedo for Various Models

λ	ω_0	A_B	MODEL
0.34	0.9770	0.520	M-1
0.55	0.9994	0.876	M-1
0.99	0.9996	0.904	M-1
0.34	0.9770	0.550	M-2
0.55	0.9994	0.874	M-2
0.99	0.9999	0.925	M-2
0.34	0.9770	0.542	M-3
0.55	0.9994	0.873	M-3
0.99	0.9994	0.887	M-3
0.34	0.9770	0.543	M-4
0.55	0.9994	0.874	M-4
0.99	0.9996	0.921	M-4
0.34	0.9770	0.543	M-5
0.55	0.9994	0.876	M-5
0.99	0.9996	0.897	M-5

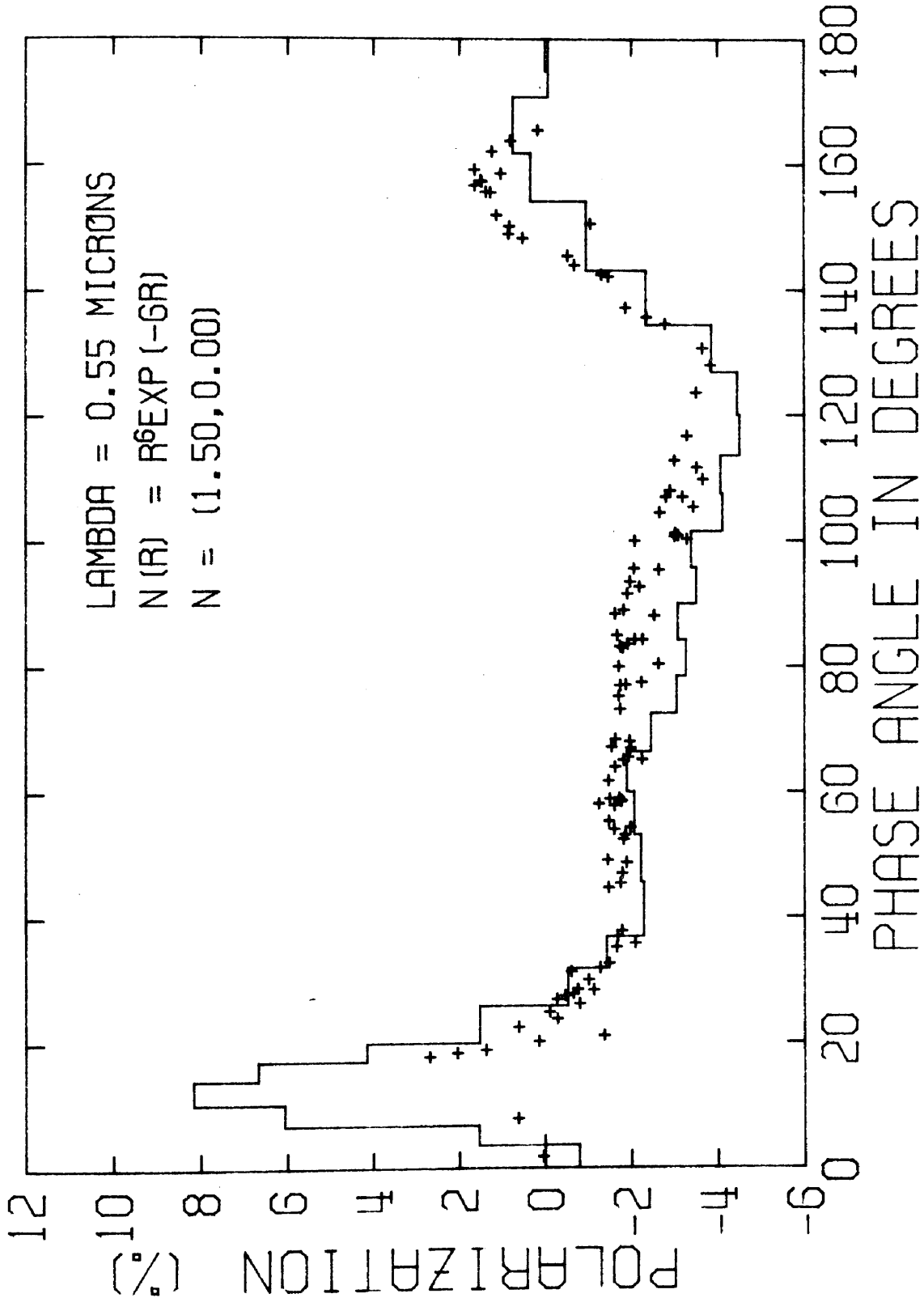


Figure 10 - Comparison of the degree of polarization versus phase angle for model M-1 with experimental observations for $\lambda=0.55 \mu$

Gehrels (1969). The agreement is quite good for phase angles between 20° and 150° ; however, the maximum is too high at 15° and too low at 160° for $\lambda=0.55\mu$. It should be noted that this condition can be remedied by using a smaller modal radius, e.g. model M-4; however, such a choice creates problems at the other wavelengths. Attempts were made to select the modal radius which gives the best overall fit at all three wavelengths. A possible explanation of this discrepancy is given in Chapter VII. The polarization is slightly too low near 90° . These values would be raised by at most 5% near 90° by the addition of an admixture of 1.2% Rayleigh scattering which should be present at this wavelength to correspond to the 6% Rayleigh scattering at 0.34μ , but this change would be barely visible on the scale of the figure.

The visual magnitude is presented in Figure 11 along with the least squares curve obtained from Knuckles, et.al. (1961). For phase angles in the vicinity of 10° the discrepancy is largest; however, there is considerable scatter in the experimental data in this region also. The Monte Carlo results near 180° have a larger probable error, because of the low intensities.

The same size distribution and refractive index are used at 0.34μ . Various amounts of the Rayleigh phase matrix were added to the aerosol phase matrix in order to explain the observed positive polarization between 40° and 100° . The single scattering phase function and polarization are given in Figures 12 and 13 for a 6% admixture of Rayleigh scattering which was found to be optimum

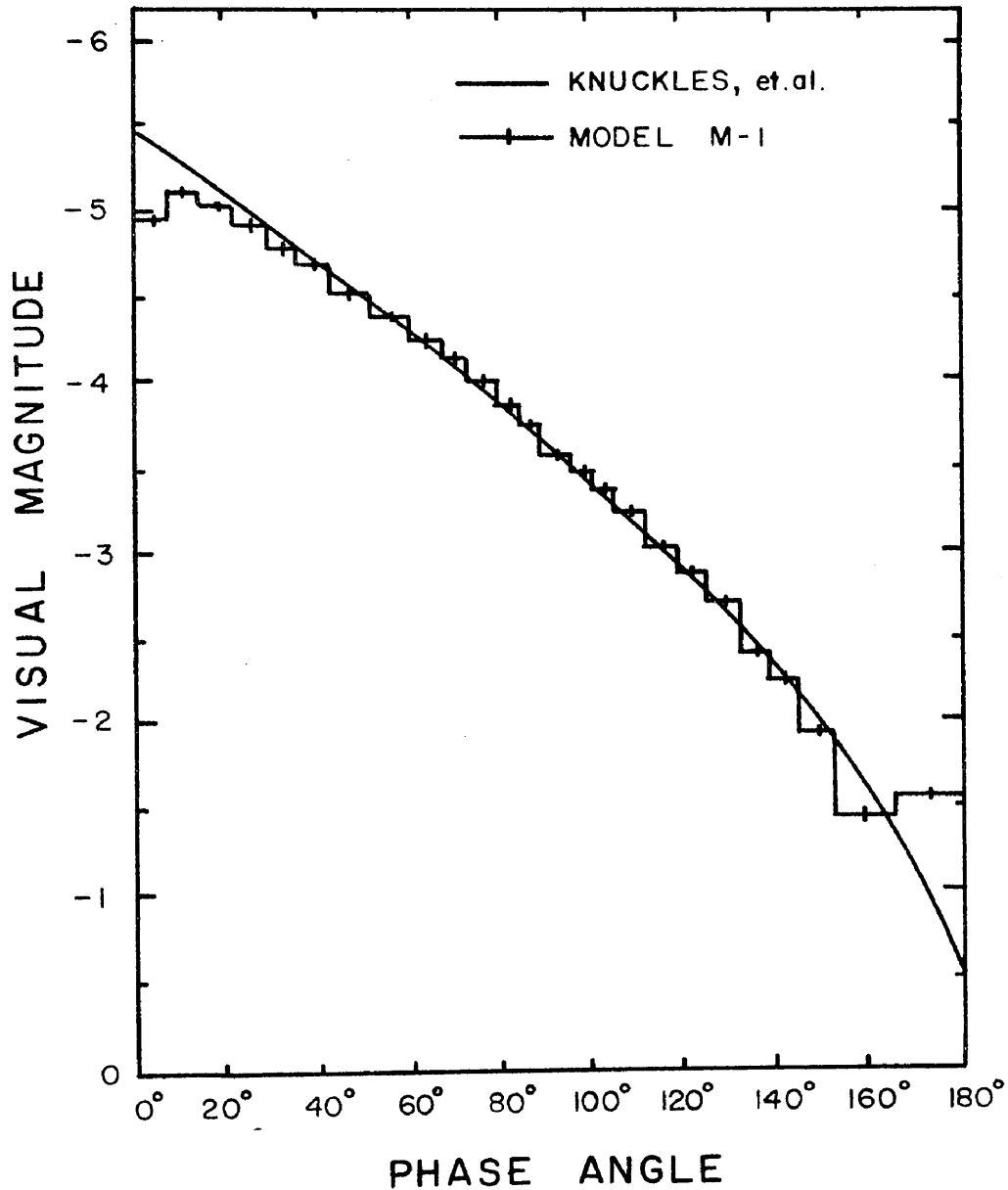


Figure 11 - Comparison of the least-squares visual magnitude as measured by Knuckles et. al. (1961) and the Monte Carlo solutions (histogram) for model M-1 at 0.55μ

for this model. The Monte Carlo results for the polarization of the multiple scattered photons from Venus is given in Figure 14. It should be noted that the maximum at about 15° phase angle is virtually unaffected by the addition of Rayleigh scattering and is due to the aerosol scattering. All of the albedo data is given in Table I.

The results for the single scattering phase function and polarization for the same aerosol model at 0.99μ are presented in Figures 15 and 16. The Monte Carlo results for the multiple scattered photons are presented in Figure 17. A good fit is obtained for phase angles ranging from 20° to 140° ; however, the minimum at 10° is too low.

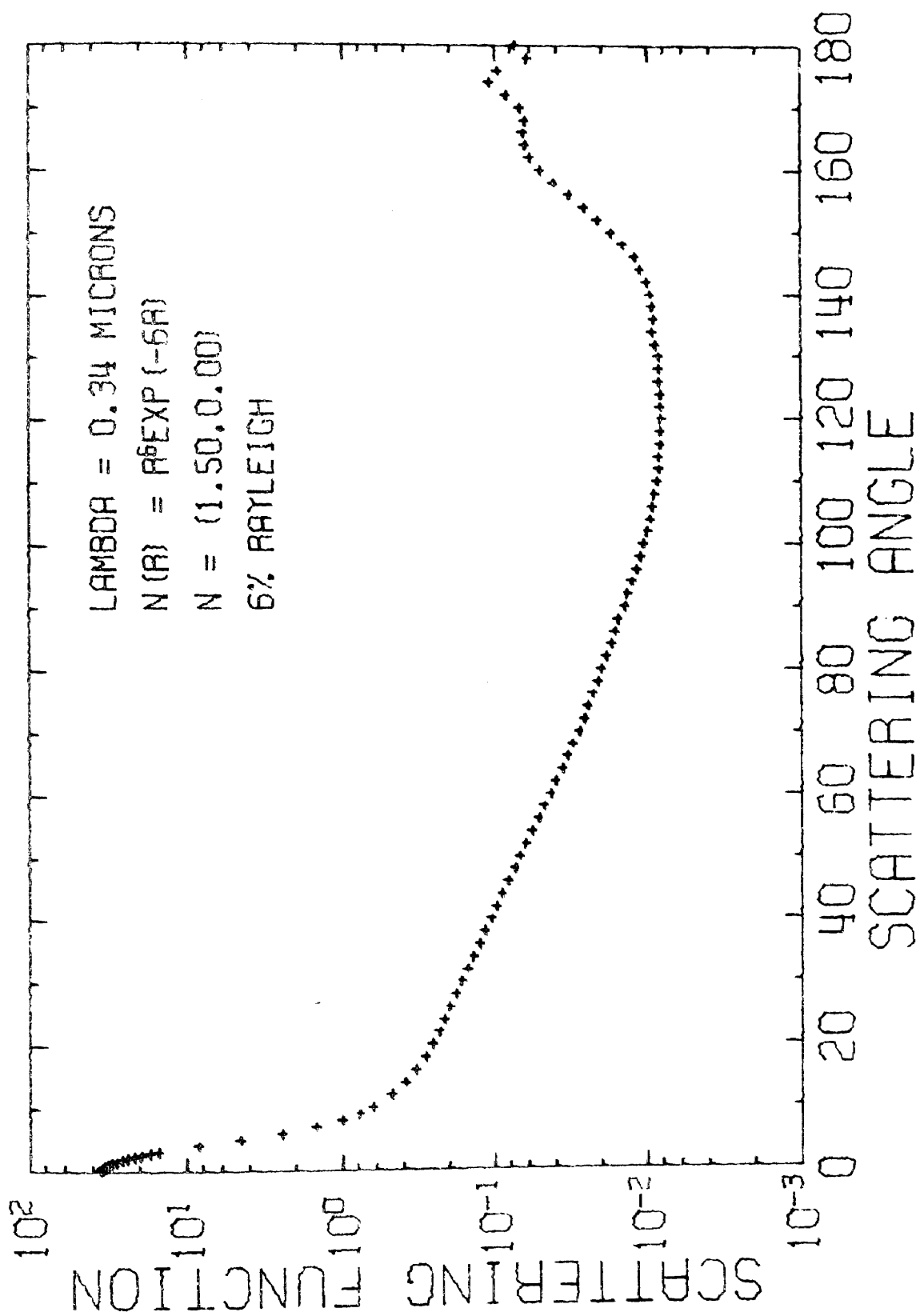
b) Single Layer: Model-2 (M-2)

For this model the same refractive index is used as in M-1, namely $N_1=1.5$ and $N_2=0$ and the same modal radius $r_m=1.0$. The functional form of the distribution

$$n(r) \propto r^6 e^{-3r^2} \quad (82)$$

gives more weight to particles whose radii are less than 2μ . The mean radius $\langle r \rangle = 1.04$. The Monte Carlo results are presented in Figure 18 for 0.34μ for a 6% admixture of Rayleigh scattering. Again the maximum due to the aerosols at a phase angle of 15° is too high.

At a wavelength of 0.55μ the polarization is shown in Figure 19; the maximum at 15° is fitted much better than in the case of M-1,

Figure 12 - Same as Figure 8 but for 0.34 μ

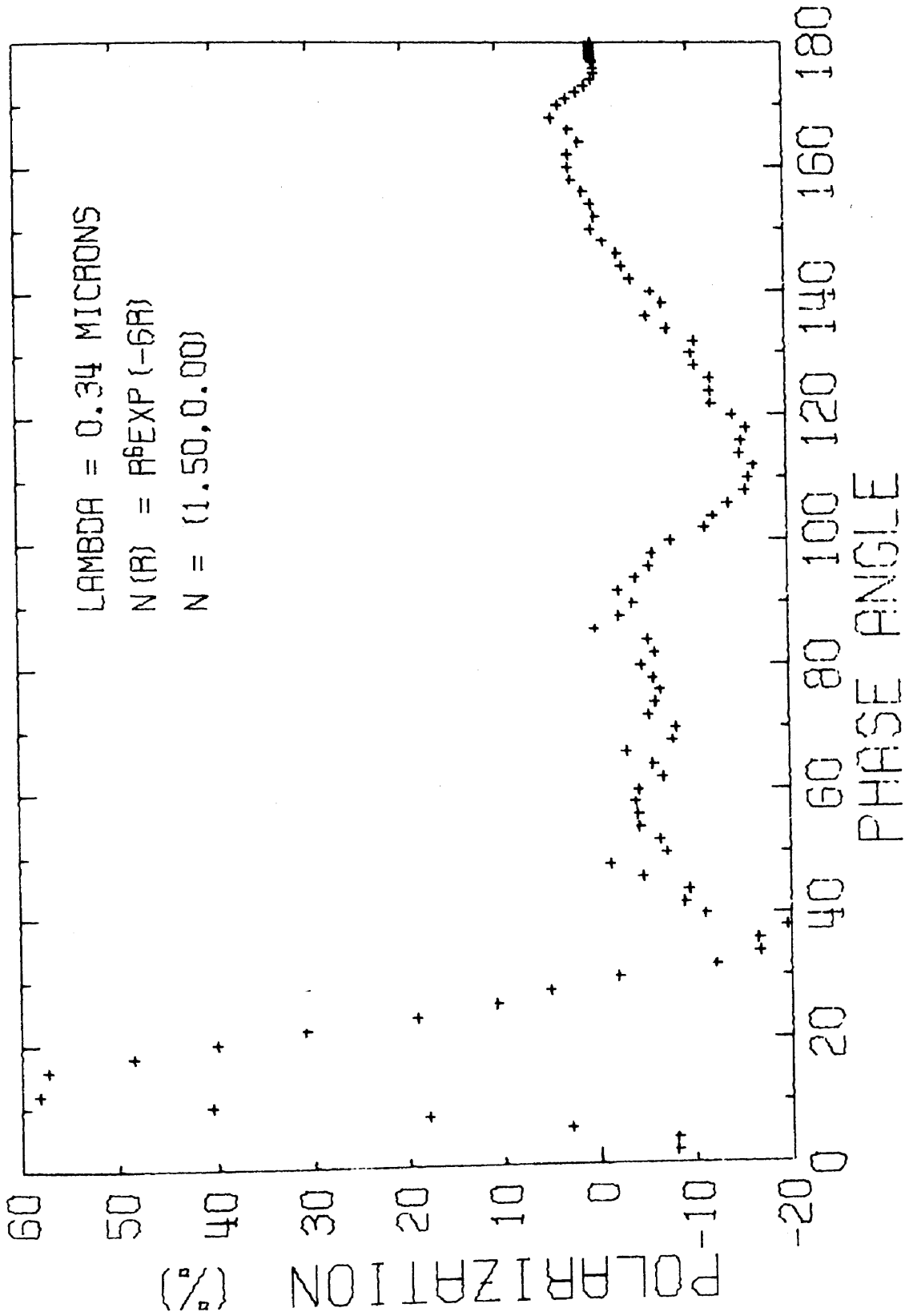


Figure 13 - Same as Figure 9 but for 0.34 μ

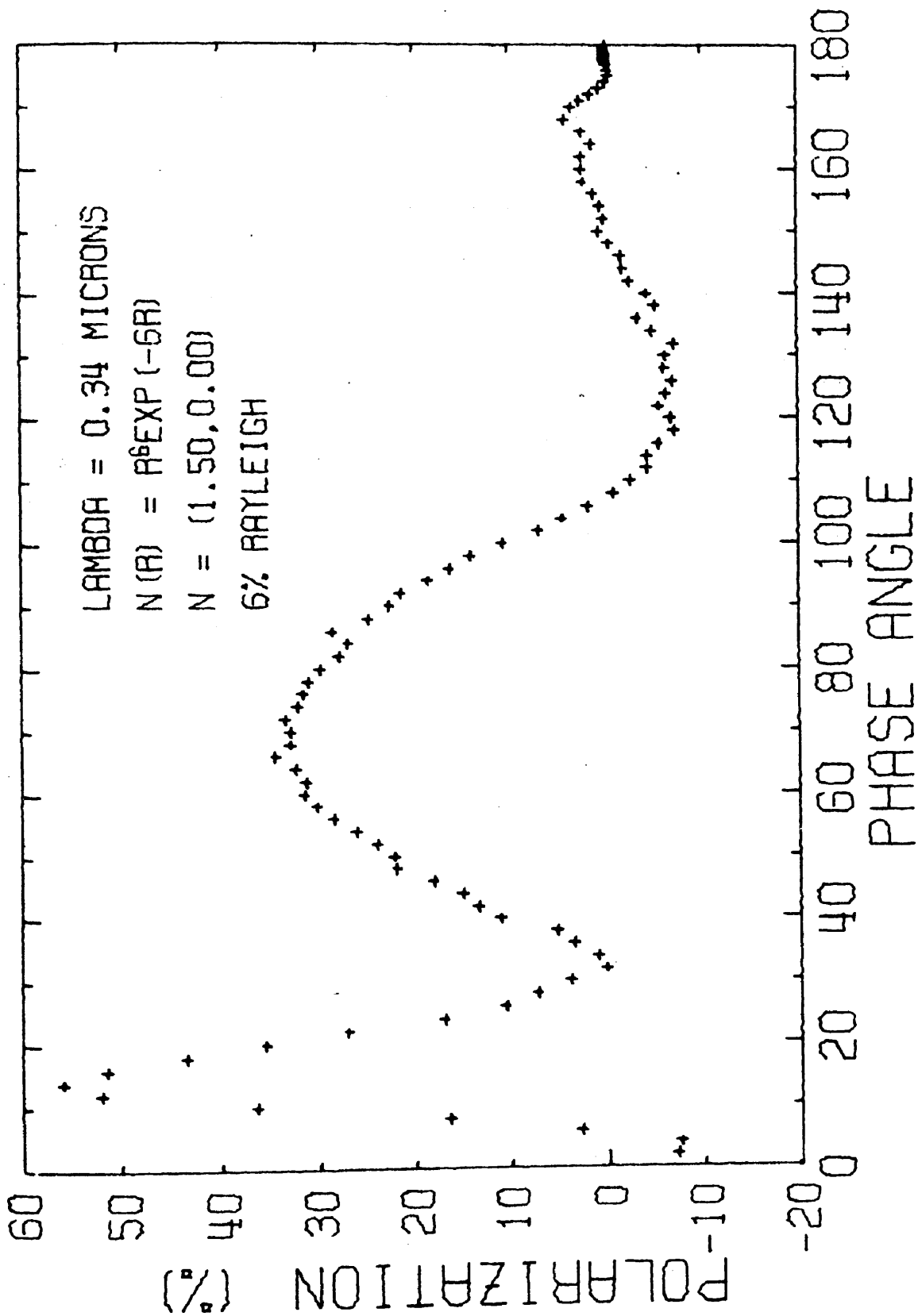


Figure 14 - Same as Figure 10 with a 6% admixture of Rayleigh scattering at 0.34 μ

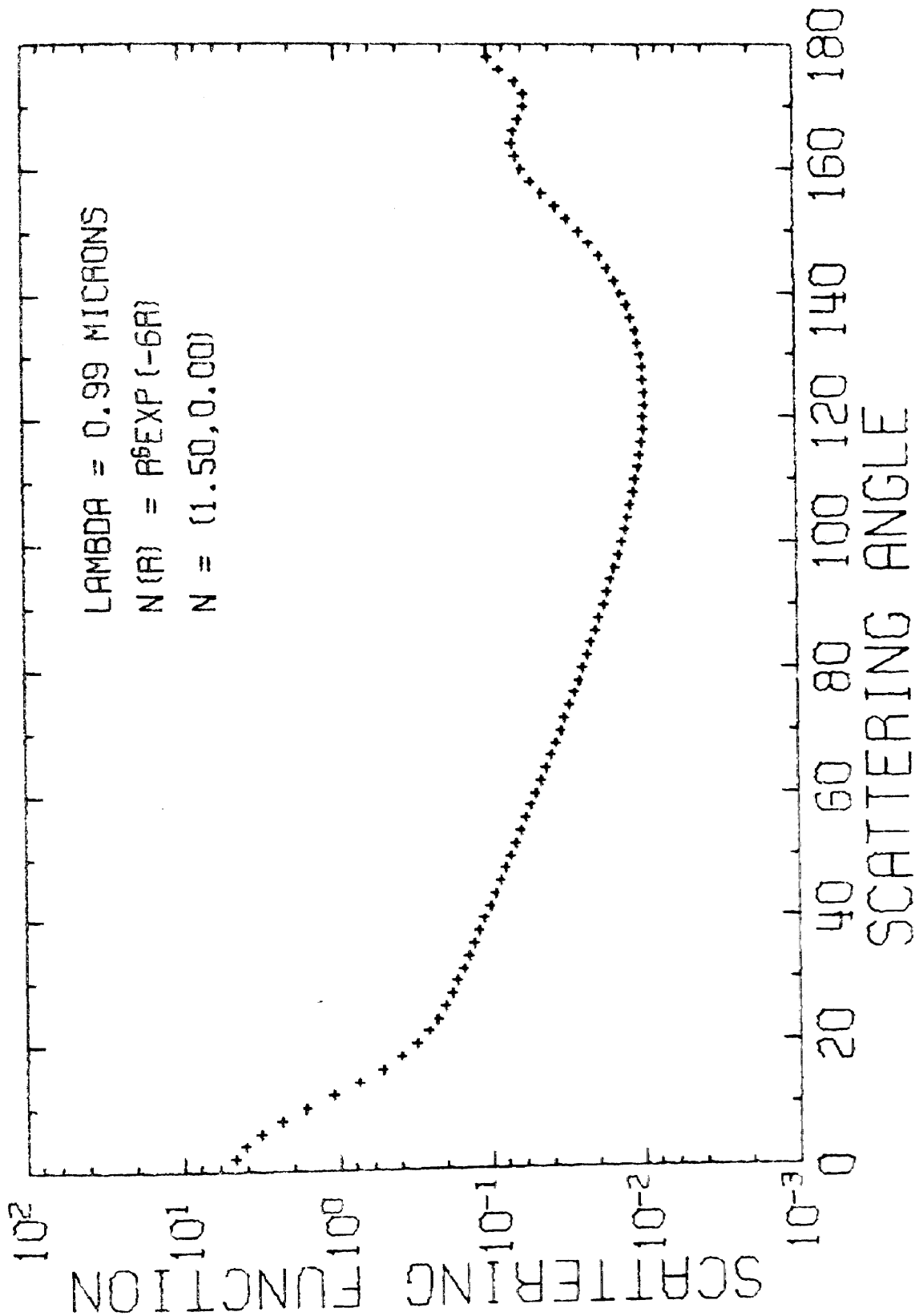


Figure 15 - Single scattering phase function for model M-1 at 0.99 μ

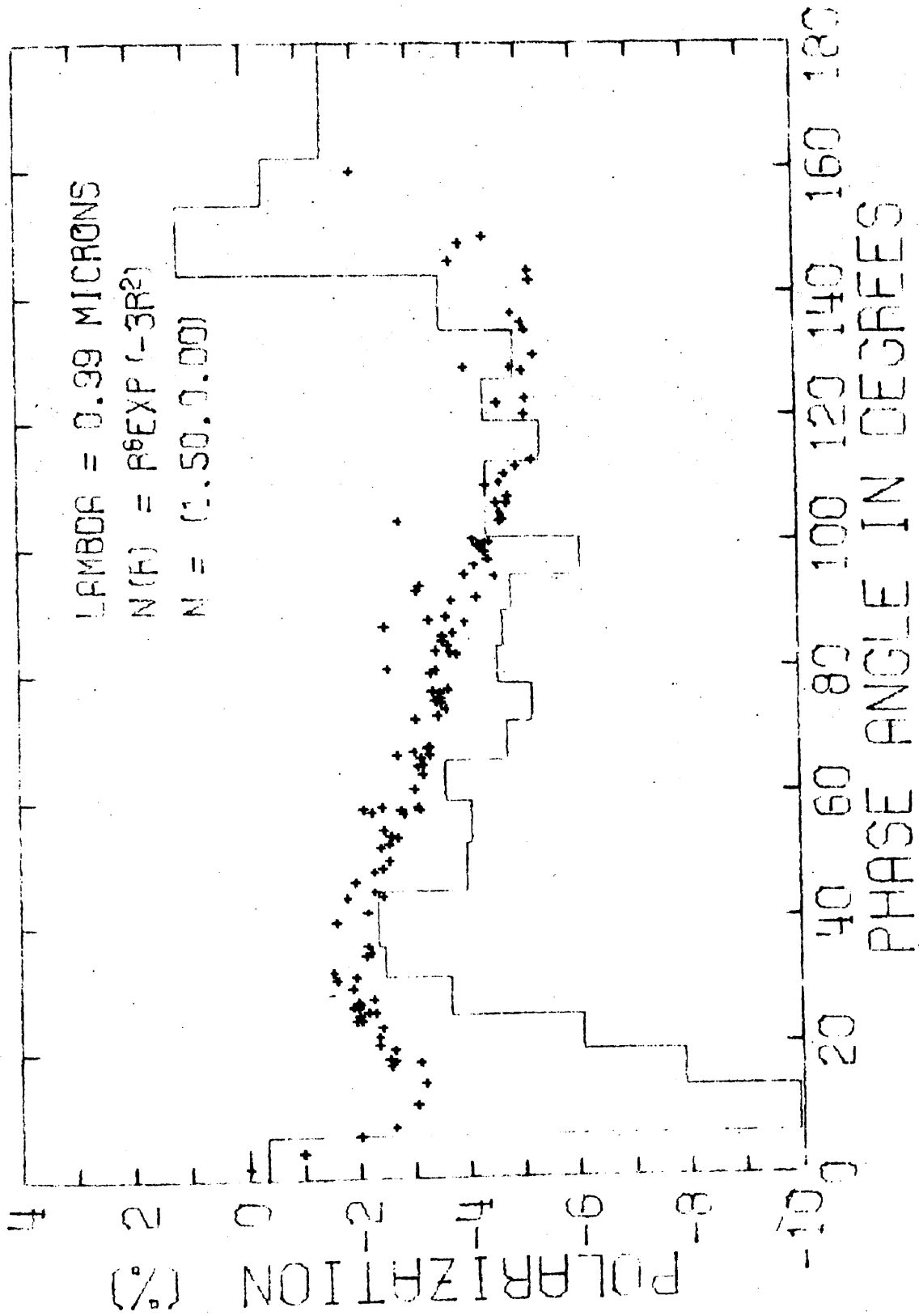
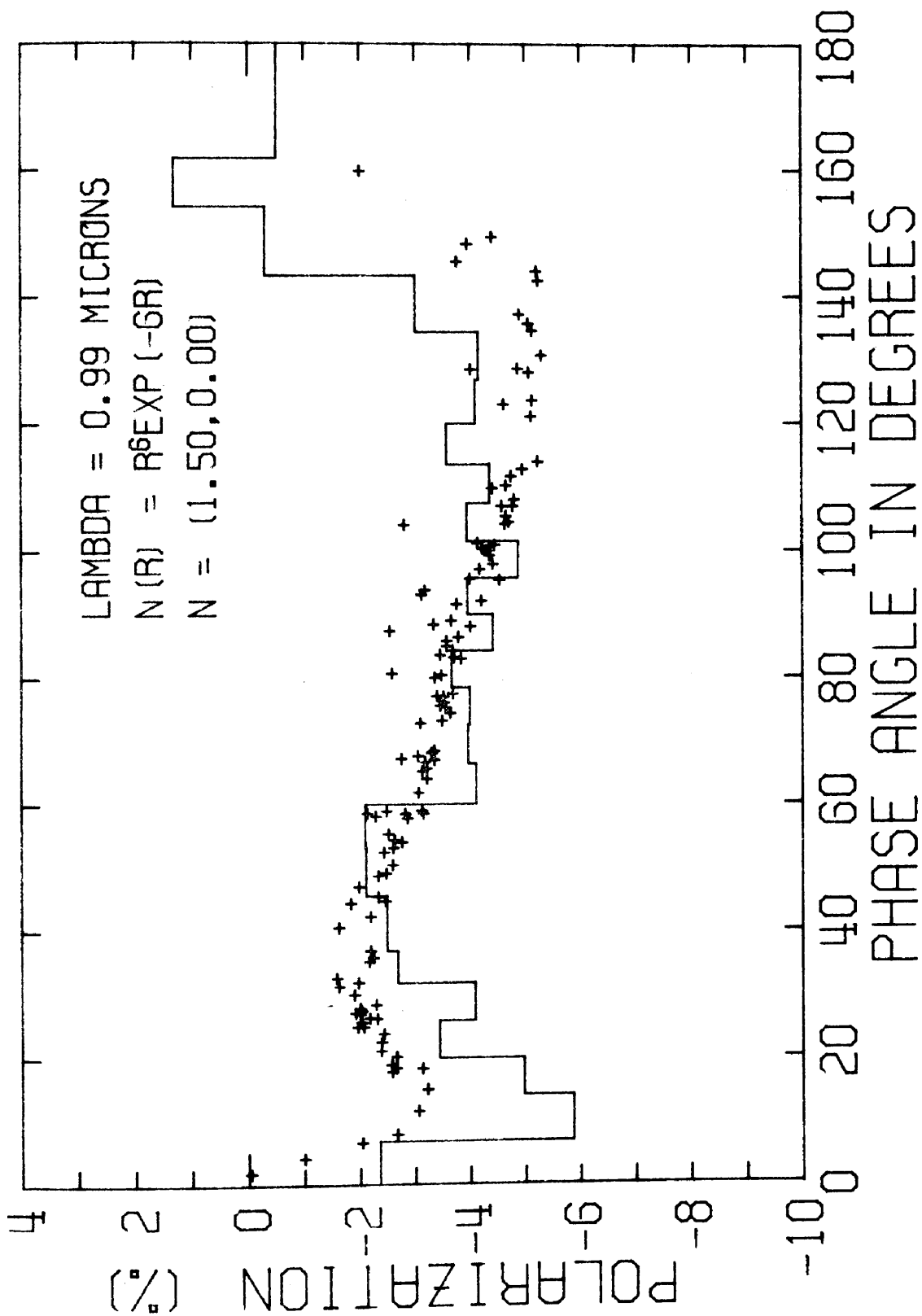


Figure 16 - Degree of polarization for model M-1 at 0.99 μ

Figure 17 - Monte Carlo results for model M-1 at 0.99 μ

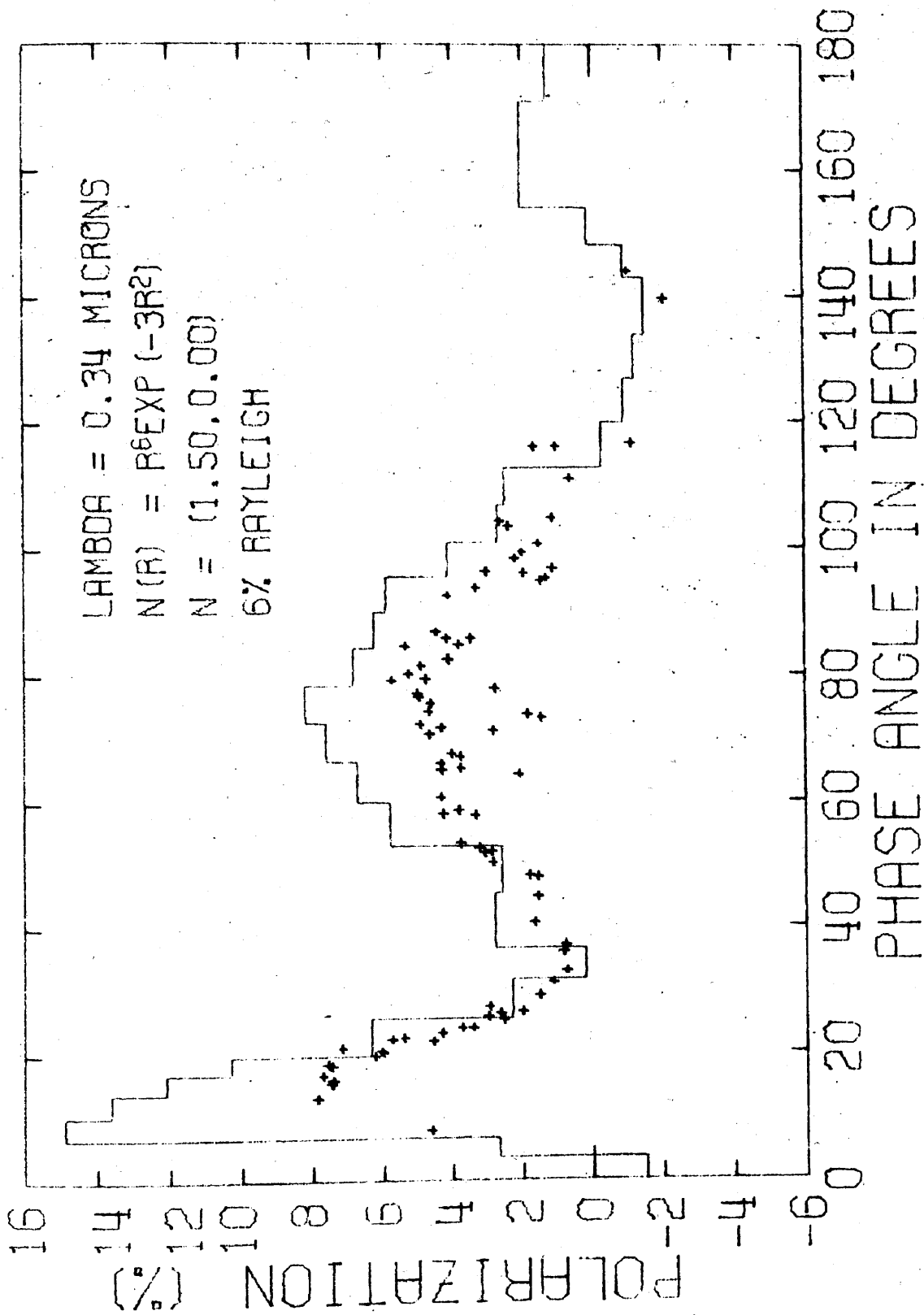


Figure 18 - Monte Carlo results for model M-2 at 0.34 μ with 6% Rayleigh

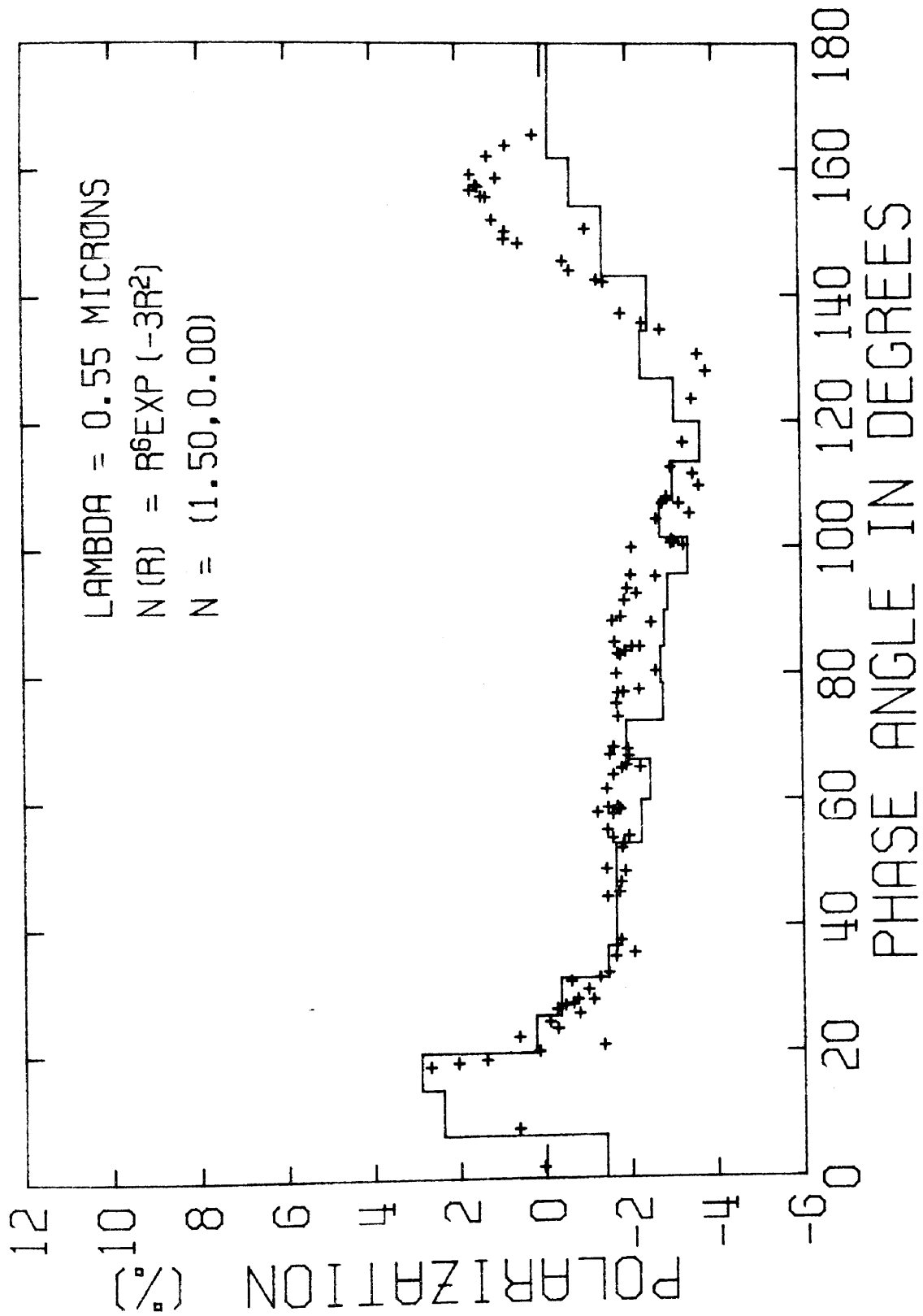


Figure 19 - Monte Carlo results for model M-2 at 0.55 μ

but the fit is poor in the region from 150° to 170° .

The results at 0.99μ are given in Figure 20. The minimum at 15° is much too low and the curve rises too rapidly from 140° to 160° .

c) Single Layer: Model-3 (M-3)

In this model the refractive index is $N_1=1.6$ and $N_2=0.0$ and the particle size distribution is given by

$$n(r) \propto r^6 e^{-4.2r}.$$

The distribution has a modal radius of 1.25μ and $\langle r \rangle = 1.46$. The results for 0.34μ are given in Figure 21. The maximum at 15° phase angle is too high and the calculated polarization falls more rapidly than the experimental data out to 30° . The region from 40° to 140° is fitted quite well with an 8% admixture of Rayleigh scattering.

At $\lambda=0.55\mu$ (see Figure 22) the first maximum is overestimated and from 50° to 110° the computed polarization is slightly too negative. The addition of 1.2% Rayleigh scattering which would still be prevalent at this wavelength would only raise the values about 5% around 90° , an amount barely visible on the scale of the figure. The one salient feature of this case is that the second maximum at about 160° in phase is reproduced quite well.

At 0.99μ (see Figure 23) the minimum in the polarization is too low and the curve rises too rapidly from 110° to 170° . Our study of the single scattering polarization curves for various

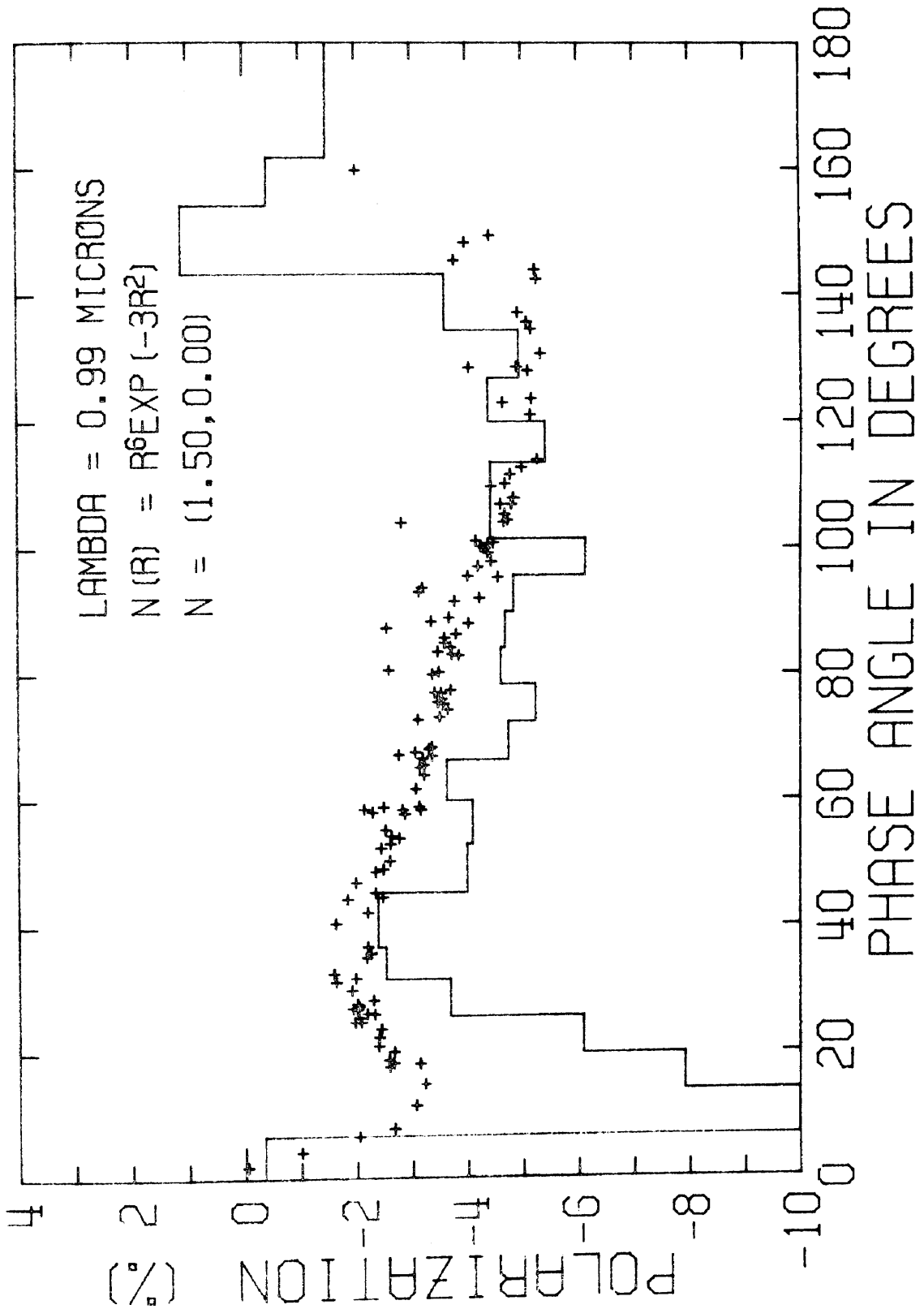


Figure 20 - Monte Carlo results for model M-2 at 0.99 μ

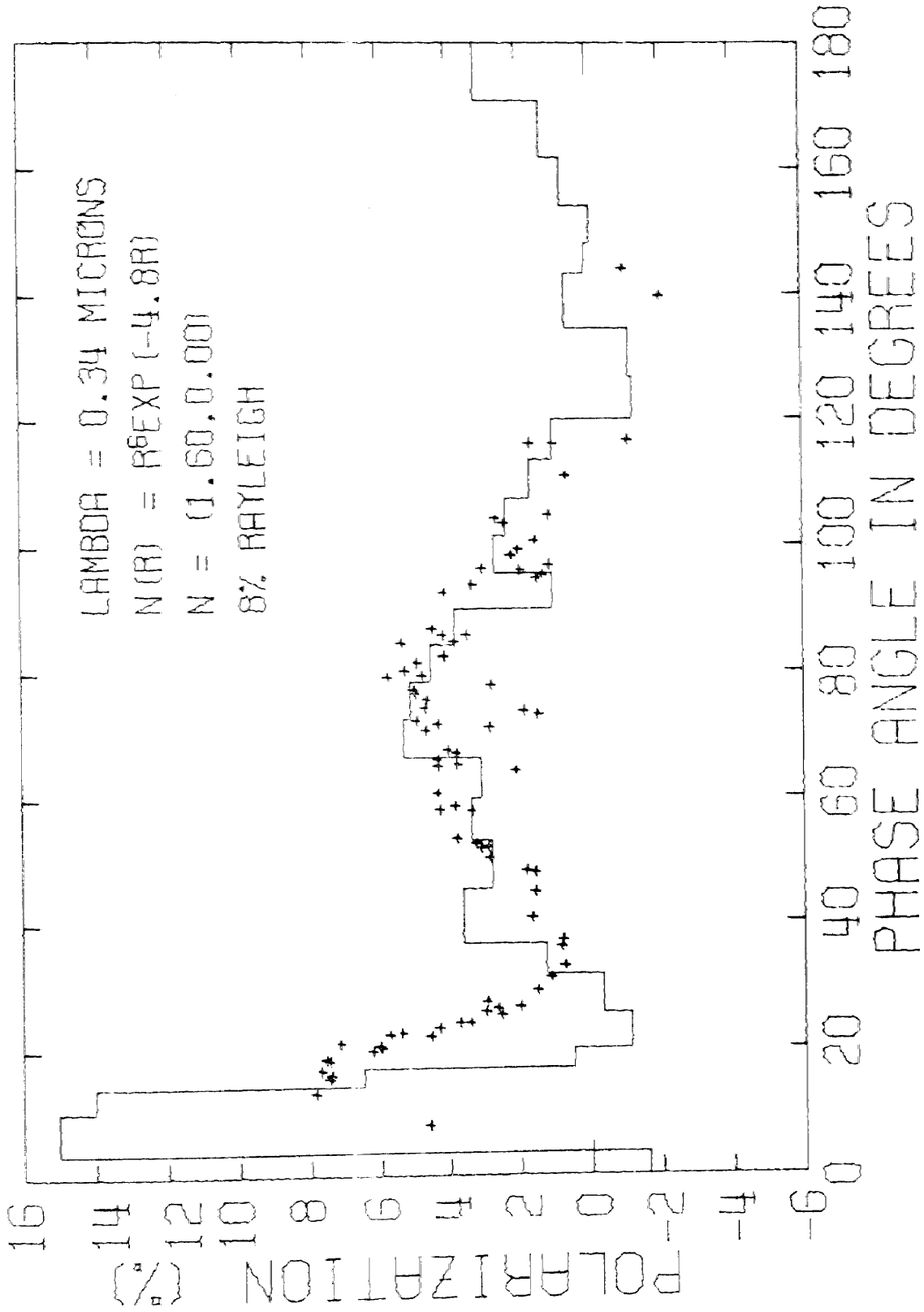


Figure 21 - Monte Carlo results for model M-3 at 0.34 μ

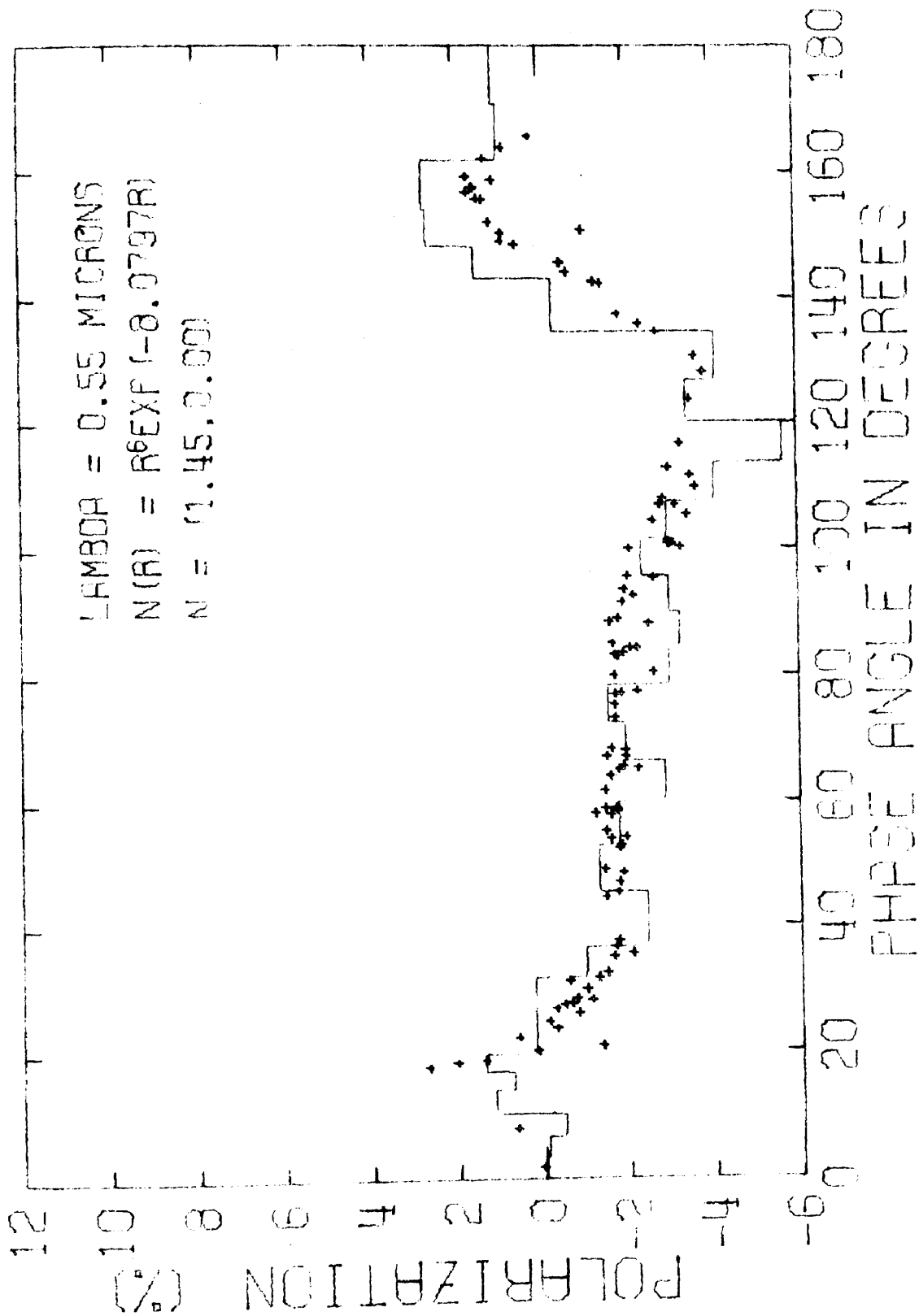


Figure 22 - Monte Carlo results for model M3 at 0.55 μ

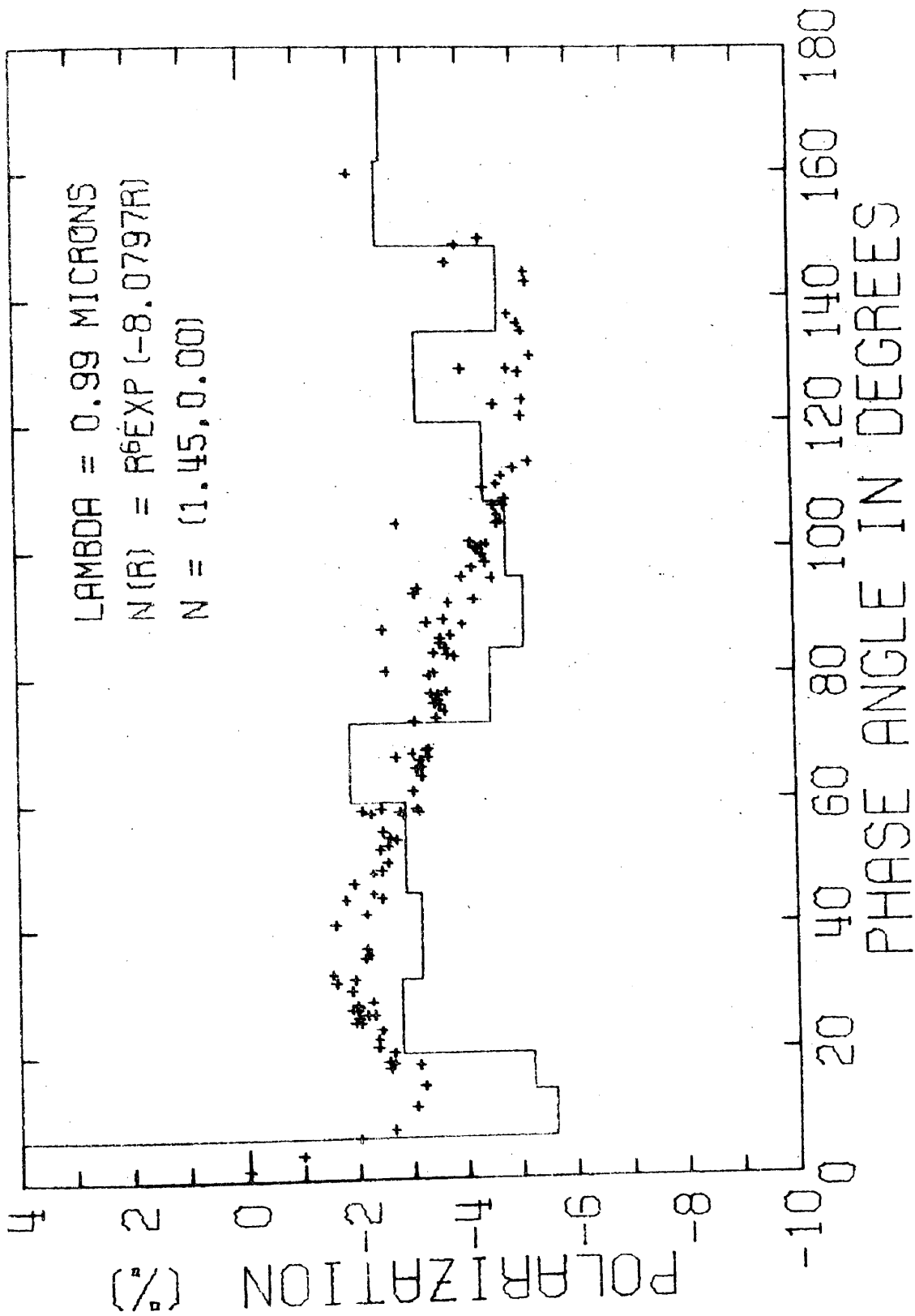


Figure 23 - Monte Carlo results for model M-3 at 0.99 μ

refractive indices and particle size distributions shows that, if one fits the minimum at 14° for 0.99μ , the first maximum is too high at 0.55μ for the same model.

d) Single Layer: Model-4 (M-4)

This model was selected so that the spherical Monte Carlo results could be checked against the plane parallel solutions of Hansen and Arking (1971) hereinafter referred to as HA. The particle size distribution selected is

$$n(r) \propto r^6 e^{-8.07972 r}$$

which has a modal radius $r_m = 0.743$ and $\langle r \rangle = 0.866\mu$. The value of $\bar{r} = 1.1$ at 0.55μ and varies with the wavelength. The index of refraction was taken as $N_1 = 1.45$ and $N_2 = 0.0$ to agree closely with the calculations of HA.

The Monte Carlo results at 0.34μ with an admixture of 6% Rayleigh scattering are shown in Figure 24. The value of \bar{r} at this wavelength is 1.04.

At 0.55μ (Figure 25) where $\bar{r} = 1.1$, the Monte Carlo results agree very well with the measurements. It is noteworthy that HA obtain a result for the second maximum at 160° which is too low, whereas, our spherical calculation agrees quite well with experimental observations. In this region the plane parallel approximation starts to break down and sphericity must be considered in order to avoid too much multiple scattering dilution of the polarization.

At 0.99μ (see Figure 26) where $\bar{r} = 1.1$ the spherical Monte Carlo

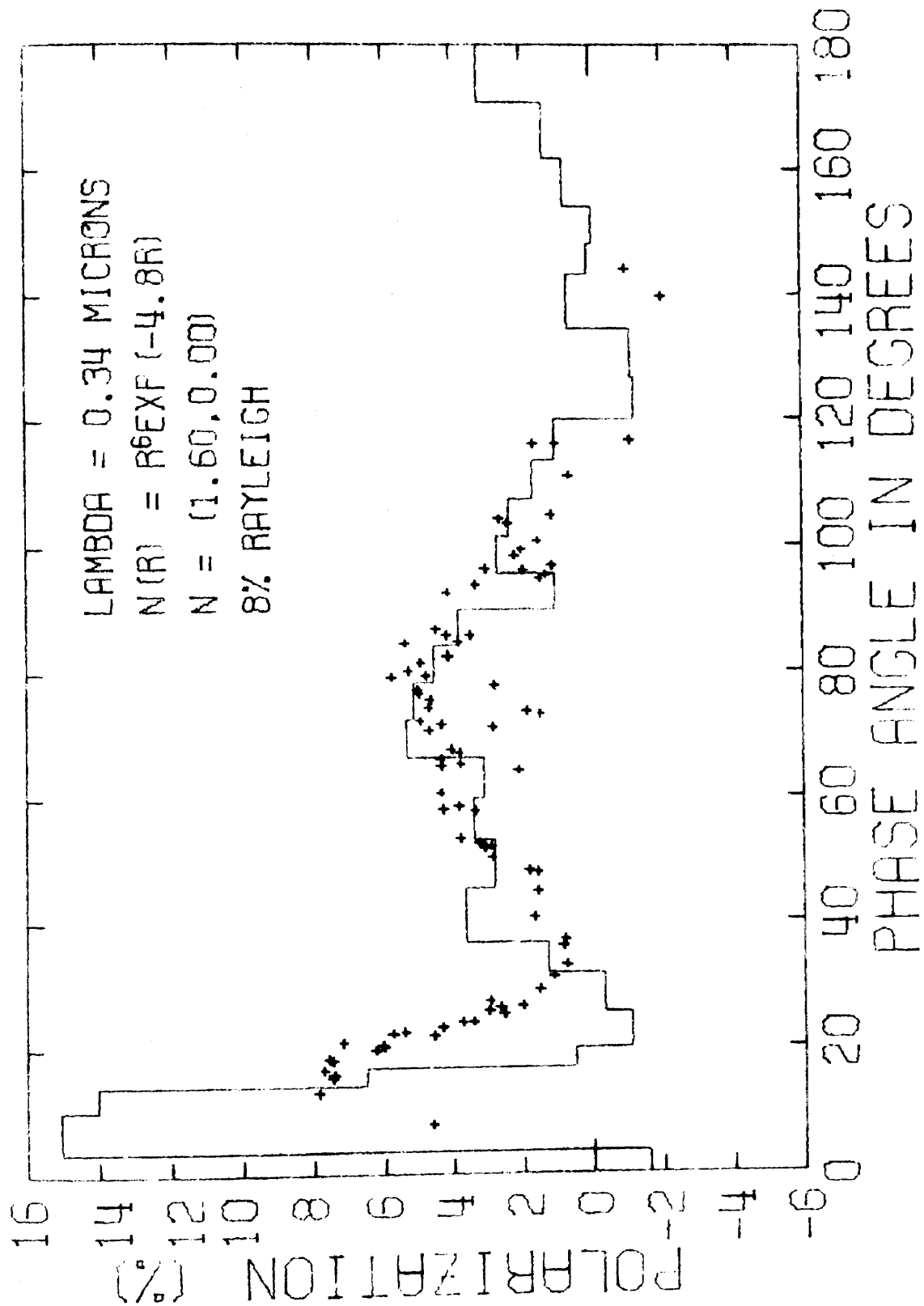


Figure 24 - Monte Carlo results for model M-4 at 0.34 μ

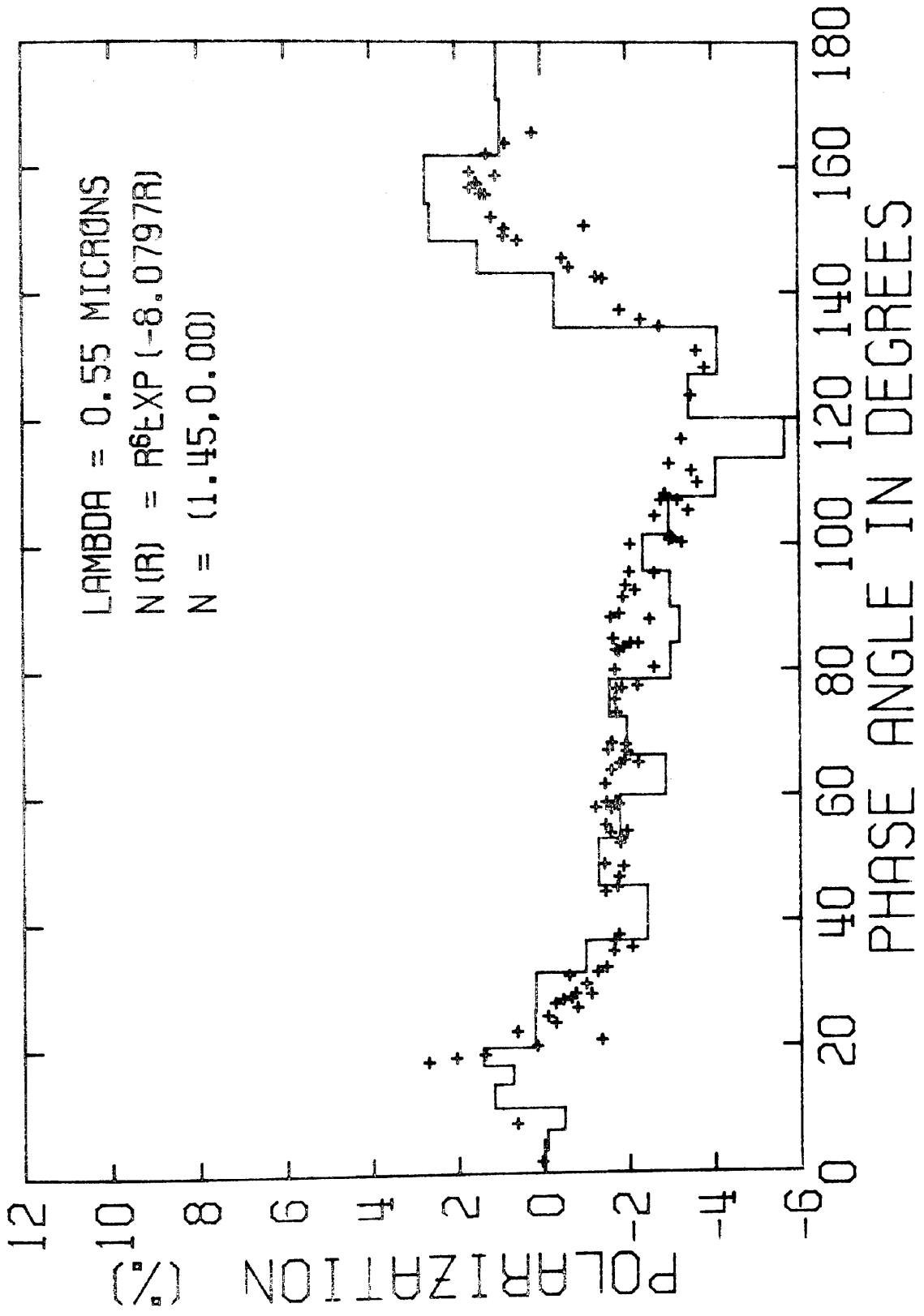


Figure 25 - Monte Carlo results for model M-4 at 0.55 μ

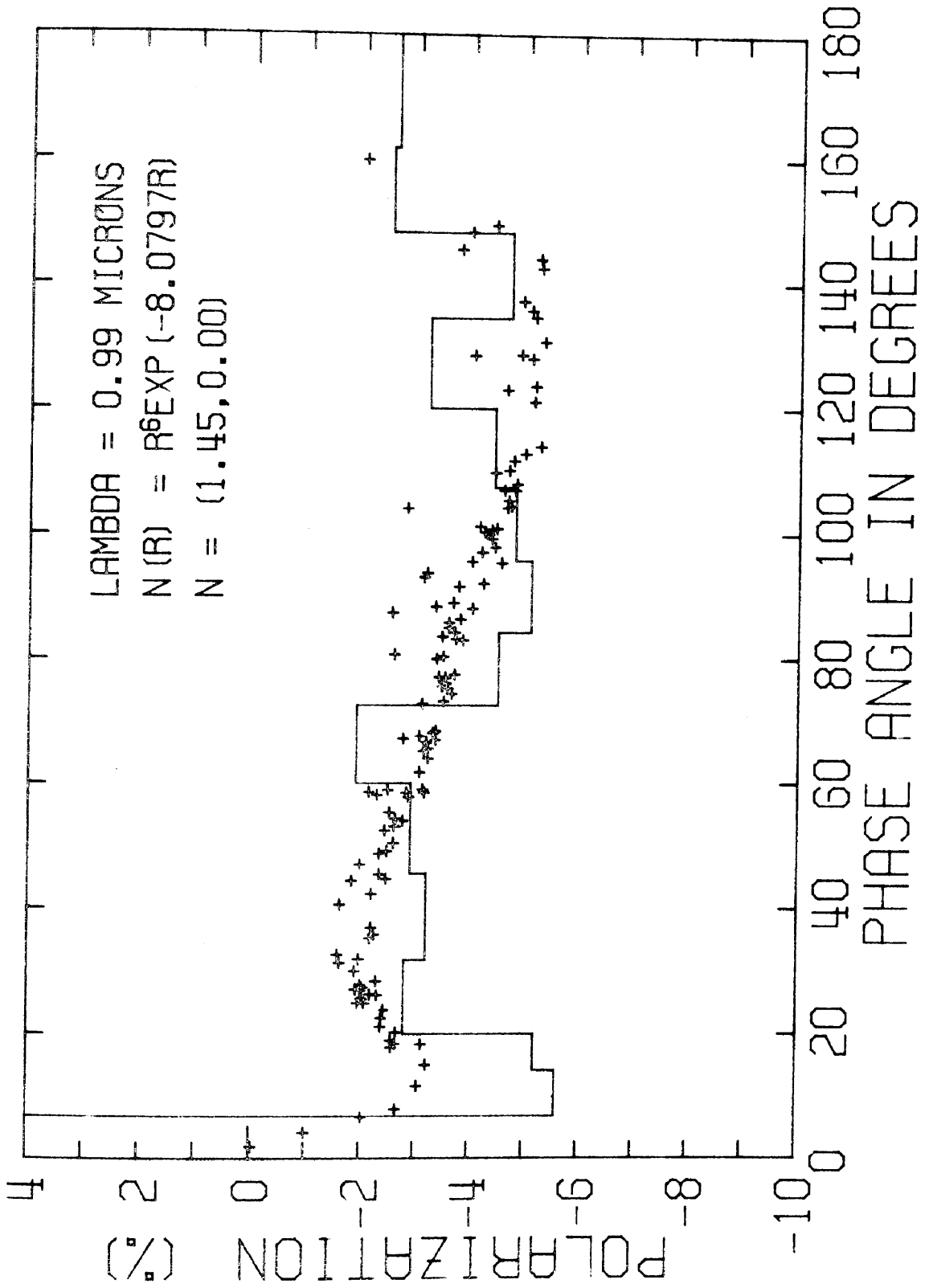


Figure 26 - Monte Carlo results for Model M-4 at 0.99 μ

calculations give a minimum which is too low, but the results for the remaining part of the polarization curve agree fairly well with observation. This minimum could be raised by going to a slightly smaller index of refraction, namely 1.44, as shown by HA.

e) Three Layers: Model-5 (M-5)

This model was selected on the basis of an analysis by Kuiper (1969). It incorporates three distinct layers each having a different refractive index, particle size distribution, and optical depth. The outermost layer was assumed to have the following properties at 0.34μ :

- 1) Optical depth $\tau = 0.2$;
- 2) Particle size distribution $n(r) \propto r^6 e^{-60r}$;
- 3) Refractive index: $N_1 = 1.64$, $N_2 = 0$;
- 4) Range: 6120 km to 6140 km.

The particle size distribution has a modal radius $r_m = 0.1$ and $\langle r \rangle = 0.117\mu$. This modal radius was selected since the UV clouds are visible at 0.36μ and apparently become invisible at larger wavelengths. The refractive index was chosen because of the possibility that sublimate NH_4Cl is present in the upper levels.

The optical properties of the middle layer were selected on the assumption (see Kuiper 1969) that the clouds are composed of $\text{FeCl}_2 \cdot 2\text{H}_2\text{O}$. The relevant parameters are as follows:

- 1) Optical depth $\tau = 0.5$;
- 2) Particle size distribution $n(r) \propto r^6 e^{-6r}$ homogeneously

mixed with 8% Rayleigh scattering;

- 3) Refractive index: $N_1=1.5$; $N_2=0.0$;
- 4) Range: 6110 km to 6120 km.

Finally the lowest layer was chosen to have optical properties consistent with FeCl_2 . They are as follows:

- 1) Optical depth $\tau = 50.0$;
- 2) Particle size distribution $n(r) \propto r^6 e^{-6r}$;
- 3) Refractive index: $N_1=1.6$; $N_2=0.0$;
- 4) Range: 6050 km to 6110 km.

The results of this calculation at 0.34μ are presented in Figure 27. The maximum around 15° phase angle agrees well with observation; however, the calculated polarization falls off too rapidly beyond this point. This rapid decline is due to both the lowest layer ($N_1=1.6$) and the upper layer ($N_1=1.64$) which have regions of strong negative polarization at these scattering angles. The remaining portion of the polarization curve beyond a phase angle of 30° is fitted fairly well.

In extending the calculation to 0.55μ , account was taken of the fact that the optical thickness of the layers changes due to the cross section versus wavelength dependence. The results are shown in Figure 28. It should be noted that the computed values lie above the experimental values from about 70° to 140° in phase angle. This was due to the fact that the single scattering polarization curve for the top layer ($N_1=1.64$; $N_2=0$) was positive in this region.

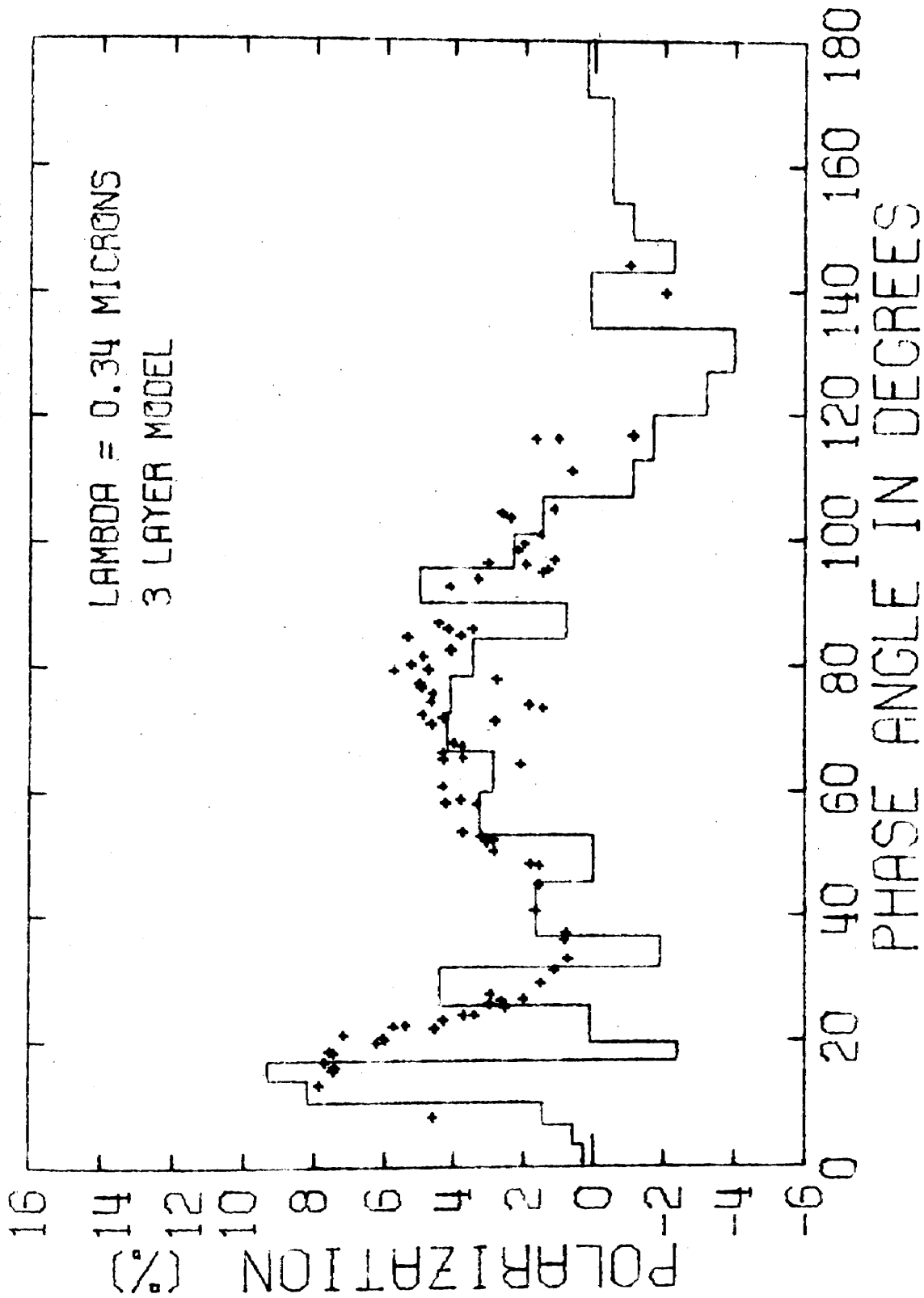


Figure 27 - Monte Carlo results for model M-5 at 0.34 μ

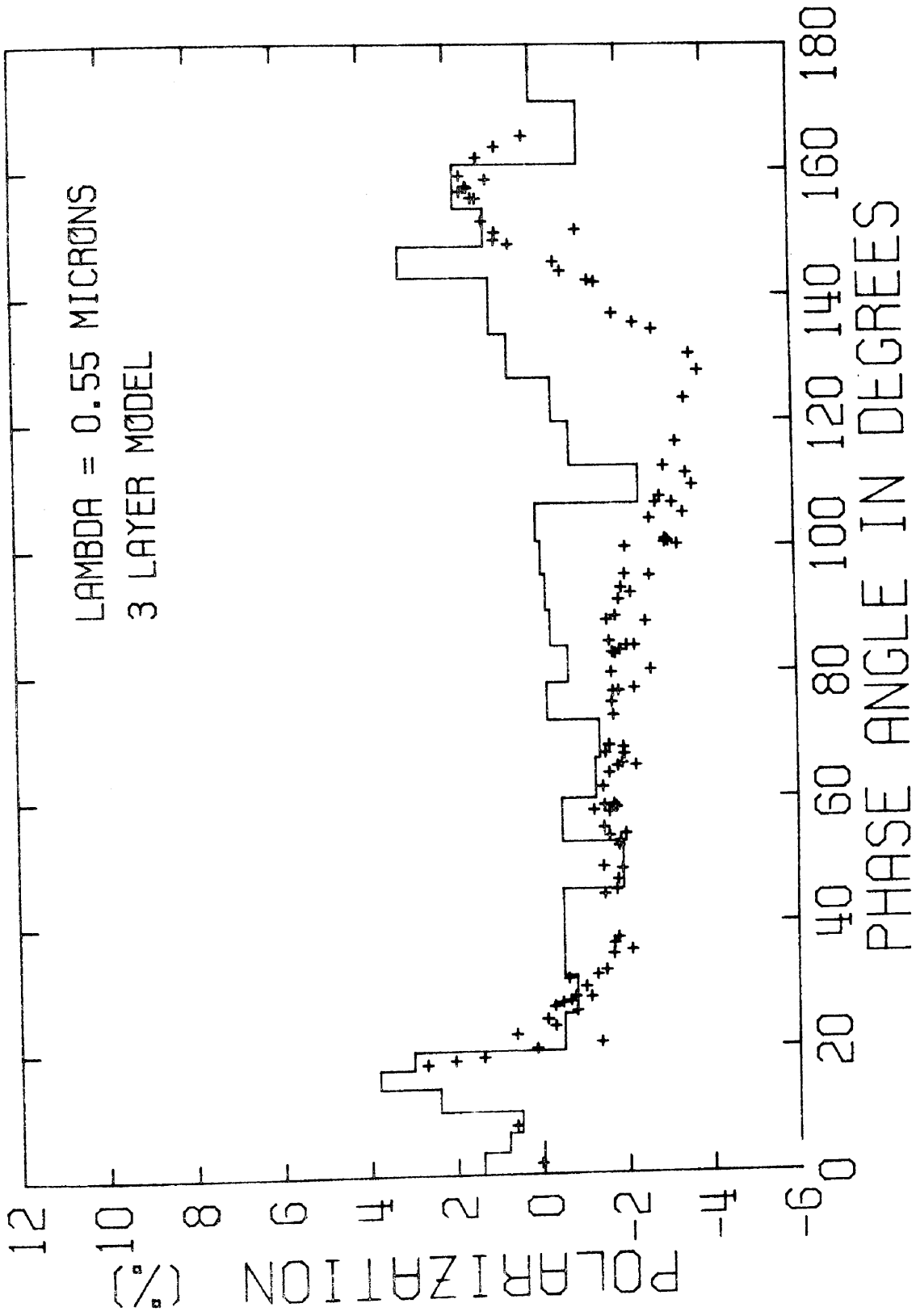


Figure 28 - Monte Carlo results for model M-5 at 0.55 μ

The calculations for 0.99μ , again with an appropriate adjustment in the optical thickness of the layers, are presented in Figure 29. Again the discrepancy from 70° to 170° is due to the strong positive polarization of the top layer; at this wavelength it is in the Rayleigh region.

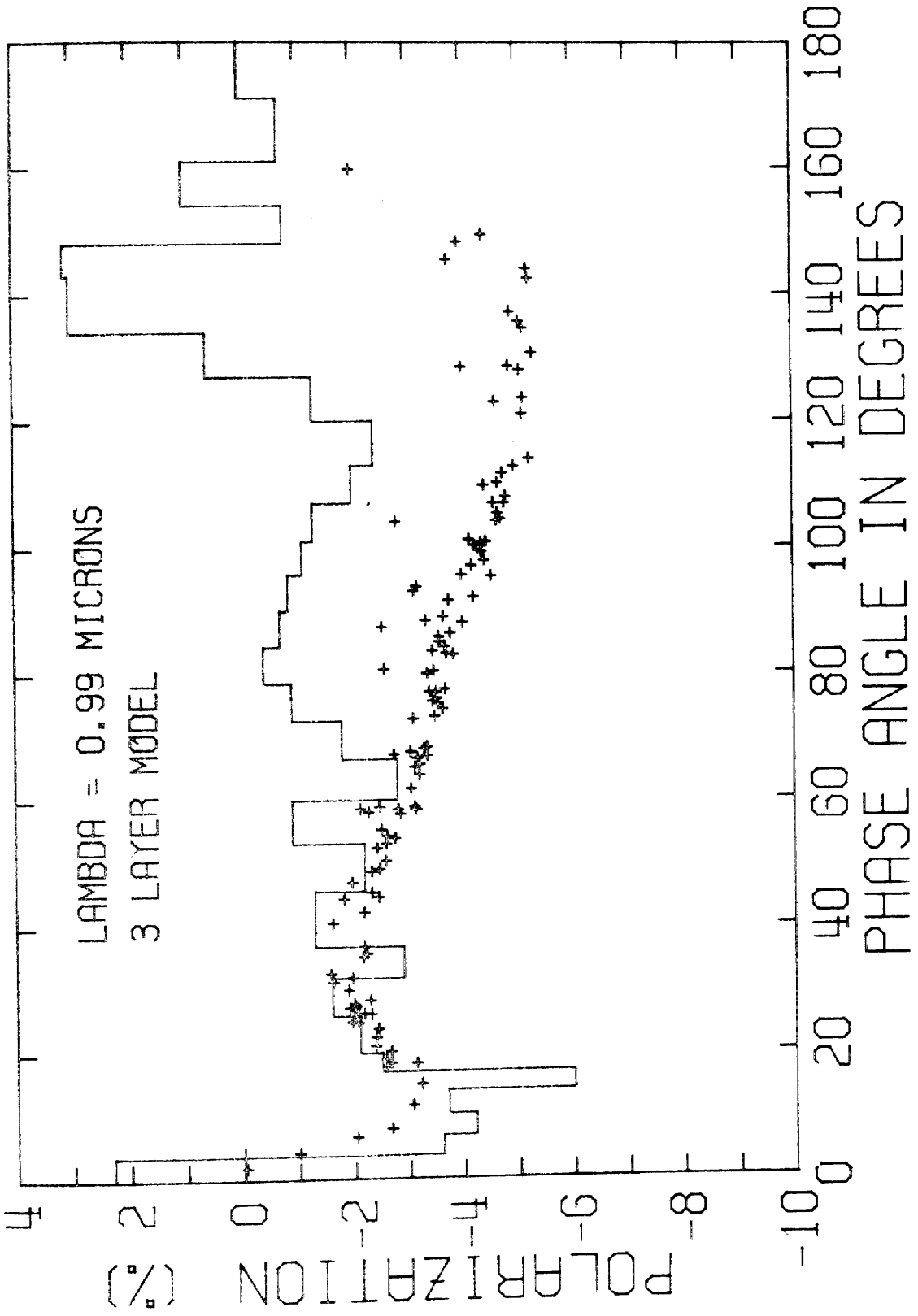


Figure 29 - Monte Carlo results for model M-5 at 0.99 μ

VII. CONCLUSION

At 0.34μ the calculated value of the polarization at the maximum near 15° agrees best with observation for models M-4 and M-5. The polarization for phase angles greater than 20° agrees reasonably well for models M-3 and M-5 with an admixture of 8% Rayleigh scattering and for models M-1, M-2, and M-4 with a 6% admixture.

At 0.55μ the calculated polarization near the first maximum agrees quite well with the observational value for models M-2, M-4, and M-5, but is too large for models M-1 and M-3. The values for phase angles from 20° to 140° agree well for models M-1, M-2, and M-4, but the calculated curve lies above the observational curve for model M-5 and below for model M-3. The best agreement near the maximum at 155° is for model M-3 with good agreement for models M-1 and M-4.

At 0.99μ model M-5 gives the best agreement near the minimum at 15° . The best agreement from 20° to 140° is for models M-1 and M-4, with models M-2 and M-3 also in fair agreement. The observational curve is not well defined beyond 150° , but all calculated curves seem to lie above the experimental points with the exception of model M-4.

No one model fits all of the features of the experimental curves at each of the wavelengths. Perhaps the best overall fit is given by models M-4 and M-5 at 0.34μ , models M-2 and M-4 at 0.55μ , and

model M-4 at 0.99μ . The best fit at all three wavelengths is given by model M-4 which provides good overall agreement with the measurements except near the minimum in the vicinity of 15° at 0.99μ . This discrepancy may be connected with the assumption of spherical particles. Measurements by Holland and Gagne (1970) have shown that the scattering from irregular shaped particles can differ appreciably from the Mie theory at certain angles (but see discussion by Plass and Kattawar (1971)). Many of the assumed particles in the Venus atmosphere would have non-spherical forms, i.e. the $\text{FeCl}_2 \cdot 2\text{H}_2\text{O}$ particles assumed by Kuiper are platelets. A study of scattering from such irregular shapes may be necessary to completely solve this problem.

The actual atmosphere of Venus is probably composed of several layers with different types of scattering centers predominating in each layer. It is dangerous to draw definite conclusions on the particle size and index of refraction based on calculations made for a single layer (Hansen and Arking, 1971), Model M-5 has three different layers. It may be necessary to consider at least several layers with different scattering properties in any realistic model. This has not been pursued further here, since there are few restrictions known at the present time on the optical depth and scattering properties of each layer. More experimental information is needed to limit the number of choices.

Any constituent that is a major component in the scattering of photons in the Venus atmosphere appears to have a refractive index

in the range from 1.45 to 1.6 and to be composed of particles with an equivalent mean radius of about 1μ .

VIII. TWILIGHT

Numerous difficult problems arise in the study of twilight in the earth's atmosphere whether by theoretical techniques or physical measurements. Each physical sunrise and sunset is unique, unrepeatable, and highly dynamic. The dynamic changes in intensities and spectral distributions (the observed color) as a function of viewing angle and relative position of the observer to the sun produce many problems in equipment construction and rapid data accumulation and analysis. Furthermore, the observer does not know what viewing angles may yield the most useful information at a given time.

The theoretical calculations for simple atmospheric models are repeatable, but may not reproduce all that is physically observed. This is to be expected. The relatively simple treatment of assuming that the photons are scattered only once required an appreciable amount of computer time on the CDC 7600 high speed digital computer and produced a proportional amount of information to be processed. More suitable results may be obtained by the addition of multiple scattering effects by the use of Monte Carlo techniques.

Hulburt (1953) attempted to determine quantitatively the brightness and color of the twilight sky. He showed the importance of ozone in determining the blue color of the zenith twilight sky.

Rozenberg (1963) has examined these problems in great detail in his book. Most of his discussion is essentially qualitative and is based on approximate equations whose validity is difficult to assess. All of his results are for a single scattering model with no refraction.

The most recent and comprehensive article on the subject is by Dave and Mateer (1968). They show colorimetry results for five atmospheric models (similar to the ones described here), but do not include any refraction or multiple scattering effects. A similar treatment is used in the following calculations with the important difference that the refraction of the light rays is taken into account.

IX. COMPUTATIONAL TECHNIQUES

The geometry of the problem for the solution of the observed radiance at a point P on the earth's surface is illustrated in Figure 30. The quantity y in the figure is the minimum height of the direct solar beam above the earth's surface if there were no refraction (while h_m is the same quantity when refraction is considered). The radius of the earth R_e is taken as 6371 km in the calculation.

The radiance I_λ of the single scattered radiation as received by the observer at point P on the earth's surface is given by the equation

$$I_\lambda(\theta_0, \theta) = \int_0^\infty (\beta_R P_R(\mu) + \beta_M P_M(\mu)) F_S(\lambda) T_p ds, \quad (83)$$

where

θ_0 = solar zenith angle with respect to the vertical of the observer.

θ = local zenith viewing angle for the observer.

β_R = volume scattering coefficient for Rayleigh scattering.

$P_R(\mu)$ = Rayleigh phase function for scattering angle μ .

β_M = volume scattering coefficient for aerosol scattering.

$P_M(\mu)$ = aerosol phase function for scattering angle μ .

$F_S(\lambda)$ = incident solar flux upon scattering volume. This

may be written as the product of $F_0(\lambda, s)T_s$, where T_s is fraction of direct solar beam incident upon the scattering point and $F_0(\lambda, s)$ is the product of the extra terrestrial solar flux at wavelength λ and a factor due to the divergence of the solar beam as it is refracted through the atmosphere. The extra terrestrial solar flux is taken to be unity for the calculations of radiance and then weighted by actual solar values for colorimetry calculations.

T_p = fractional transmission of scattered light from the scattering point to the observer.

The formulas for T_s and T_p are given by

$$T_s = \exp \left(- \int_0^L (\beta_R(\lambda) + \beta_3(\lambda) + \beta_m(\lambda)) d\lambda \right) \quad (84)$$

and

$$T_p = \exp \left(- \int_0^S (\beta_R(s') + \beta_3(s') + \beta_m(s')) ds' \right) \quad (85)$$

where

β_3 = volume absorption coefficient for ozone as given by Elterman (1968).

L = total distance traversed by photon from point of entrance into the model atmosphere to scattering point along the curved path.

S = total distance from observation point to scattering point along the line of sight.

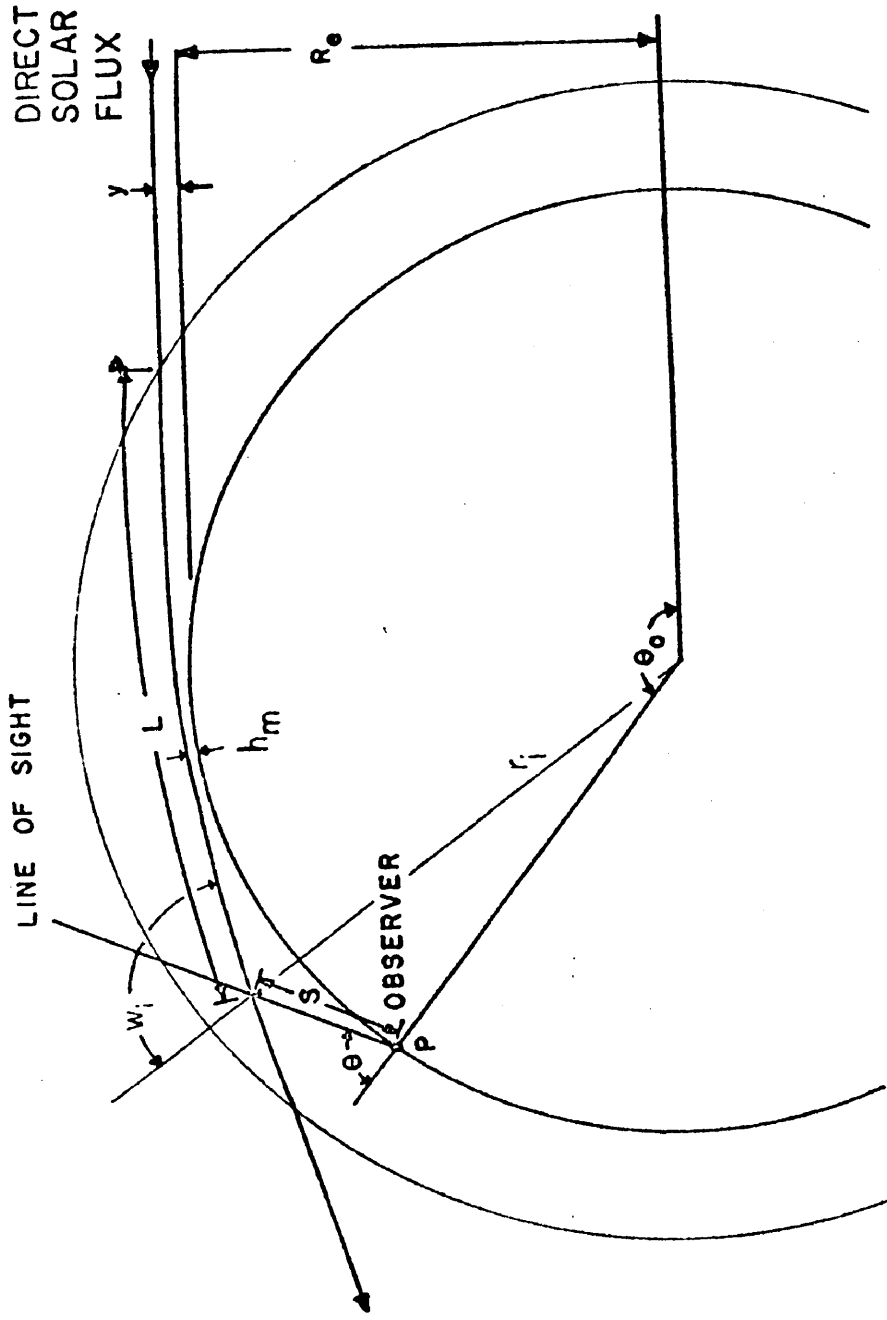


Figure 30 - Geometry of direct solar flux to scattering point on
Line of sight and then to observer on the surface of the earth

The integral in (83) was evaluated by Simpson's rule from the single scattering contributions at the points of intersection of the solar rays with the line of sight from the observer. The integrals in (84) and (85) were reduced to sums of products of extinction coefficients and distances traversed through the atmospheric layers of the model.

The aerosol phase function, $P_m(\mu)$, used throughout these calculations was calculated from Mie theory for a Haze C model with particle size density distribution proportional to r^{-4} , where r is particle radius in microns. This phase function was obtained for the wavelengths needed from a computer code developed by Kattawar and Plass (1967) in previous work involving studies of aerosols. An index of refraction of $(1.55 + 0.0i)$ was used to approximate that of atmospheric dust in the earth's atmosphere. No change in particle size distribution was assumed as a function of height in the atmosphere.

It is essential in this type of computation to determine when a sufficient number of atmospheric zones have been employed and secondly to determine when a sufficient number of photons have been processed. To test the first condition the quantity $n(r) r \sin(w)$ was calculated where

$n(r)$ = refractive index at position r

r = distance to ray from center of earth

w = angle of incidence of ray path with radius vector at position r .

This quantity should be a constant along any ray path and is easily established from Fermat's principle. The first extensive use of this result applied to atmospheric refraction was by McLeod (1919). Similar results were also obtained by Goody (1963). Testing this quantity for several different ray paths yielded a maximum error of one part in 10^{10} . To test the second condition the number of photons was increased until further doubling produced an average error in the total integrated radiance of less than one percent over all look angles and observer positions.

The values used in these calculations are from the tables of Wyszecki and Stiles (1967). These values may be found in most texts on optics.

The tristimulus values X , Y , and Z are obtained from the standard luminosity functions \bar{x}_λ , \bar{y}_λ , and \bar{z}_λ for a particular spectral distribution of radiant flux represented by $I_\lambda d\lambda$ from the equations

$$\begin{aligned} X &= \int I_\lambda \bar{x}_\lambda d\lambda \\ Y &= \int I_\lambda \bar{y}_\lambda d\lambda \\ Z &= \int I_\lambda \bar{z}_\lambda d\lambda \end{aligned} \quad (86)$$

Finally the chromaticity coordinates x , y , and z are obtained from the expressions

$$\begin{aligned} x &= X (X+Y+Z)^{-1}, \\ y &= Y (X+Y+Z)^{-1}, \\ z &= Z (X+Y+Z)^{-1}. \end{aligned} \quad (87)$$

Since the sum of x , y , and z is unity, only two of the chromaticity coordinates need be specified.

The chromaticity coordinates for twilight were calculated from the radiance calculated from (83) and substituted in (86) and (87). The radiance was calculated for the wavelengths 0.40μ [0.05] 0.75μ . Since the radiance is a slowly varying function of wavelength, the calculated values were fitted by a cubic spline routine in order to obtain radiance values for any wavelength in this interval. These radiance values were weighted with the solar spectral irradiance distribution at the top of the atmosphere as given by Thekaekara (1972) and by the appropriate standard luminosity functions. Thus the integral in (86) was calculated and finally the chromaticity coordinates were obtained from (87).

X. ATMOSPHERIC MODELS

Five different atmospheric models were used for the calculations which are referred to as models A, B, C, D, and E. These models have the following characteristics: A, pure molecular scattering; B, molecular scattering plus ozone absorption; C, molecular scattering, ozone absorption, and normal aerosol concentration as tabulated by Elterman (1968); D, as model C, but with three times normal aerosol concentration; E, as model C, but with ten times normal aerosol concentration.

The model atmosphere is assumed to have concentric spherical shells of thickness 1 km from the radius of the earth, R_e , to $R_e + 400$ km and shells of thickness 5 km from an altitude of 400 km to 500 km. Atmospheric parameters are taken as constant in each layer. The density values are obtained from the U. S. Standard Atmosphere 1962, Anonymous (1965). Atmospheric extinction coefficients for Rayleigh, ozone, and aerosol scattering are obtained from the tables of Elterman (1968) for altitudes up to 50 km. Above this altitude Rayleigh extinction coefficients are calculated from density values obtained from the U. S. Standard Atmosphere 1962, ozone extinction coefficients are assumed to be zero, and aerosol extinction coefficients are assumed to decrease from 50 to 80 km with the same scale height as from 40 to 50 km. The number

density of the aerosols is held constant from 80 to 90 km in order to simulate an aerosol layer. Above 90 km the aerosol number density decreases with the same scale height already used. The calculated optical thickness of the entire atmosphere in the zenith direction as a function of wavelength is shown in Figure 31 for each of the five models.

The shadow height for a given line of sight of the observer is defined as the vertical height to the point along the line of sight that intersects the path of a solar photon that just grazes the earth's surface. The shadow height is shown in Figure 32 as a function of the zenith angle θ of the line of sight taken as positive in the solar direction and negative in the antisolar direction. Each curve is for a particular value of θ_0 which defines the observer's position on the earth's surface with respect to the solar direction (see Figure 30). The solid curves give the shadow height when refraction effects are taken into account and the dashed curves are calculated without refraction. The dashed curves agree well with the results of Rosenberg (1963). In many cases there is an important change in the shadow height when refraction is taken into account. These decreased shadow heights may increase the radiance contributions from lower altitudes, particularly at longer wavelengths where the atmosphere is more transparent. This in turn may change the calculated colorimetry values where a major portion of the total contribution is within this region.

As another example of the importance of refraction, particularly

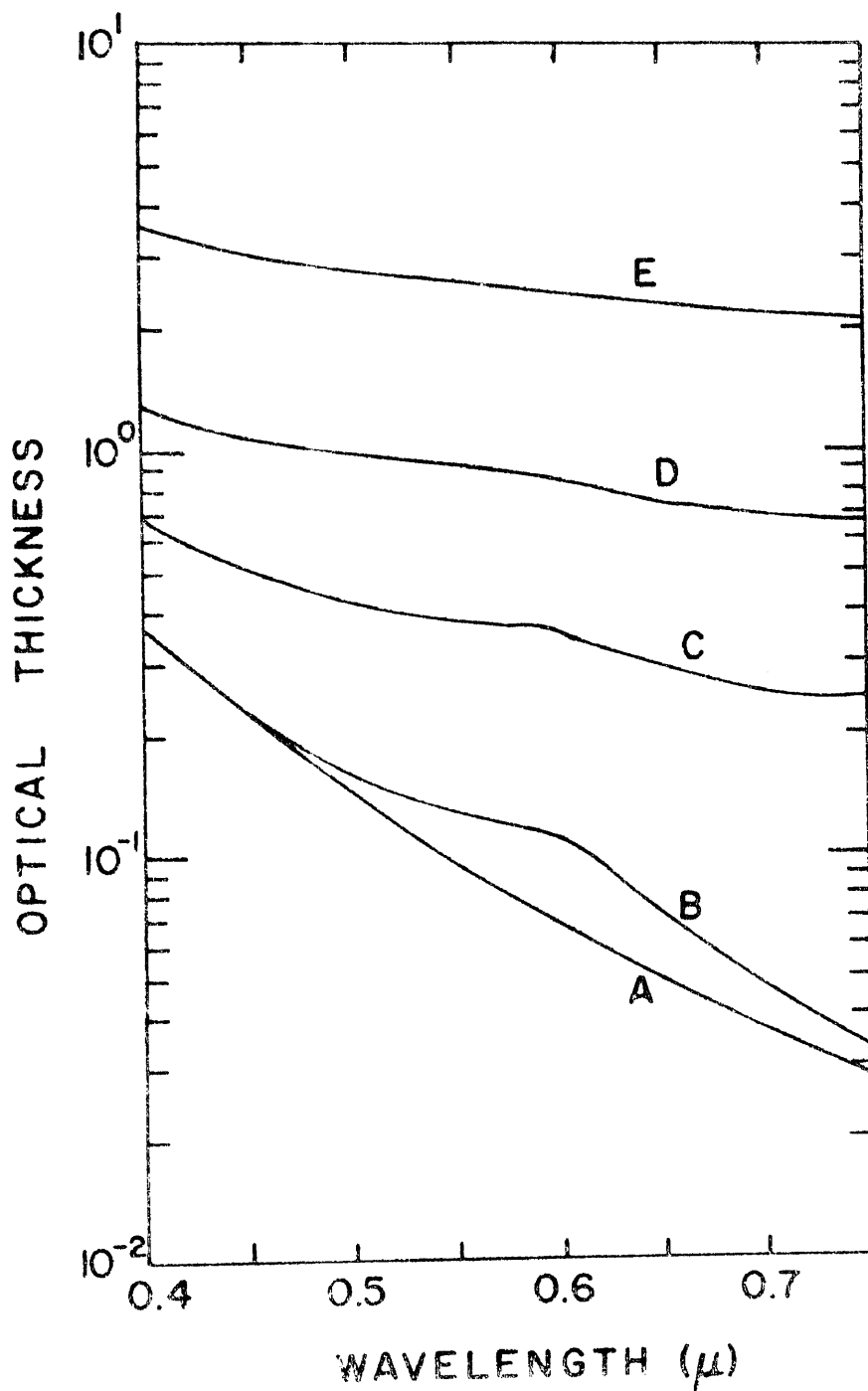


Figure 31 - Optical thickness through the entire atmosphere in a vertical direction as a function of wavelength for Models A-E

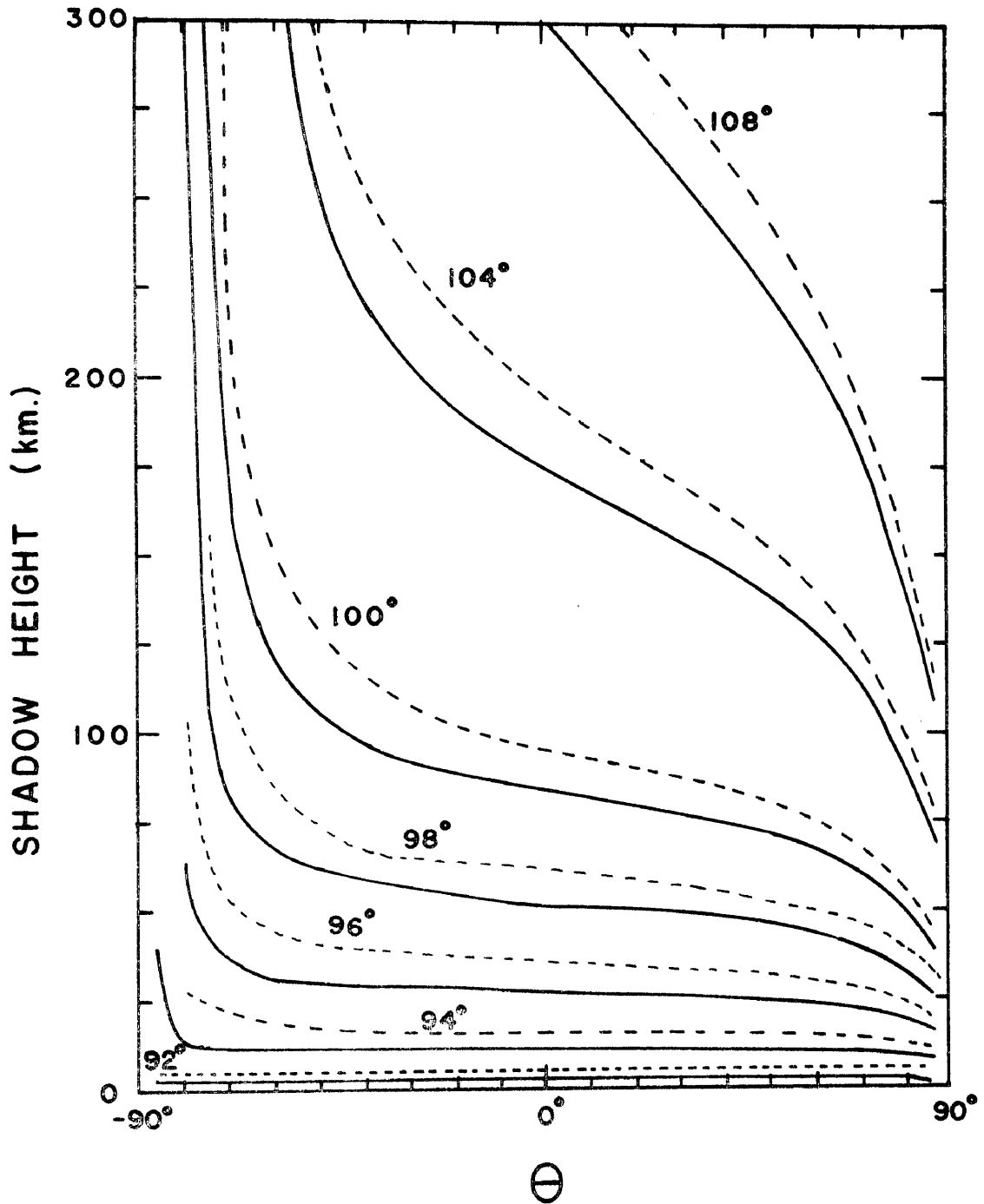


Figure 32 - Shadow height in km as a function of θ , the zenith angle of observation

for the rays that come close to the earth's surface, consider an observer at the terminator ($\Delta_0 = 90^\circ$) viewing an unrefracted solar ray at the zenith ($\theta = 0^\circ$) that intersects the line of sight at an altitude of 2 km. The refracted ray intersects the line of sight instead of 0.55 km. When looking in the antisolar direction so that $\theta = -85^\circ$, the same unrefracted and refracted rays intersect the line of sight at 2.04 km and 0.51 km respectively.

The transmission from outside the atmosphere to the perigee point is shown in Figures 33 and 34 for $\lambda = 0.45\mu$ and 0.75μ respectively. The transmission for Model A is much greater at $\lambda = 0.75\mu$ than at 0.45μ because of the strong wavelength dependence of Rayleigh scattering. The ozone absorption is small at $\lambda = 0.45\mu$ and the difference between the curves for Models A and B cannot be shown on the scale of the figure. The transmission is always less at a shorter wavelength than at a longer when a given model and perigee height are compared. The greatest changes between these figures occur in those regions of Figure 34 with relatively high transmission and a perigee height near the earth's surface.

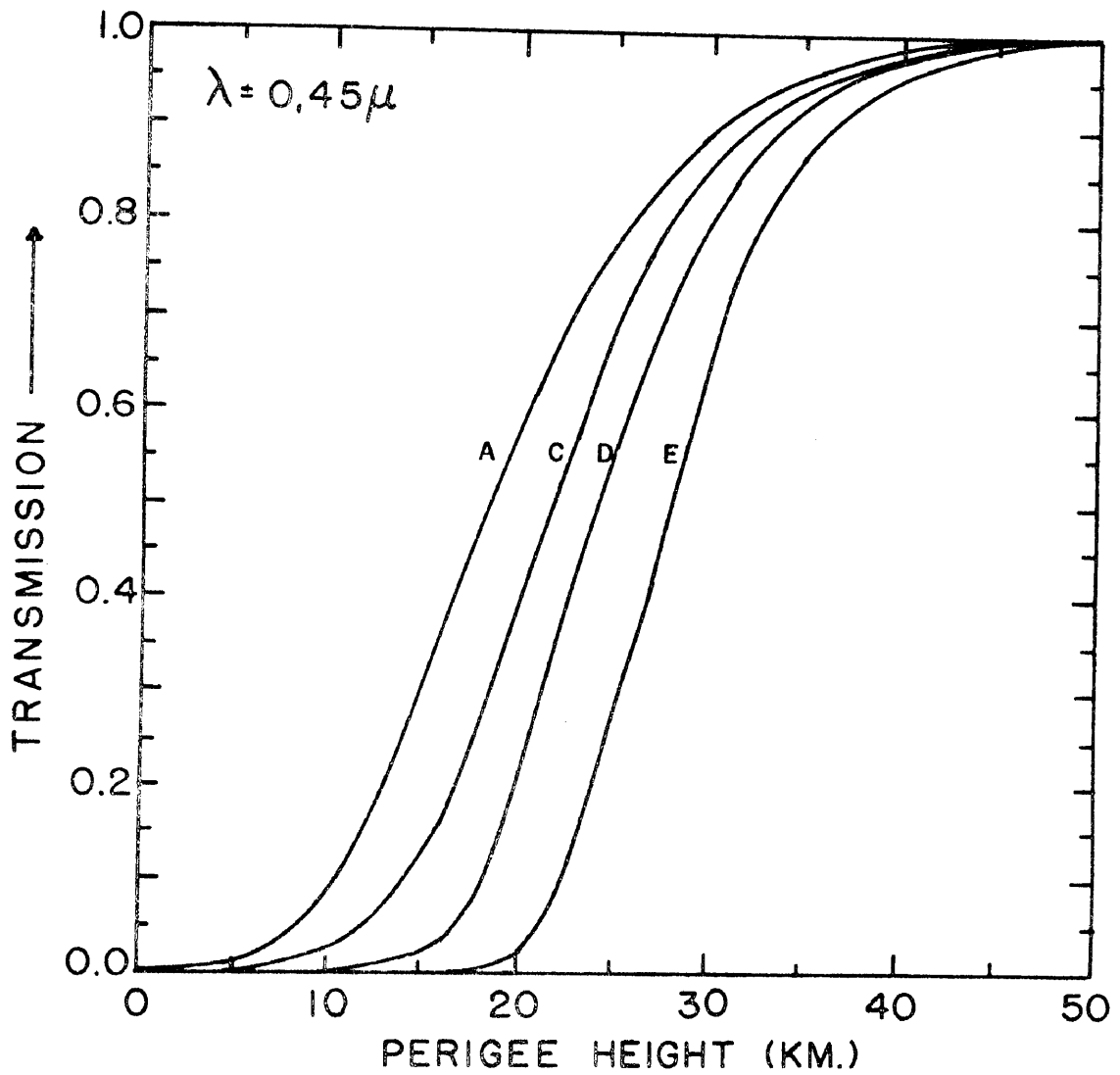


Figure 33 - Transmission from outside atmosphere to perigee point

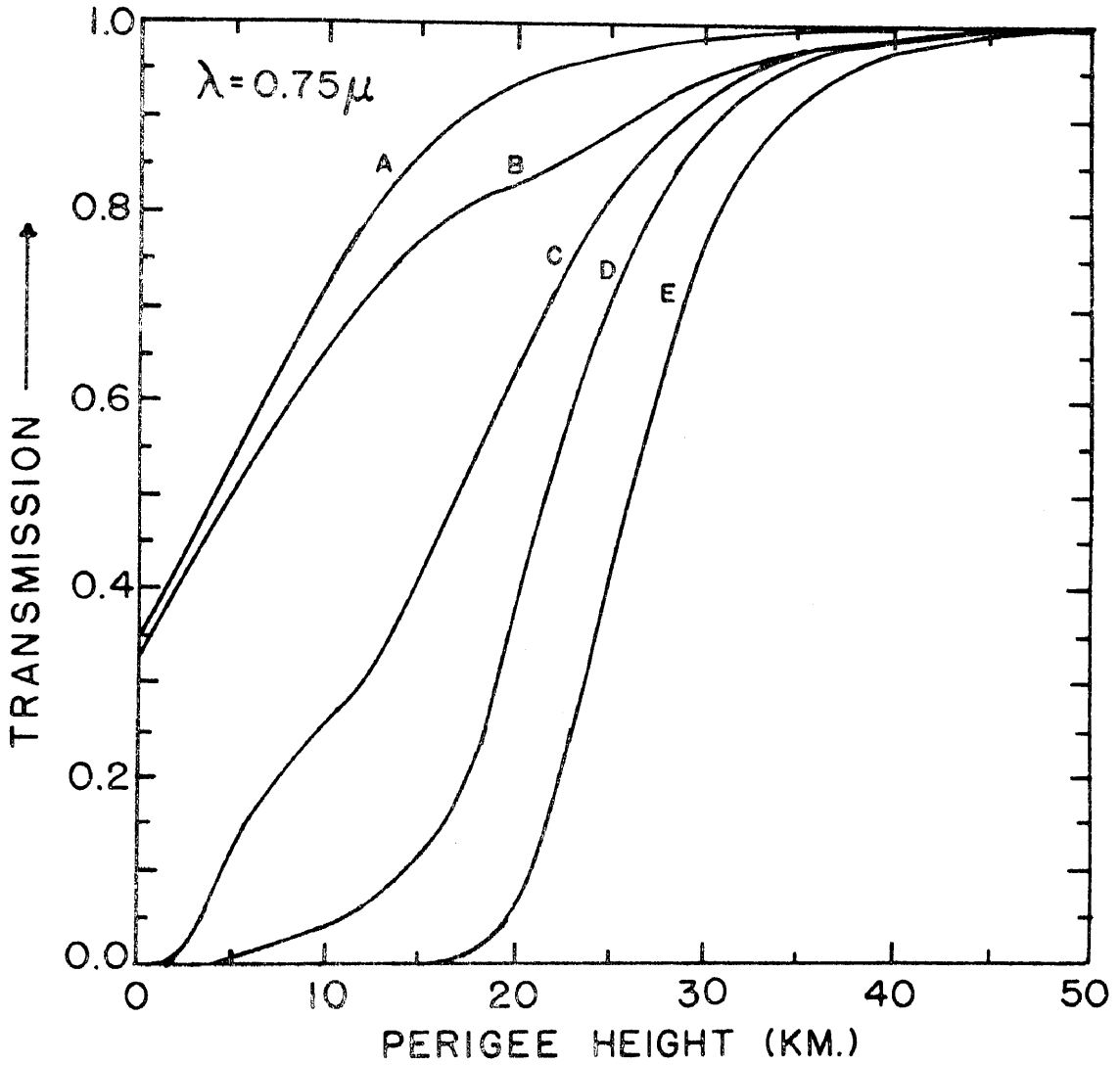


Figure 34 - Same as Figure 33 except $\lambda = 0.75 \mu$

XI. CALCULATED RADIANCE

The single scattered radiance was calculated for the following observer positions: $\Theta_o = 80^\circ, 85^\circ, 90^\circ [2^\circ] 108^\circ$. At each observer position calculations were made for the following zenith viewing angles in the solar plane: $\Theta = 90^\circ, 85^\circ, 80^\circ, 75^\circ, 70^\circ [10^\circ] -70^\circ, -75^\circ, -80^\circ, -85^\circ$, where positive values of Θ refer to viewing angles in the solar direction from the zenith while negative values are in the antisolar direction. All calculations were performed for 8 wavelengths: $0.40 \mu [0.05] 0.75 \mu$.

The radiance calculated for Model A is shown in Figures 35 and 36 as a function of wavelength for $\Theta_o = 90^\circ$ and various viewing angles Θ . All calculated radiance values assume an incident solar flux of unity perpendicular to the incoming solar beam at each wavelength. Later these values are weighted by the solar distribution for the calculation of the colorimetry results. In the solar direction, Figure 35 shows that the greatest change with wavelength occurs when $\Theta = 85^\circ$, the large decrease in the blue caused by the increased Rayleigh scattering at shorter wavelengths. As the viewing angle increases from 85° to zenith, the radiance in the blue increases at first and then decreases. There are three competing effects for a given solar ray as Θ decreases: first, a decrease in radiance due to more absorption of solar

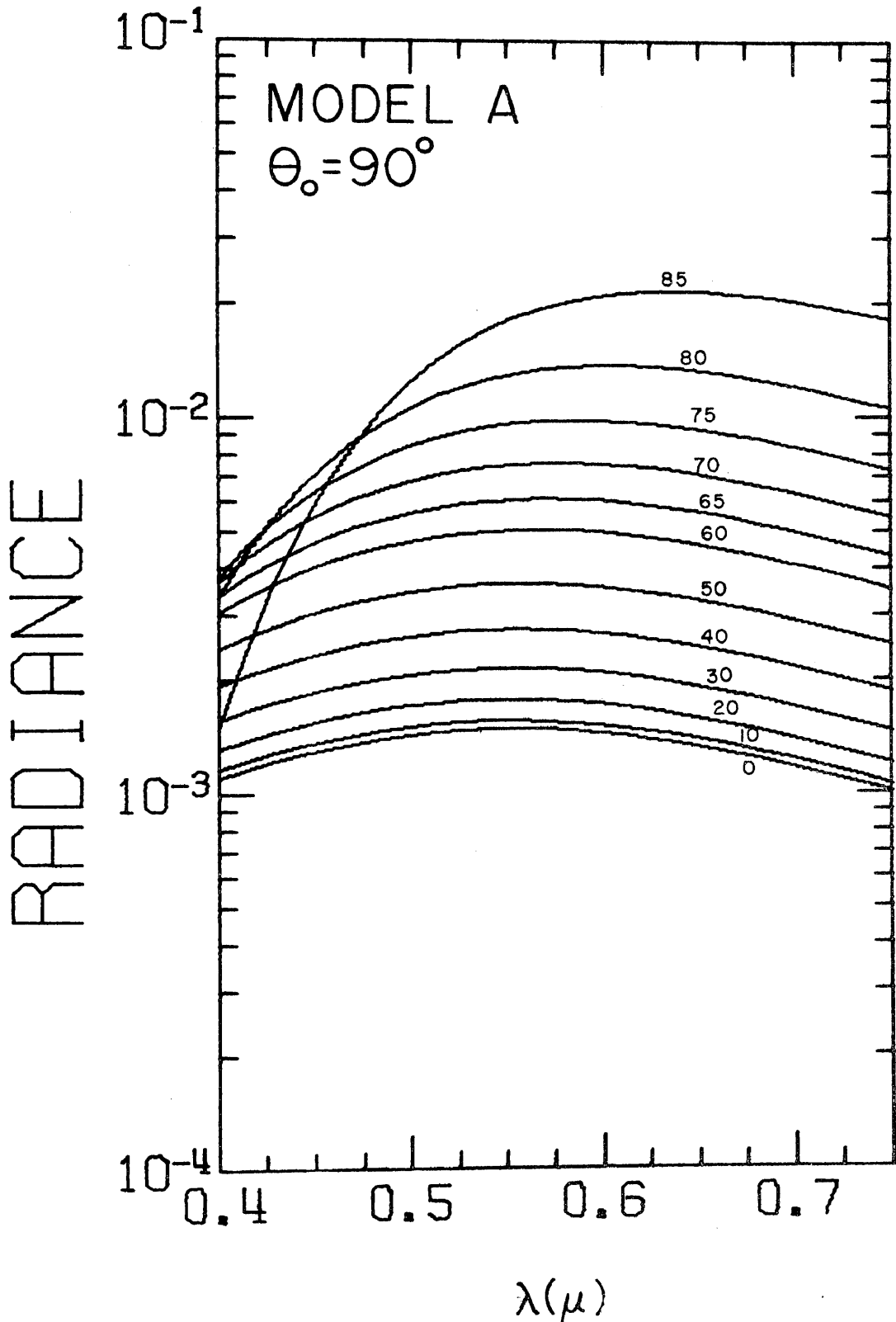


Figure 35 - Radiance as a function of wavelength (microns) for Model A and $\theta_0 = 90^\circ$

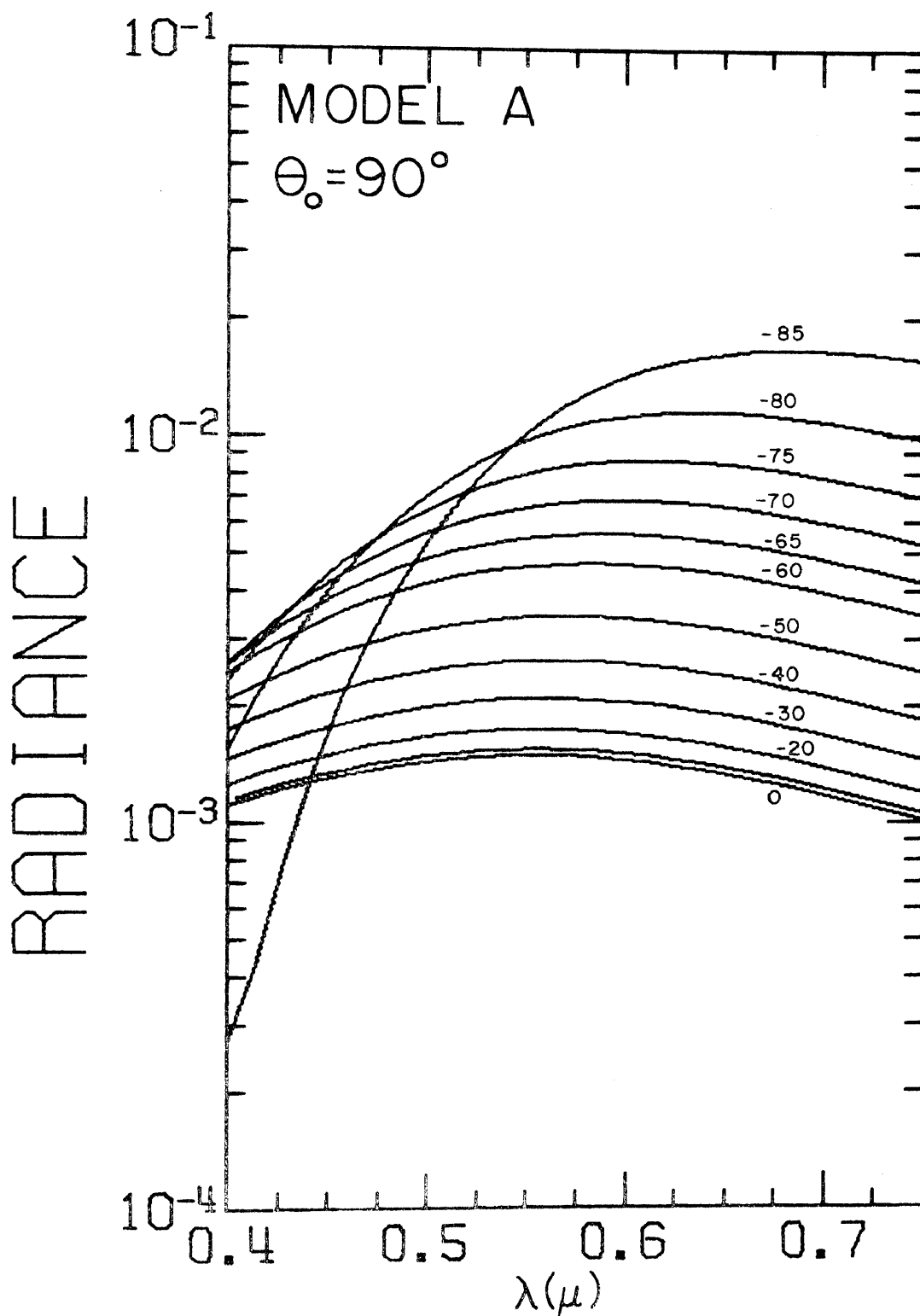


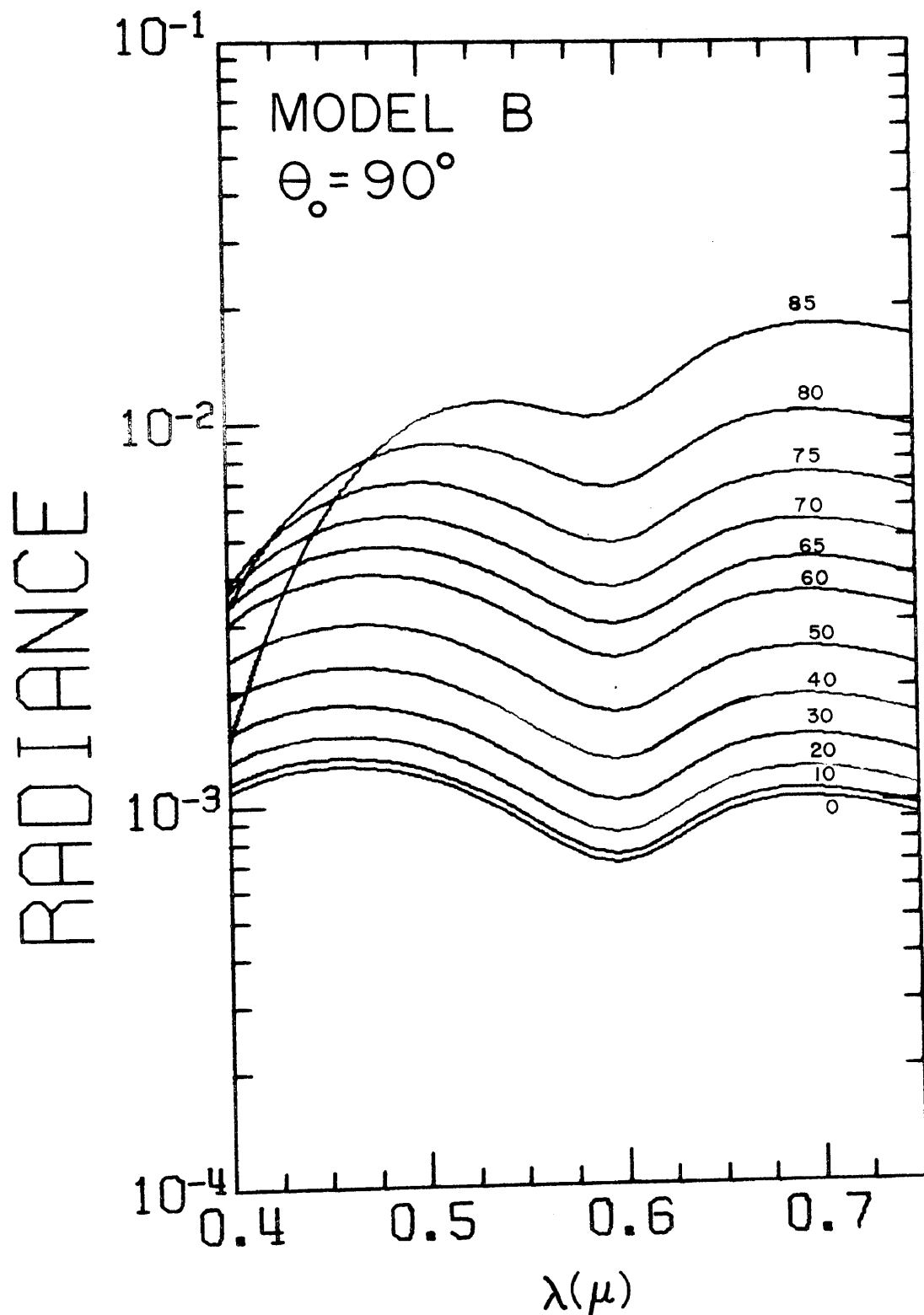
Figure 36 - Radiance as a function of wavelength (microns) for Model A and $\theta_0 = 90^\circ$

radiation along the ray to the scattering center; second, the number of scattering centers along the line of sight decreases by the secant effect; third, the absorption decreases from the scattering center to the observer. The radiance in the antisolar directions is shown in Figure 36.

The radiance in the solar directions for Model B is given in Figure 37 for $\theta_0 = 90^\circ$. The radiance for a fixed value of θ now shows a pronounced minimum near $\lambda = 0.6\mu$ due to the ozone absorption.

The radiance for Model C when $\theta_0 = 90^\circ$ is given in Figure 38 for viewing angles in the solar direction. Rayleigh scattering, ozone absorption, and aerosol scattering are all included in this model. The dip in the radiance curves in the middle of the visible spectrum due to ozone absorption is clearly visible here. In most cases the radiance is less for Model C than for Model A except at long wavelengths and for viewing angles near the horizon. In this case the radiance is larger due to the strong forward scattering of the sunlight by the aerosols and the additional scattering centers along the line of sight.

A more complete understanding of these curves can be obtained by a study of the differential radiance curves shown in Figure 39. The differential radiance per kilometer, dI/ds , (measured along the slant path) is given as a function of the vertical height to the scattering volume measured along the earth's local radius through the infinitesimal volume. Each

Figure 37 - Radiance for Model B and $\theta_0 = 90^\circ$

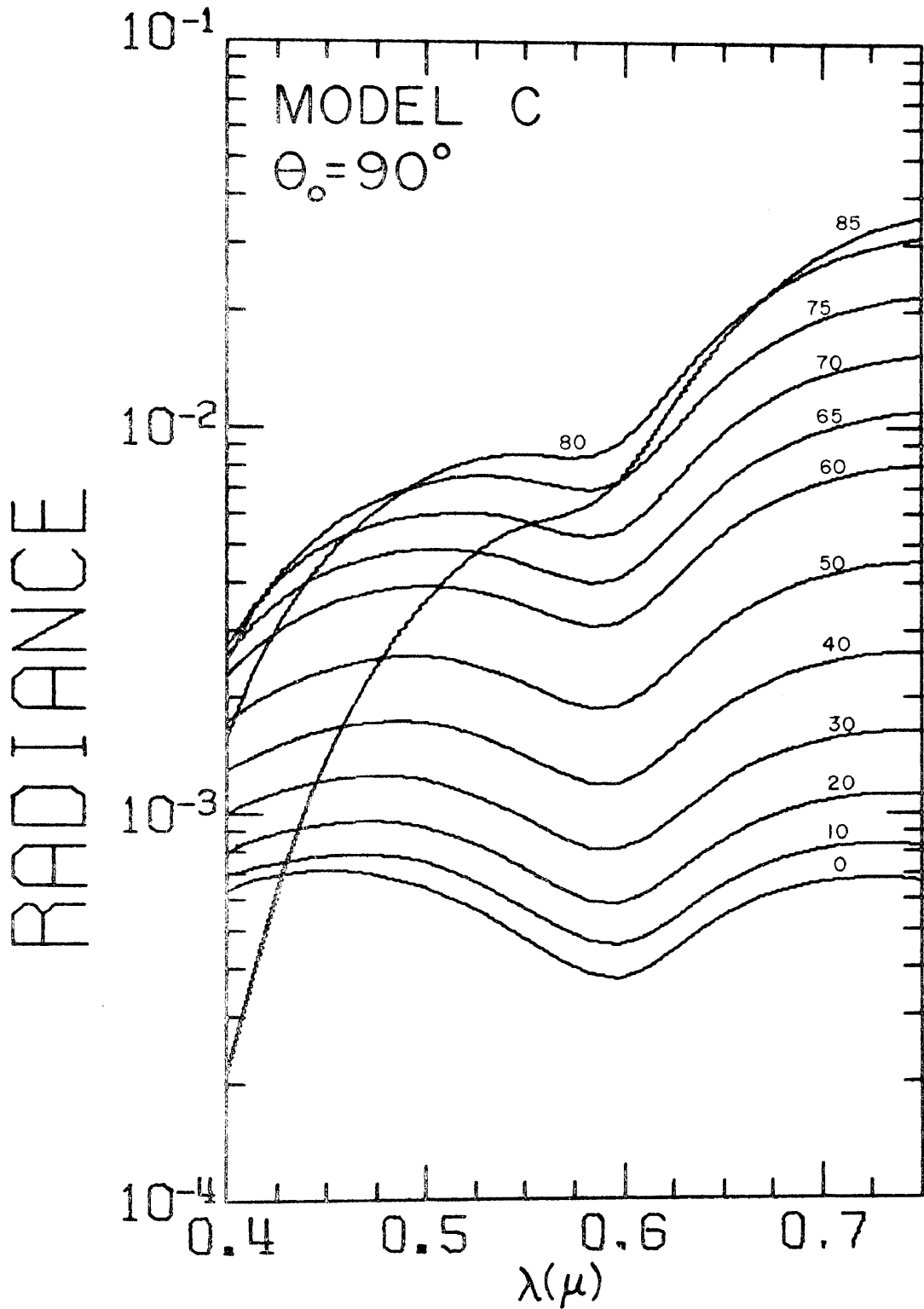


Figure 38 - Radiance for Model C and $\theta_0 = 90^\circ$

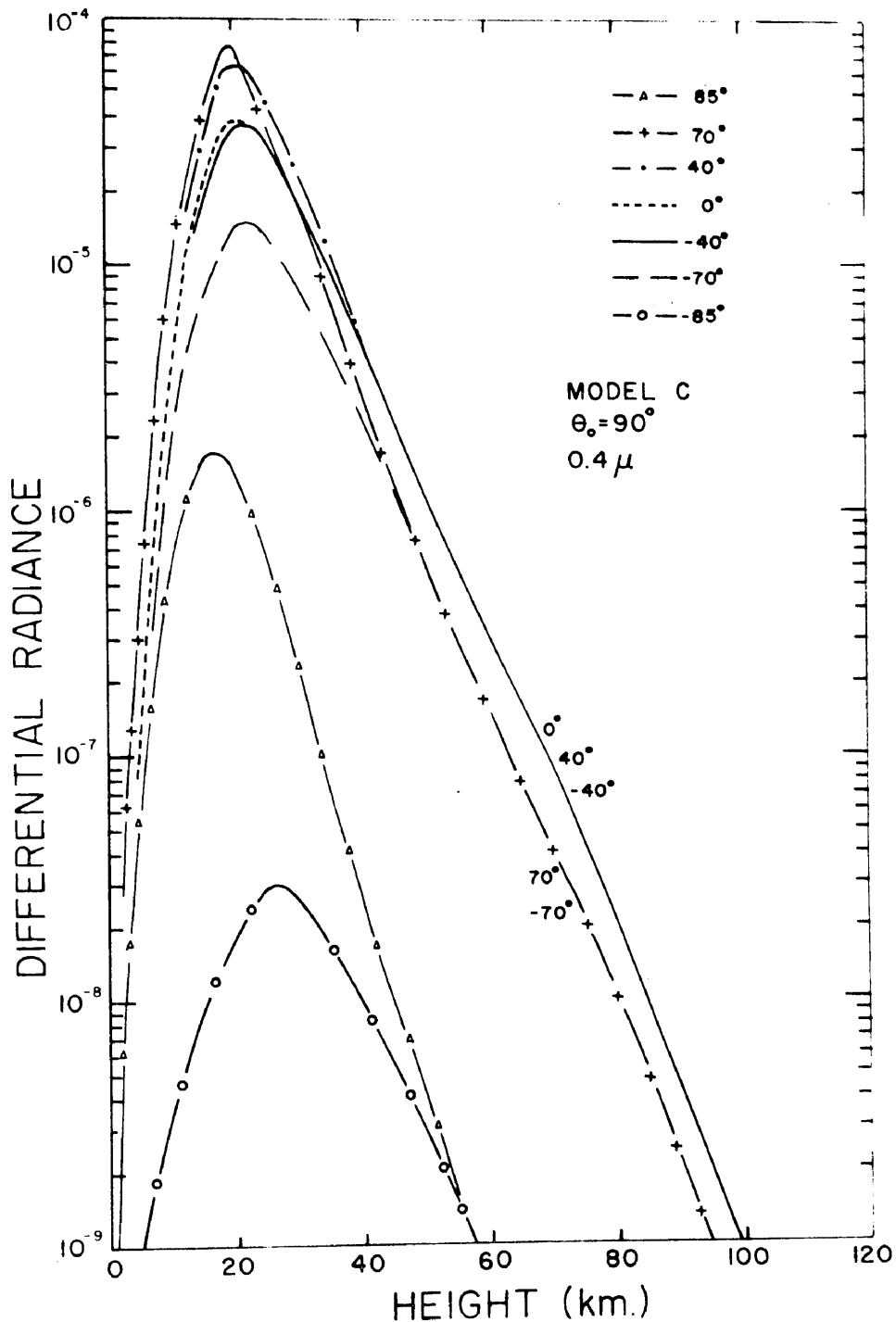


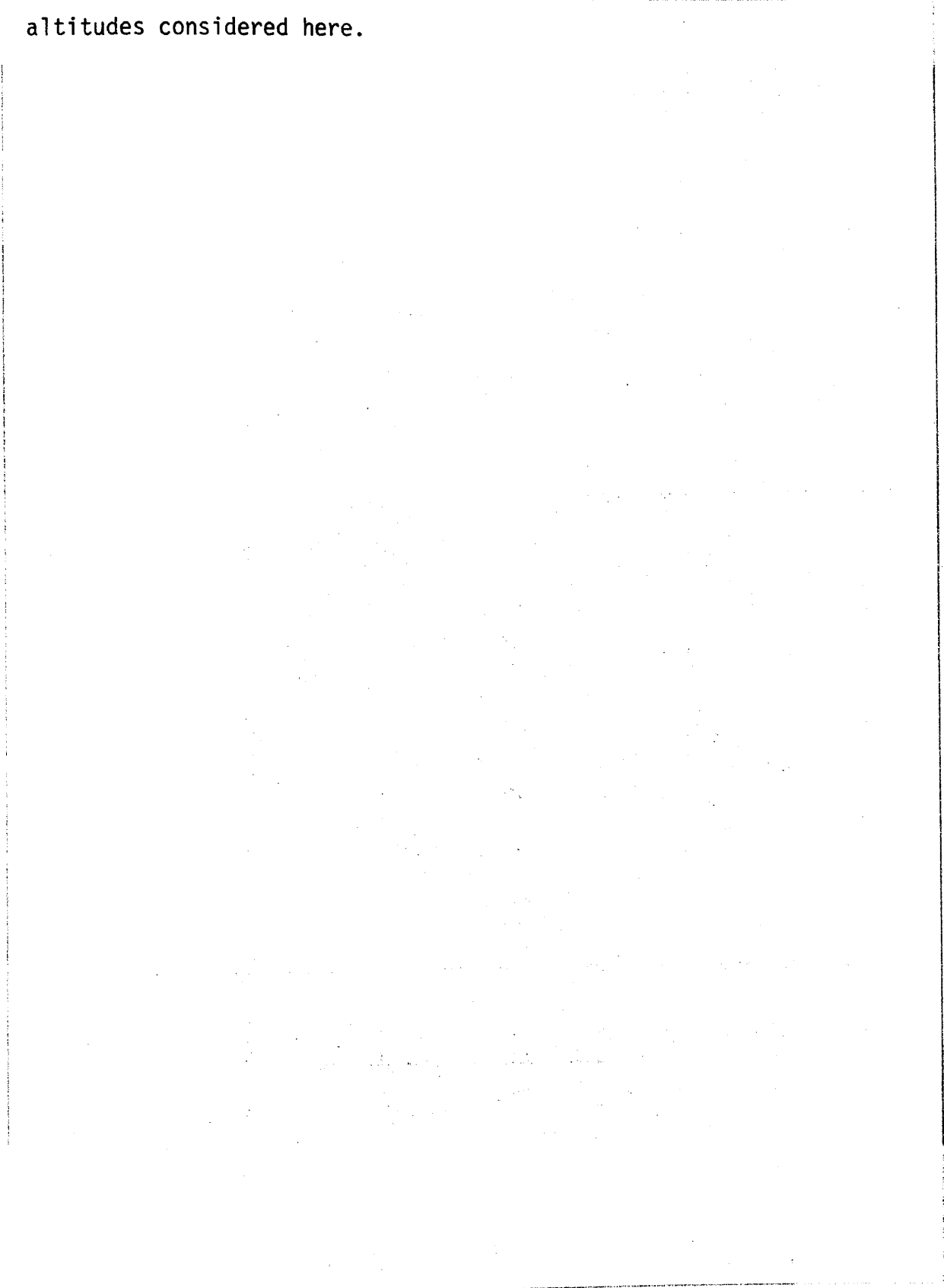
Figure 39 - The differential radiance per kilometer (measured along the slant path) as a function of the vertical height to the scattering volume measured along the earth's local radius through the infinitesimal volume

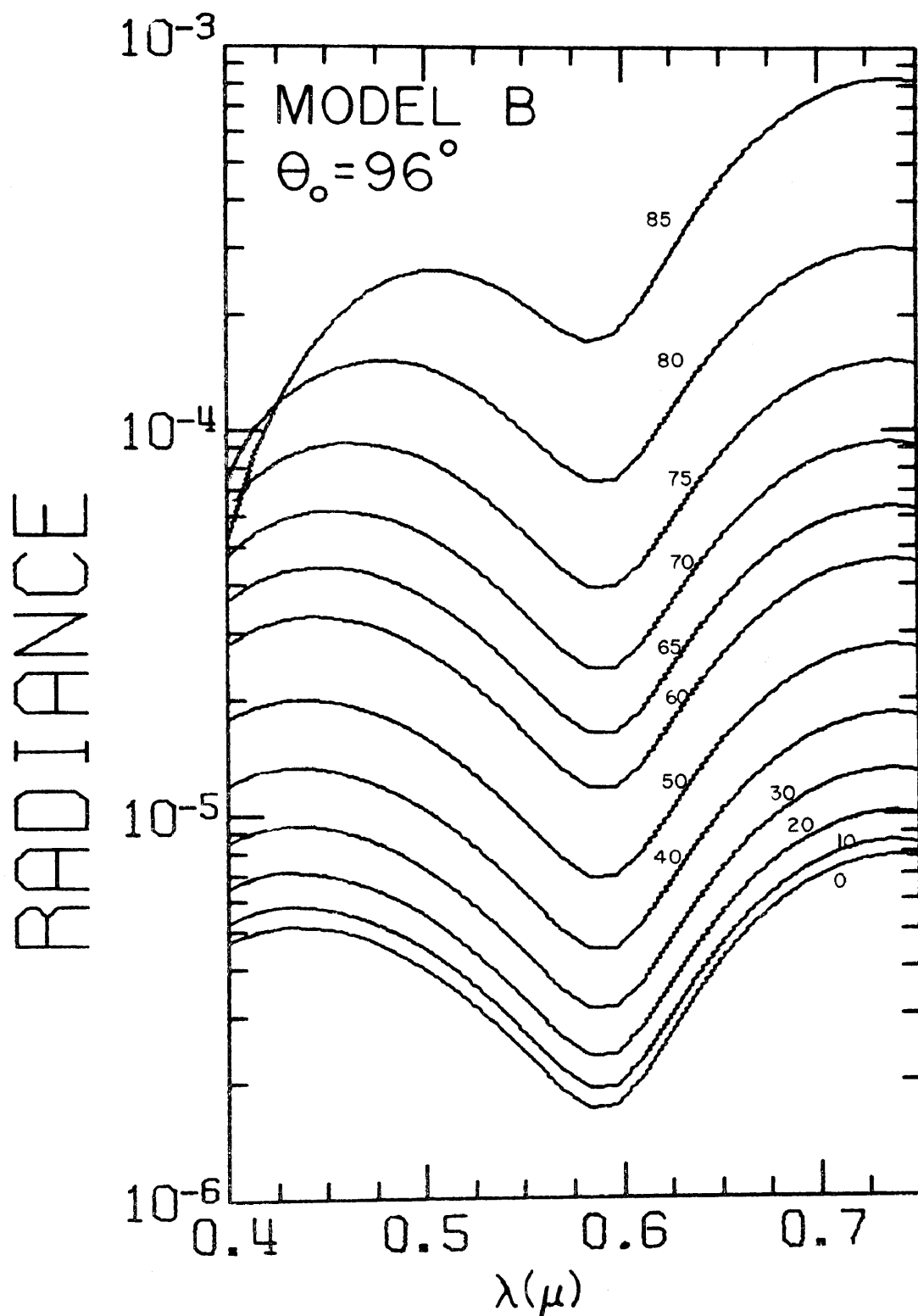
curve for a particular value of θ increases to a maximum value; beyond the maximum it decreases approximately as an exponential. The initial increase in the radiance occurs as the transmission of the solar radiation to the scattering point increases with height. The differential radiance eventually decreases as the number of scattering centers of all types decreases with height. At altitudes above 60 km these curves are identical on the scale of this figure for the same zenith angle in the solar and antisolar directions (e.g. $\theta = 70^\circ$ and $\theta = -70^\circ$). The curves for an observer at $\theta_0 = 90^\circ$ will have this symmetry at altitudes sufficiently high that there is virtually no loss in the solar radiation to the scattering point on either line of sight. At lower altitudes the differential radiance is lower in the antisolar direction because of the additional absorption of the solar beam before it reaches the scattering point (e.g., the curve for $\theta = -85^\circ$ is considerably lower below an altitude of 40 km than that for $\theta = 85^\circ$). Since the radiance observed at a given angle of view is proportional to the area under the corresponding differential radiance curve in Figure 39, the variation in the radiance curves with θ can be understood in terms of the changes in the absorption of the solar beam up to the point of scattering, the dependence of the scattering on the phase function of the aerosols and the Rayleigh scattering centers, the decrease of the scattering centers along the line of sight.

The radiance for Model B and $\Theta_0 = 96^\circ$ is shown in Figure 40. The radiance for Model C and $\Theta_0 = 96^\circ$ is given in Figures 41 and 42 for the solar and antisolar directions respectively. In general the difference in radiance values for large observation angles from the zenith between Models B and C is greatest at short than at long wavelengths. This is largely due to the very small values of the transmission from the scattering point to the observer for Model C at $\lambda = 0.4\mu$ which reduces the observed radiance by more than an order of magnitude. The corresponding transmission for Model C at $\lambda = 0.75\mu$ is much larger. The radiance in the anti-solar direction shows little dependence on Θ until $\Theta = -40^\circ$. The radiance rapidly decreases to very small values for larger zenith angles in the antisolar direction.

The differential radiance for $\Theta_0 = 96^\circ$ is given in Figure 43. The differential radiance at the zenith reaches a maximum at about 62 km. The maxima for $\Theta = 40^\circ$ and $\Theta = -40^\circ$ occur approximately at 57 and 67 km respectively. The curves for $\Theta = 0^\circ$, 40° , and -40° are nearly the same on the scale of the figure above 75 km. Below 90 km the differential radiance for $\Theta = -70^\circ$ is very much less than that for $\Theta = 70^\circ$ due to the much greater atmospheric path that the solar rays must traverse to reach the scattering point in the former case and the additional divergence of the beam. The maxima for these two angles are at about 50 and 82 km respectively. The maximum for $\Theta = 85^\circ$ is at about 35 km. No single scattered radiation can be observed at $\Theta = -85^\circ$ up to the

altitudes considered here.



Figure 40 - Radiance for Model B and $\theta_0 = 96^\circ$

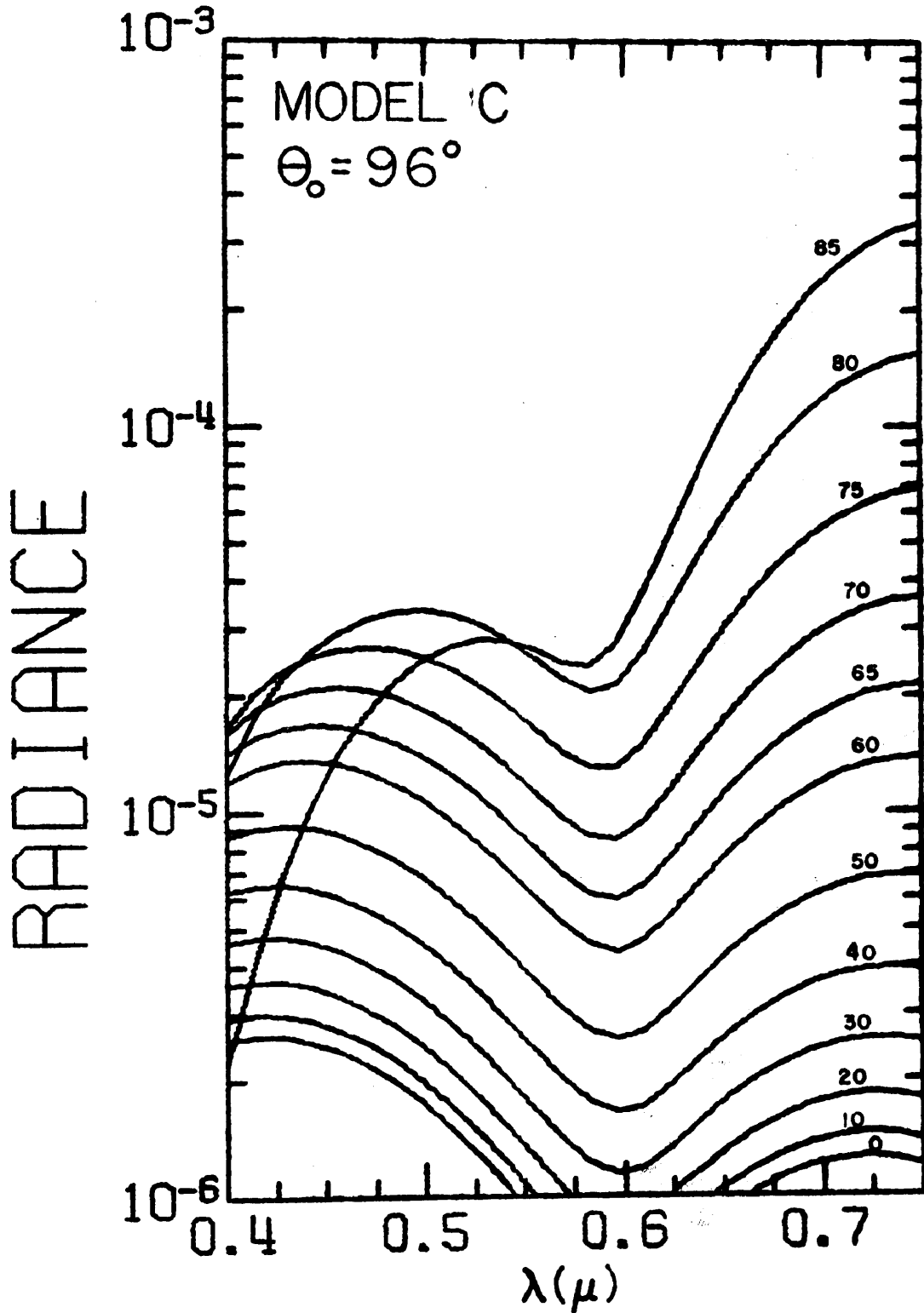


Figure 41 - Radiance for Model C and $\theta_0 = 96^\circ$ for solar half plane

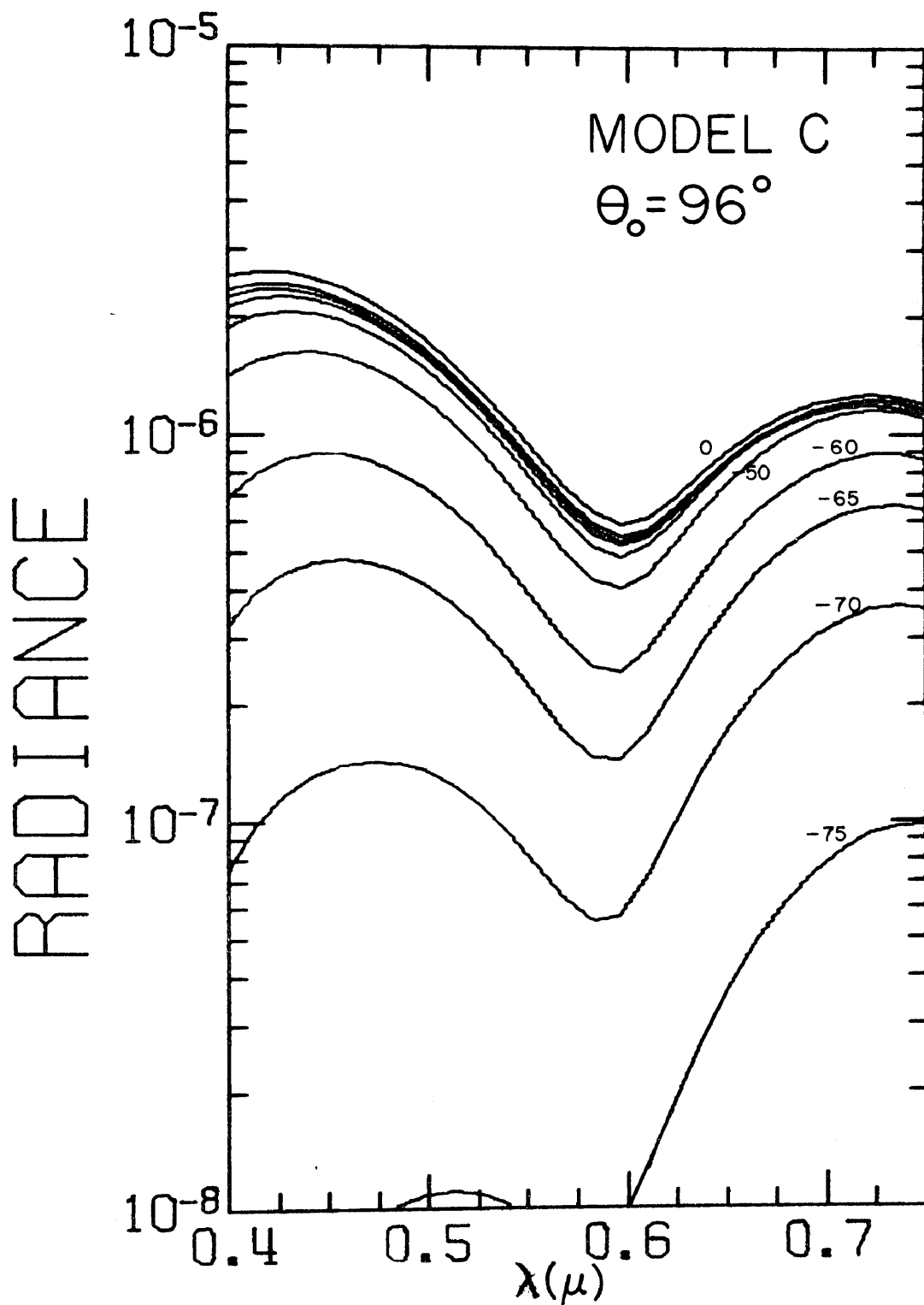


Figure 42 - Radiance for Model C and $\theta_0 = 96^\circ$ for antisolar half plane

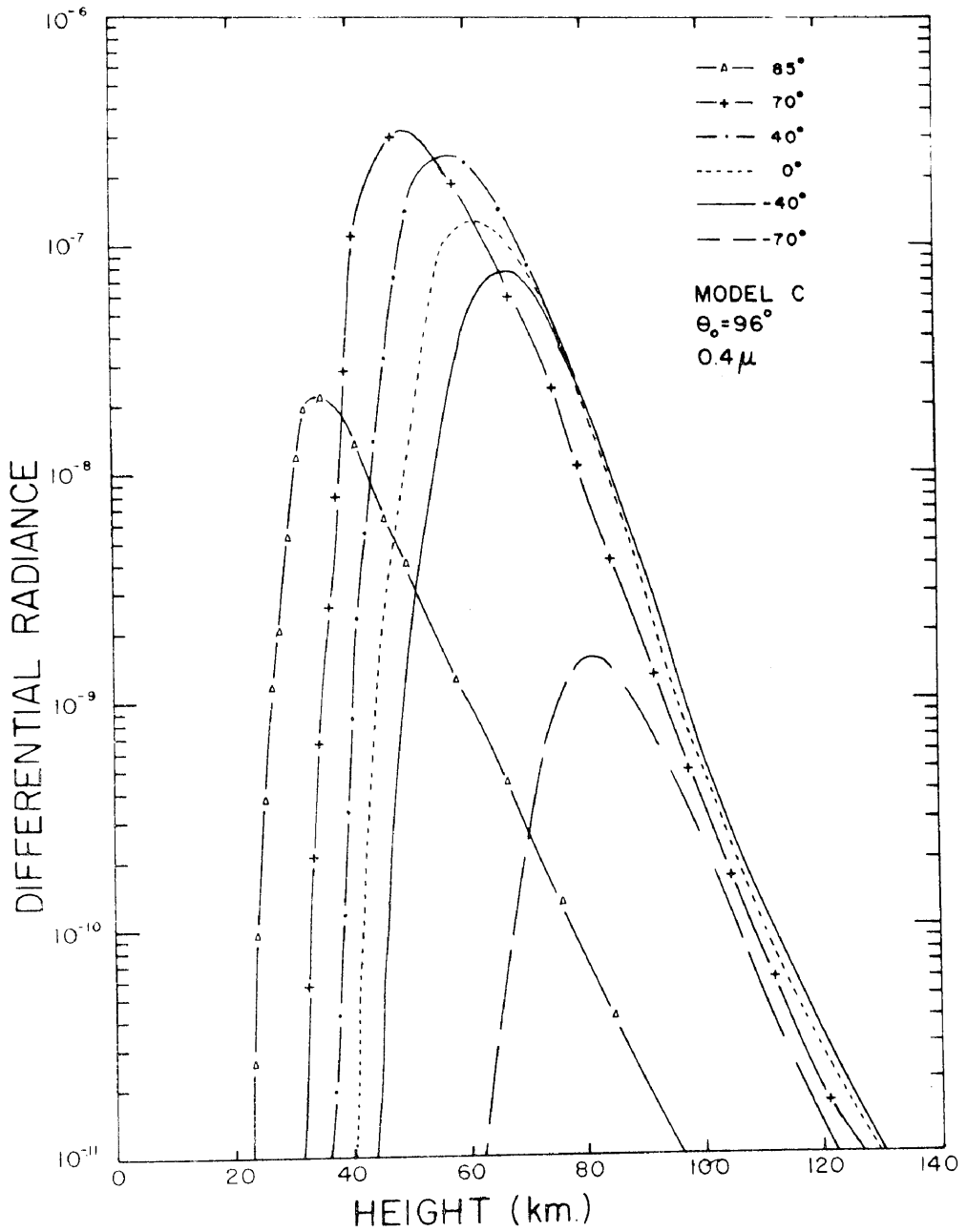


Figure 43 - Differential radiance for Model C, $\theta_0 = 96^\circ$, and $\lambda = 0.4 \mu$

XII. CHROMATICITY

The chromaticity was calculated for each model and solar zenith angle by the method described in Chapter IX. The results are shown in a series of chromaticity diagrams in which the x and y chromaticity coordinates are plotted for each viewing angle in the solar and antisolar half planes. For further reference the chromaticity coordinates are given in Tables II to VI for each of the five models, for various values of θ , and for $\theta_0 = 90^\circ$, 92° , 94° , and 96° .

a) Model A. Molecular atmosphere without ozone.

The chromaticity diagrams for Model A are shown in Figures 44 and 45 for $\theta_0 = 90^\circ$, 92° , and 96° . The regions traditionally assigned to the different colors are indicated in Figure 44 for guidance. The spectral purity isopleths are indicated in all the figures. When the spectral purity is less than about 5% the color is usually assumed to be a white or gray without discernable color. The numbers beside the curve indicate the zenith angle of observation (positive for the solar half plane and negative for the antisolar half plane). The colors for $\theta_0 = 90^\circ$ are all yellow or an essentially white color near the zenith. At $\theta_0 = 92^\circ$ and 96° the colors near the horizon have slightly greater spectral purity.

TABLE II. COLORIMETRY VALUES FOR MODEL A

θ_0	θ	X	Y	θ_0	θ	X	Y
90	90	—	—	94	90	0.5683	0.4165
90	85	0.4025	0.4193	94	85	0.4215	0.4168
90	80	0.3612	0.3860	94	80	0.3750	0.3832
90	75	0.3446	0.3693	94	75	0.3588	0.3672
90	70	0.3360	0.3600	94	70	0.3517	0.3587
90	60	0.3276	0.3505	94	60	0.3461	0.3514
90	40	0.3216	0.3431	94	40	0.3427	0.3462
90	20	0.3200	0.3411	94	20	0.3456	0.3472
90	0	0.3200	0.3409	94	0	0.3483	0.3489
90	-20	0.3217	0.3429	94	-20	0.3505	0.3517
90	-40	0.3258	0.3472	94	-40	0.3603	0.3562
90	-60	0.3362	0.3582	94	-60	0.3794	0.3699
90	-70	0.3494	0.3712	94	-70	0.4075	0.3864
90	-75	0.3630	0.3837	94	-75	0.4393	0.3997
90	-80	0.3900	0.4054	94	-80	0.5117	0.4124
92	90	0.5582	0.4241	96	90	0.5702	0.4147
92	85	0.4226	0.4202	96	85	0.4163	0.4143
92	80	0.3796	0.3899	96	80	0.3663	0.3772
92	75	0.3612	0.3722	96	75	0.3484	0.3589
92	70	0.3538	0.3654	96	70	0.3408	0.3499
92	60	0.3488	0.3576	96	60	0.3340	0.3413
92	40	0.3389	0.3484	96	40	0.3317	0.3367
92	20	0.3428	0.3511	96	20	0.3330	0.3363
92	0	0.3412	0.3490	96	0	0.3355	0.3379
92	-20	0.3449	0.3524	96	-20	0.3415	0.3426
92	-40	0.3516	0.3578	96	-40	0.3533	0.3519
92	-60	0.3680	0.3703	96	-60	0.3861	0.3746
92	-70	0.3881	0.3852	96	-70	0.4453	0.4033
92	-75	0.4082	0.3978	96	-75	0.5193	0.4155
92	-80	0.4492	0.4147	96	-80	0.6161	0.3786

TABLE III. COLORIMETRY VALUES FOR MODEL B

θ_0	θ	X	Y	θ_0	θ	X	Y
90	90			94	90	0.5616	0.4137
90	85	0.3597	0.3928	94	85	0.3543	0.3693
90	80	0.3142	0.3471	94	80	0.2992	0.3138
90	75	0.2970	0.3261	94	75	0.2825	0.2921
90	70	0.2885	0.3150	94	70	0.2757	0.2812
90	60	0.2803	0.3035	94	60	0.2701	0.2719
90	40	0.2744	0.2949	94	40	0.2661	0.2642
90	20	0.2726	0.2921	94	20	0.2681	0.2647
90	0	0.2726	0.2921	94	0	0.2698	0.2656
90	-20	0.2737	0.2934	94	-20	0.2714	0.2677
90	-40	0.2769	0.2975	94	-40	0.2784	0.2721
90	-60	0.2860	0.3091	94	-60	0.2949	0.2863
90	-70	0.2979	0.3236	94	-70	0.3219	0.3066
90	-75	0.3104	0.3375	94	-75	0.3588	0.3284
90	-80	0.3377	0.3648	94	-80	0.4648	0.3698
92	90	0.5496	0.4238	96	90	0.5631	0.4094
92	85	0.3710	0.3874	96	85	0.3298	0.3513
92	80	0.3203	0.3400	96	80	0.2771	0.2960
92	75	0.3012	0.3167	96	75	0.2619	0.2744
92	70	0.2927	0.3064	96	70	0.2555	0.2641
92	60	0.2886	0.2980	96	60	0.2498	0.2539
92	40	0.2776	0.2845	96	40	0.2469	0.2469
92	20	0.2782	0.2846	96	20	0.2470	0.2456
92	0	0.2795	0.2848	96	0	0.2480	0.2455
92	-20	0.2822	0.2872	96	-20	0.2513	0.2486
92	-40	0.2884	0.2934	96	-40	0.2588	0.2558
92	-60	0.3037	0.3074	96	-60	0.2847	0.2791
92	-70	0.3238	0.3255	96	-70	0.3515	0.3281
92	-75	0.3457	0.3425	96	-75	0.4657	0.3807
92	-80	0.3963	0.3708	96	-80	0.6247	0.3644

TABLE IV. COLORIMETRY VALUES FOR MODEL C

θ_0	θ	X	Y	θ_0	θ	X	Y
90	90	—	—	94	90	0.6728	0.3254
90	85	0.4644	0.4134	94	85	0.4530	0.3986
90	80	0.3896	0.3829	94	80	0.3693	0.3538
90	75	0.3572	0.3601	94	75	0.3313	0.3239
90	70	0.3395	0.3452	94	70	0.3100	0.3056
90	60	0.3205	0.3307	94	60	0.2850	0.2833
90	40	0.2996	0.3146	94	40	0.2565	0.2573
90	20	0.2850	0.3015	94	20	0.2446	0.2456
90	0	0.2731	0.2861	94	0	0.2365	0.2367
90	-20	0.2666	0.2796	94	-20	0.2328	0.2347
90	-40	0.2671	0.2824	94	-40	0.2344	0.2377
90	-60	0.2779	0.2968	94	-60	0.2427	0.2500
90	-70	0.2956	0.3166	94	-70	0.2574	0.2672
90	-75	0.3137	0.3350	94	-75	0.2766	0.2860
90	-80	0.3515	0.3666	94	-80	0.3519	0.3366
92	90	0.6690	0.3292	96	90	0.6773	0.3209
92	85	0.4577	0.4082	96	85	0.4246	0.3864
92	80	0.3830	0.3725	96	80	0.3189	0.3263
92	75	0.3500	0.3486	96	75	0.2782	0.2903
92	70	0.3315	0.3330	96	70	0.2587	0.2697
92	60	0.3135	0.3180	96	60	0.2408	0.2489
92	40	0.2866	0.2951	96	40	0.2280	0.2322
92	20	0.2743	0.2827	96	20	0.2235	0.2260
92	0	0.2592	0.2640	96	0	0.2215	0.2236
92	-20	0.2537	0.2583	96	-20	0.2215	0.2239
92	-40	0.2553	0.2622	96	-40	0.2236	0.2279
92	-60	0.2673	0.2765	96	-60	0.2333	0.2423
92	-70	0.2881	0.2972	96	-70	0.2691	0.2805
92	-75	0.3100	0.3164	96	-75	0.3679	0.3503
92	-80	0.3605	0.3486	96	-80	0.4739	0.3404

TABLE V. COLORIMETERY VALUES FOR MODEL D

θ_0	θ	X	Y	θ_0	θ	X	Y
90	90	————	————	94	90	0.7032	0.2961
90	85	0.5285	0.4080	94	85	0.5121	0.4033
90	80	0.4296	0.3978	94	80	0.3957	0.3769
90	75	0.3835	0.3754	94	75	0.3416	0.3441
90	70	0.3589	0.3584	94	70	0.3138	0.3224
90	60	0.3342	0.3423	94	60	0.2824	0.2952
90	40	0.3112	0.3264	94	40	0.2529	0.2646
90	20	0.2955	0.3128	94	20	0.2401	0.2498
90	0	0.2796	0.2901	94	0	0.2325	0.2387
90	-20	0.2689	0.2780	94	-20	0.2301	0.2362
90	-40	0.2678	0.2797	94	-40	0.2323	0.2415
90	-60	0.2825	0.2998	94	-60	0.2420	0.2575
90	-70	0.3081	0.3259	94	-70	0.2559	0.2783
90	-75	0.3336	0.3481	94	-75	0.2701	0.2967
90	-80	0.3843	0.3800	94	-80	0.3098	0.3321
92	90	0.7030	0.2963	96	90	0.7026	0.2966
92	85	0.5237	0.4051	96	85	0.4991	0.4027
92	80	0.4187	0.3882	96	80	0.3664	0.3660
92	75	0.3676	0.3620	96	75	0.3074	0.3242
92	70	0.3419	0.3432	96	70	0.2781	0.2969
92	60	0.3144	0.3236	96	60	0.2518	0.2674
92	40	0.2870	0.3013	96	40	0.2339	0.2437
92	20	0.2696	0.2838	96	20	0.2278	0.2347
92	0	0.2540	0.2616	96	0	0.2252	0.2310
92	-20	0.2457	0.2521	96	-20	0.2250	0.2313
92	-40	0.2456	0.2551	96	-40	0.2268	0.2354
92	-60	0.2569	0.2720	96	-60	0.2340	0.2491
92	-70	0.2770	0.2961	96	-70	0.2502	0.2720
92	-75	0.2967	0.3165	96	-75	0.2858	0.3053
92	-80	0.3381	0.3490	96	-80	0.3180	0.3464

TABLE VI. COLORIMETERY VALUES FOR MODEL E

θ_0	θ	X	Y	θ_0	θ	X	Y
90	85	0.6588	0.3368	94	85	0.6590	0.3360
90	80	0.5578	0.3959	94	80	0.5525	0.3939
90	75	0.4885	0.4050	94	75	0.4749	0.3998
90	70	0.4446	0.3971	94	70	0.4246	0.3889
90	60	0.3961	0.3814	94	60	0.3661	0.3640
90	40	0.3561	0.3632	94	40	0.3104	0.3258
90	20	0.3365	0.3514	94	20	0.2843	0.3019
90	0	0.3198	0.3288	94	0	0.2697	0.2848
90	-20	0.3095	0.3172	94	-20	0.2660	0.2821
90	-40	0.3136	0.3247	94	-40	0.2739	0.2936
90	-60	0.3479	0.3570	94	-60	0.3047	0.3273
90	-70	0.4032	0.3892	94	-70	0.3490	0.3637
90	-75	0.4521	0.4045	94	-75	0.3945	0.3888
90	-80	0.5287	0.4036	94	-80	0.4857	0.4024
92	85	0.6589	0.3364	96	85	0.6582	0.3364
92	80	0.5570	0.3934	96	80	0.5406	0.3976
92	75	0.4829	0.4020	96	75	0.4493	0.3983
92	70	0.4372	0.3927	96	70	0.3879	0.3783
92	60	0.3859	0.3753	96	60	0.3228	0.3387
92	40	0.3415	0.3518	96	40	0.2760	0.2958
92	20	0.3177	0.3350	96	20	0.2613	0.2793
92	0	0.2996	0.3108	96	0	0.2563	0.2731
92	-20	0.2882	0.2995	96	-20	0.2577	0.2755
92	-40	0.2931	0.3084	96	-40	0.2668	0.2877
92	-60	0.3257	0.3411	96	-60	0.2963	0.3203
92	-70	0.3762	0.3759	96	-70	0.3422	0.3561
92	-75	0.4230	0.3963	96	-75	0.3967	0.3895
92	-80	0.5012	0.4059	96	-80	0.4856	0.4129

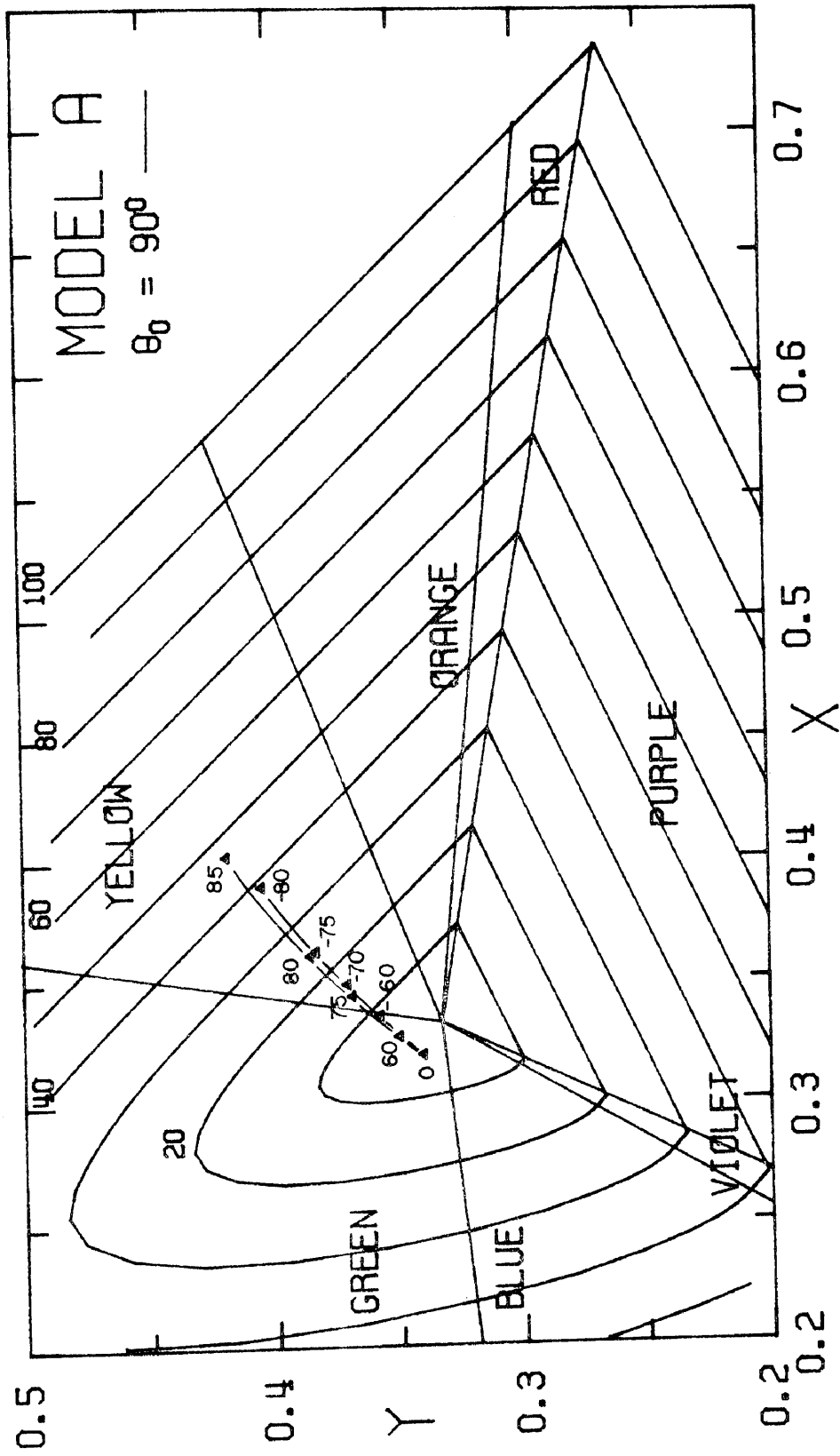


Figure 44 - Chromaticity diagram for Model A and $\theta_0=90^\circ$

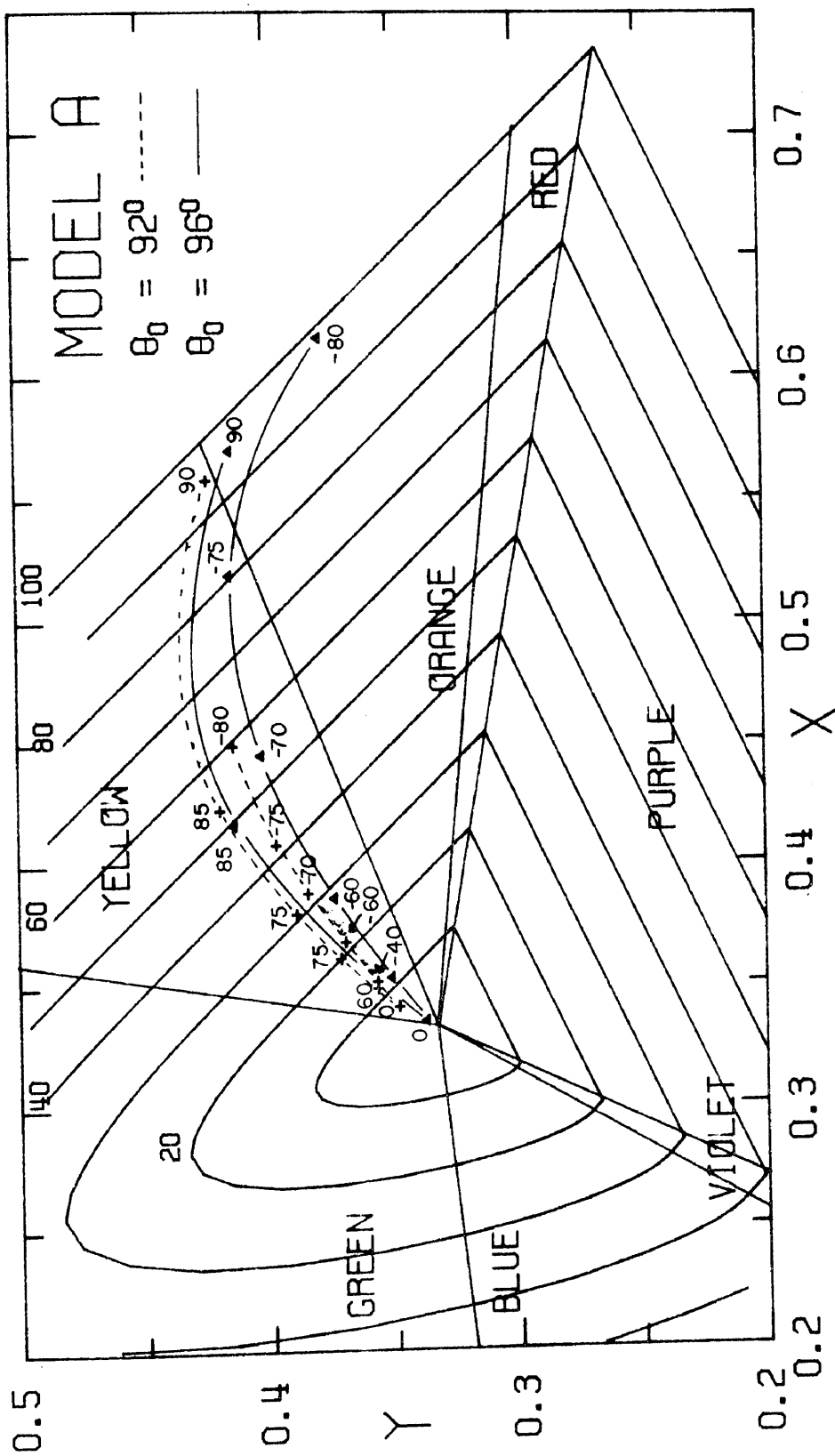


Figure 45 - Chromaticity diagram for Model A and $\theta_0 = 92^\circ$ and 96°

A portion of these latter curves is also in the orange portion of the spectrum. The zenith sky is not blue in this model. The actual colors of the twilight sky are not well represented by this model, except for the predominately yellow-orange color just above the solar horizon.

For comparison, results were obtained in some cases both with and without consideration of the effects of refraction in the atmosphere. For example, at $\Theta_0 = 96^\circ$ and $\Theta = 0^\circ$, $x = 0.336$ and $y = 0.327$ when refractive effects are taken into account, but $x = 0.316$ and $y = 0.327$ without refraction. In all cases calculated the x and y values were less without refraction than the same values obtained with refraction. Thus values calculated without refraction tend to be too far down on the chromaticity diagram and in many cases would show blue or purple colors that do not exist when refraction effects are included. This may explain some of the differences between these results and those of Dave and Mateer (1968). Other differences include the use of somewhat different atmospheric models and the extension of the atmosphere to much higher altitudes (500 km) in the present calculations.

b) Model B. Molecular atmosphere with ozone.

The results when 0.35 cm of ozone are added to the molecular atmosphere are shown in Figures 46 and 47. The main change brought about by the addition of the ozone to the model is the development of blue color over a large area of the sky surrounding the zenith.

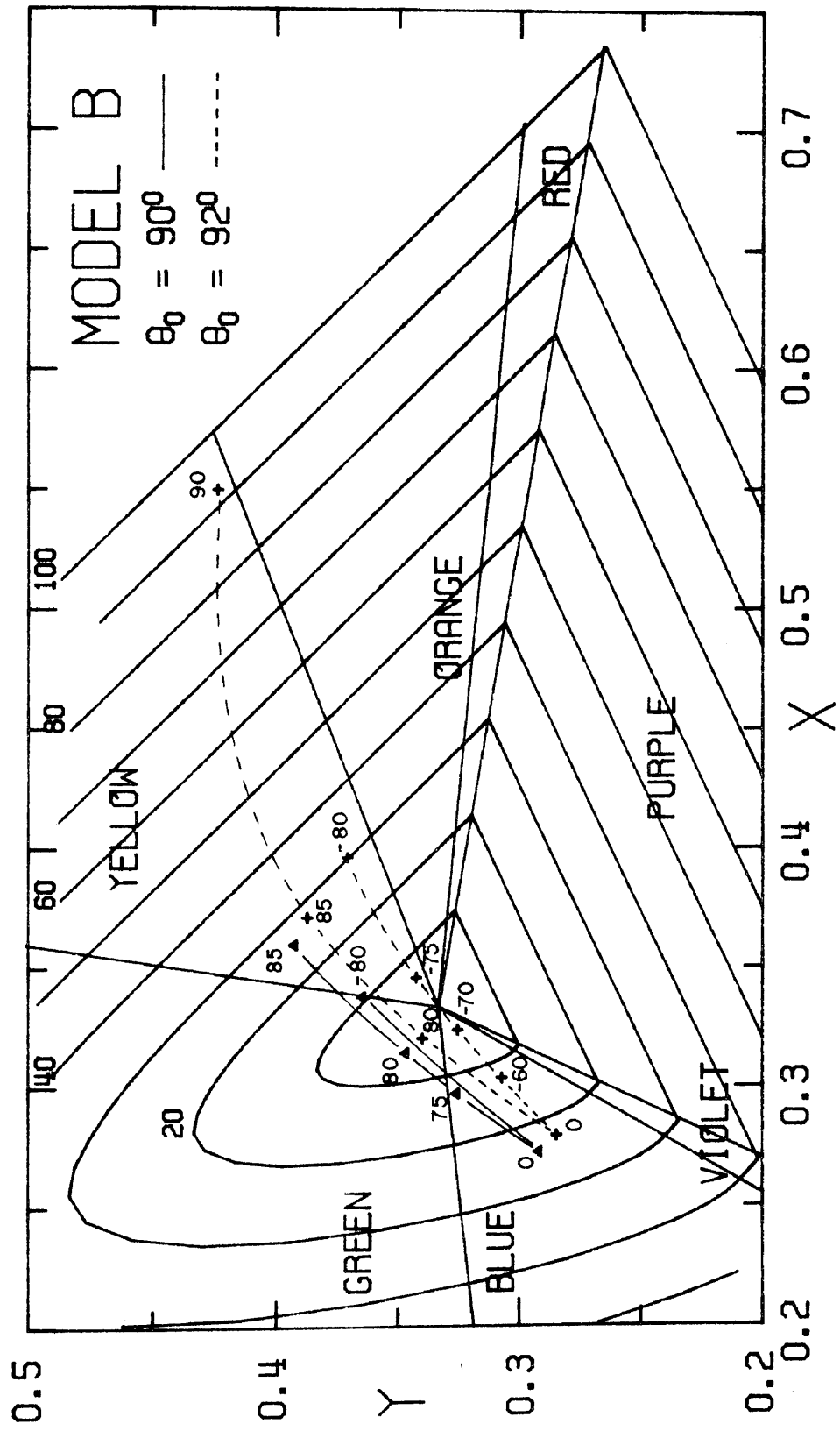


Figure 46 - Chromaticity diagram for Model B and $\theta_0=90^\circ$ and 92°

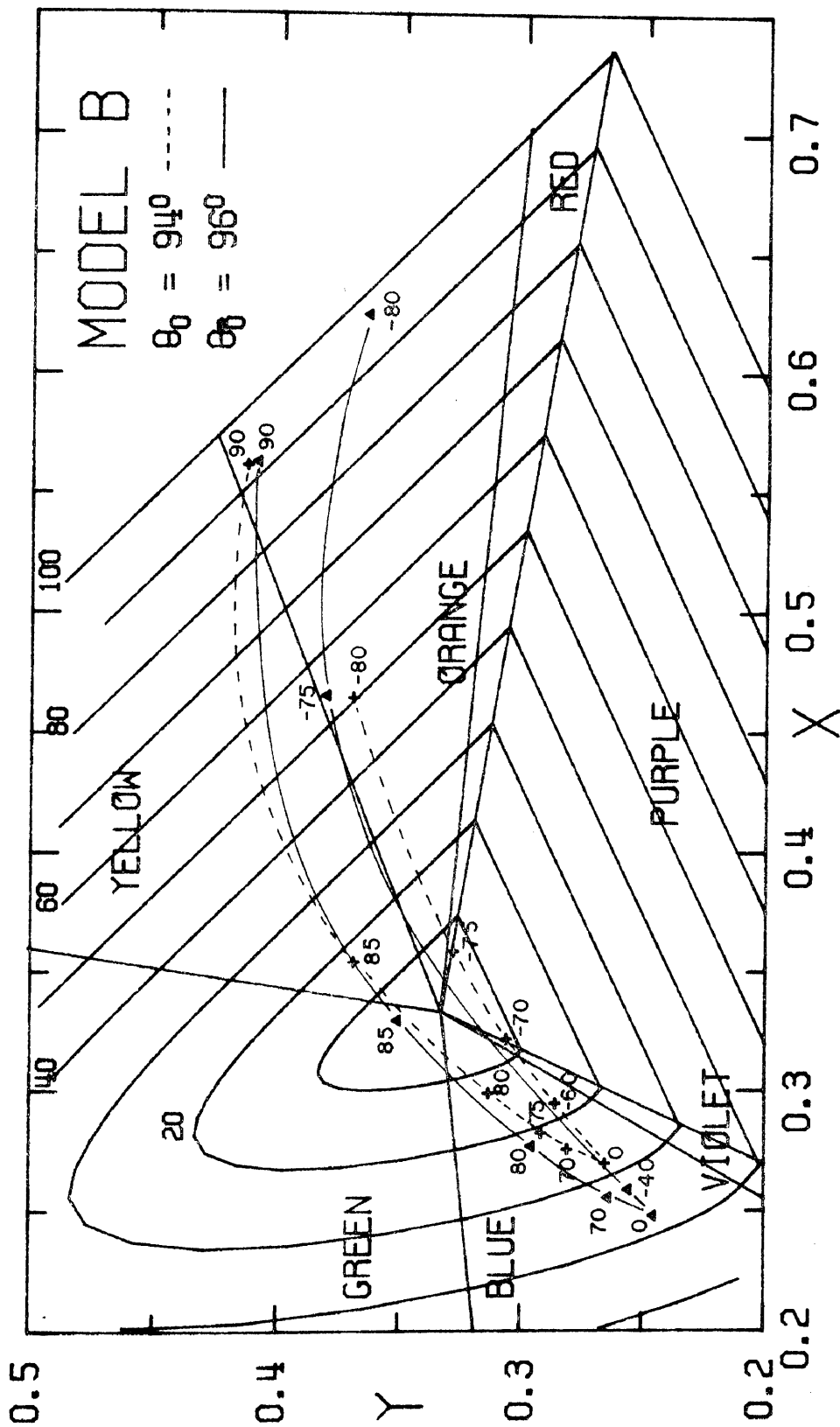


Figure 47 - Chromaticity diagram for Model B and $\theta_0=94^\circ$ and 96°

This results from the ozone absorption by the Chappius bands in the vicinity of $\lambda=0.6\mu$. The spectral purity of the zenith increases as θ_0 increases from 92° to 96° . A portion of the sky is purple of a low spectral purity in the antisolar half plane in some of these cases. The chromaticity coordinates very hardly at all near the zenith as θ changes. The actual turning point of the chromaticity curve occurs in the range from $\theta = 20$ to 30° for $\theta_0 = 94^\circ$ and 96° . The turning point on the figures has usually been marked 0° , since the chromaticity is the same at $\theta = 0^\circ$ and 30° on these figures.

The blue color of the zenith sky as well as a region of purple sky in the antisolar half plane are features which are obtained from this model which cannot be explained by a purely Rayleigh scattering atmosphere.

c) Model C. Molecular atmosphere, ozone, normal aerosol amount.

The results for this model of the normal atmosphere are shown in Figures 48 and 49. The blue region of the sky around the zenith has a higher spectral purity when aerosols are added to the model. Dave and Mateer (1968) have pointed out that a normal aerosol amount contributes to an increased blueness of the zenith sky. The spectral purity is somewhat higher in our calculations than in theirs and becomes almost 40% near the zenith when $\theta_0 = 96^\circ$. The greater increase in absorption at blue than at red wavelengths for the solar radiation up to the scattering point

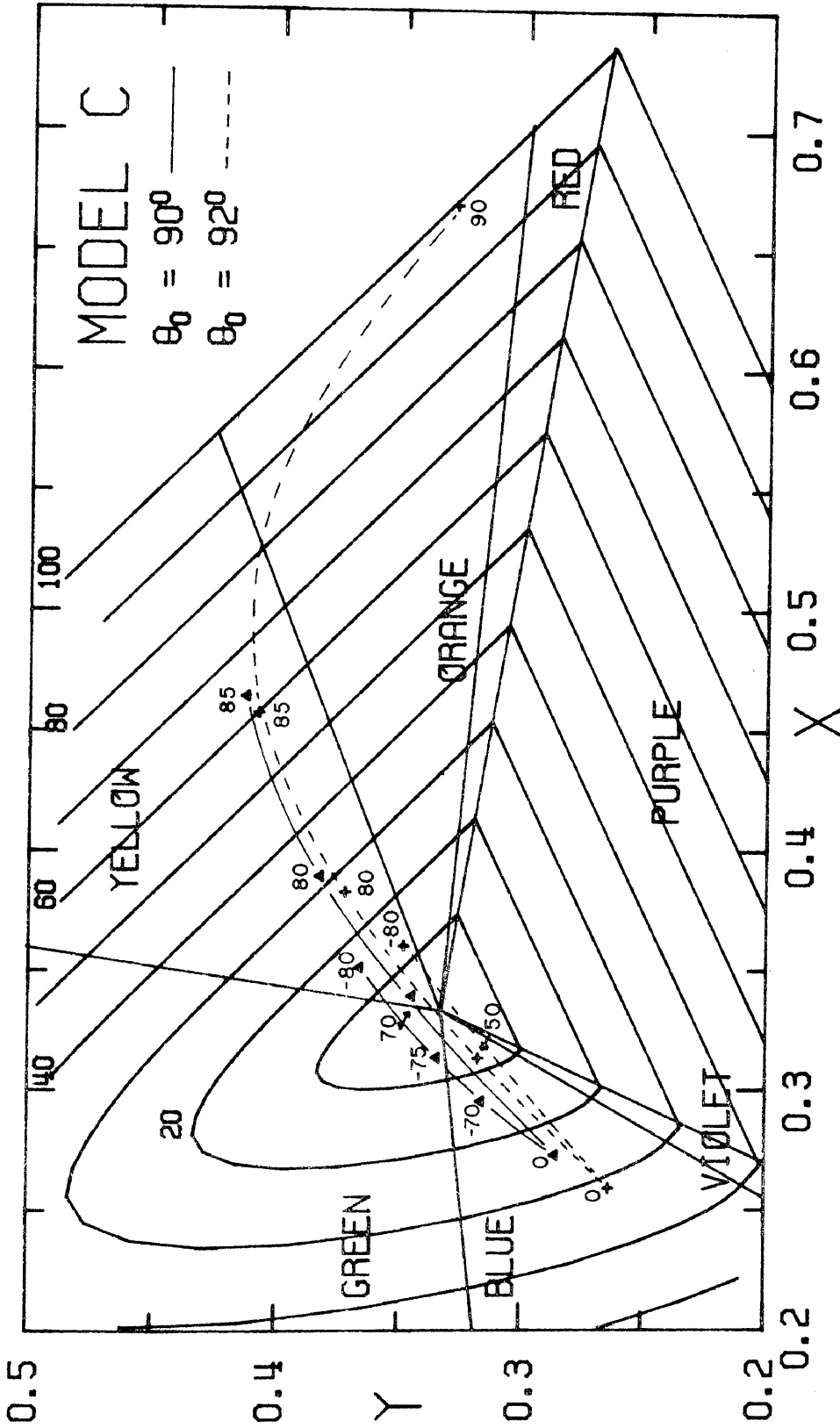
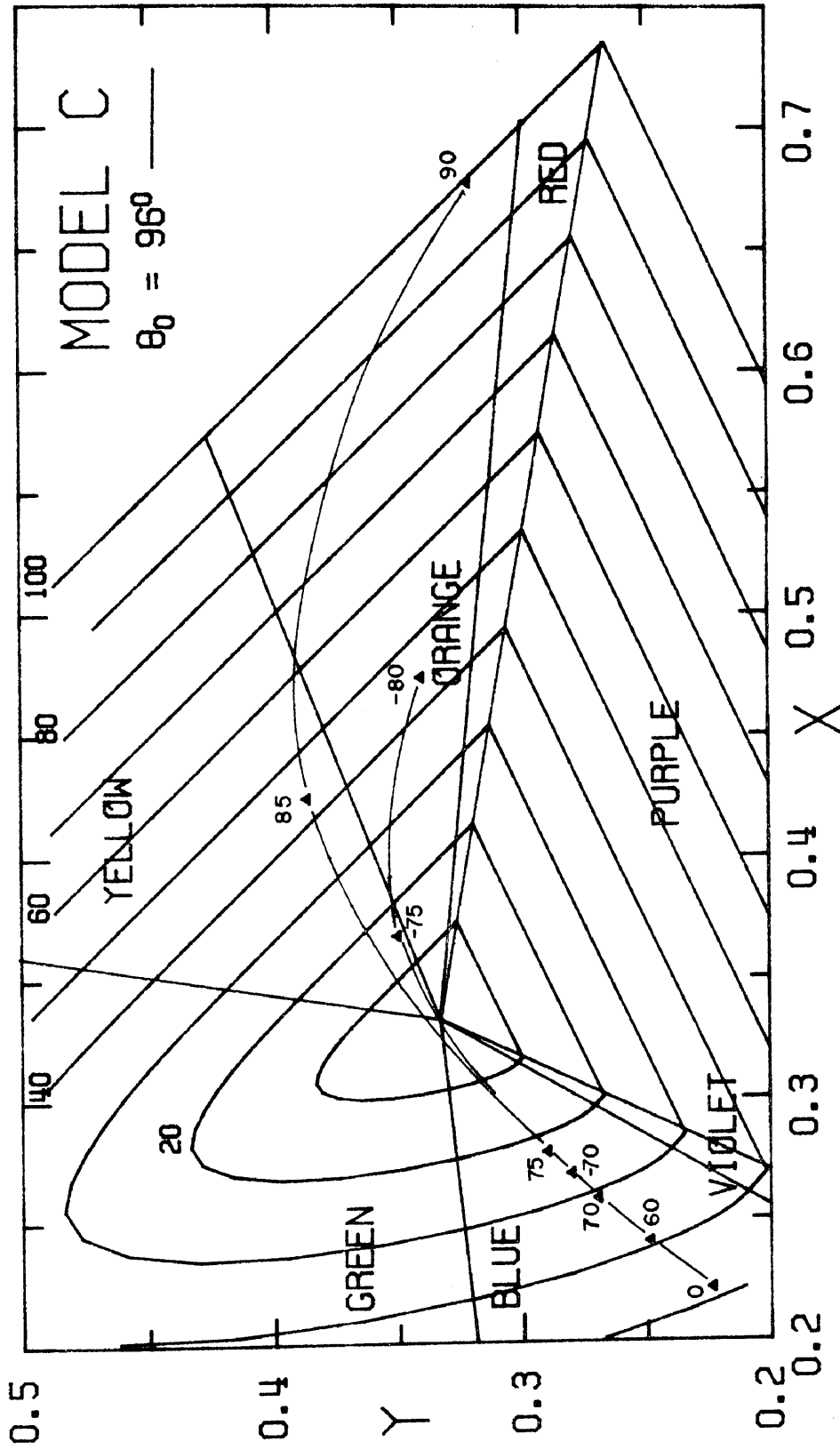


Figure 48 - Chromaticity diagram for Model C and $\theta_0=90^\circ$ and 92°

Figure 49 - Chromaticity diagram for Model C and $\theta_0=96^\circ$

when Models B and C are compared (Figures 33 and 34) is the reason for the deeper blue color at the zenith when aerosols are present. Some purple light of low spectral purity is predicted for some angles of observation.

The color of the sky around the solar horizon is correctly predicted as an orange-red of high spectral purity. The single scattering model predicts orange colors near the antisolar horizon as Θ_0 increases in disagreement with observation. Obviously multiple scattering effects are most important in this region of the sky. The chromaticity curve for $\Theta_0 = 94^\circ$ is not shown here since it is very nearly the same as for $\Theta_0 = 96^\circ$. The main difference is that the point $\Theta = 80^\circ$ corresponds to a yellow-orange of spectral purity 18% when $\Theta_0 = 94^\circ$, but corresponds to a nearly white color when $\Theta_0 = 96^\circ$.

d) Model D. Molecular atmosphere, ozone, three times normal aerosol amount.

The chromaticity diagram when the atmosphere contains three times the normal aerosol amount at all altitudes is shown in Figure 50. At $\Theta_0 = 92^\circ$ the portion of the sky near the solar horizon has a higher spectral purity and tends to appear a deeper red with the greater aerosol amount. The additional aerosols also make the sky around the zenith a blue of greater spectral purity and this color extends over a larger region of the sky. The more vivid colors which are observed at twilight during periods of high

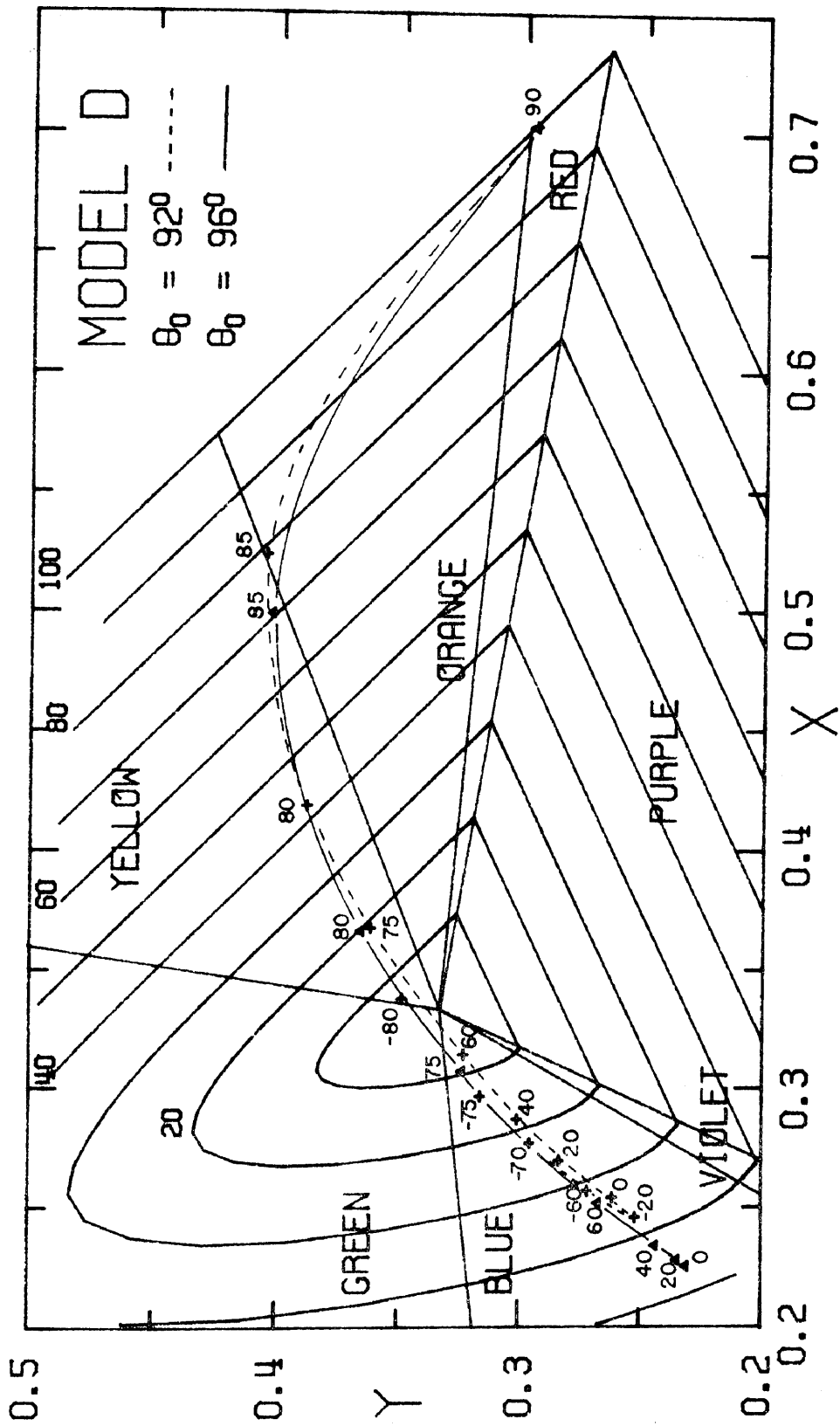


Figure 50 - Chromaticity diagram for Model D and $\theta_0=92^\circ$ and 96°

aerosol concentration in the atmosphere are confirmed by this model.

e) Model E. Molecular atmosphere, ozone, ten times normal aerosol amount.

The chromaticity diagram when the atmosphere contains ten times the normal aerosol amount at all altitudes is shown in Figure 51. This model represents an extreme condition with the optical thickness of the atmosphere in a vertical direction between 2 and 3.5 (Figure 31). The region of the sky around the solar horizon with red and orange colors of high spectral purity continues to expand as the aerosol concentration increases up to this amount. For example, at $\Theta_0 = 92^\circ$ the spectral purity is greater than 20% from the solar horizon to $\Theta \sim 55^\circ$ for Model E; the corresponding values of Θ for Models C and D are 78° and 76° . Furthermore the deep blue sky near the zenith has disappeared in Model E which has only a gray blue region within 30° of the zenith. These same features are also evident at $\Theta_0 = 92^\circ$. For large aerosol amounts the model indicates vivid colors near the solar horizon, but colors of reduced spectral purity near the zenith. Multiple scattering effects would be especially important for the larger optical depths of this model.

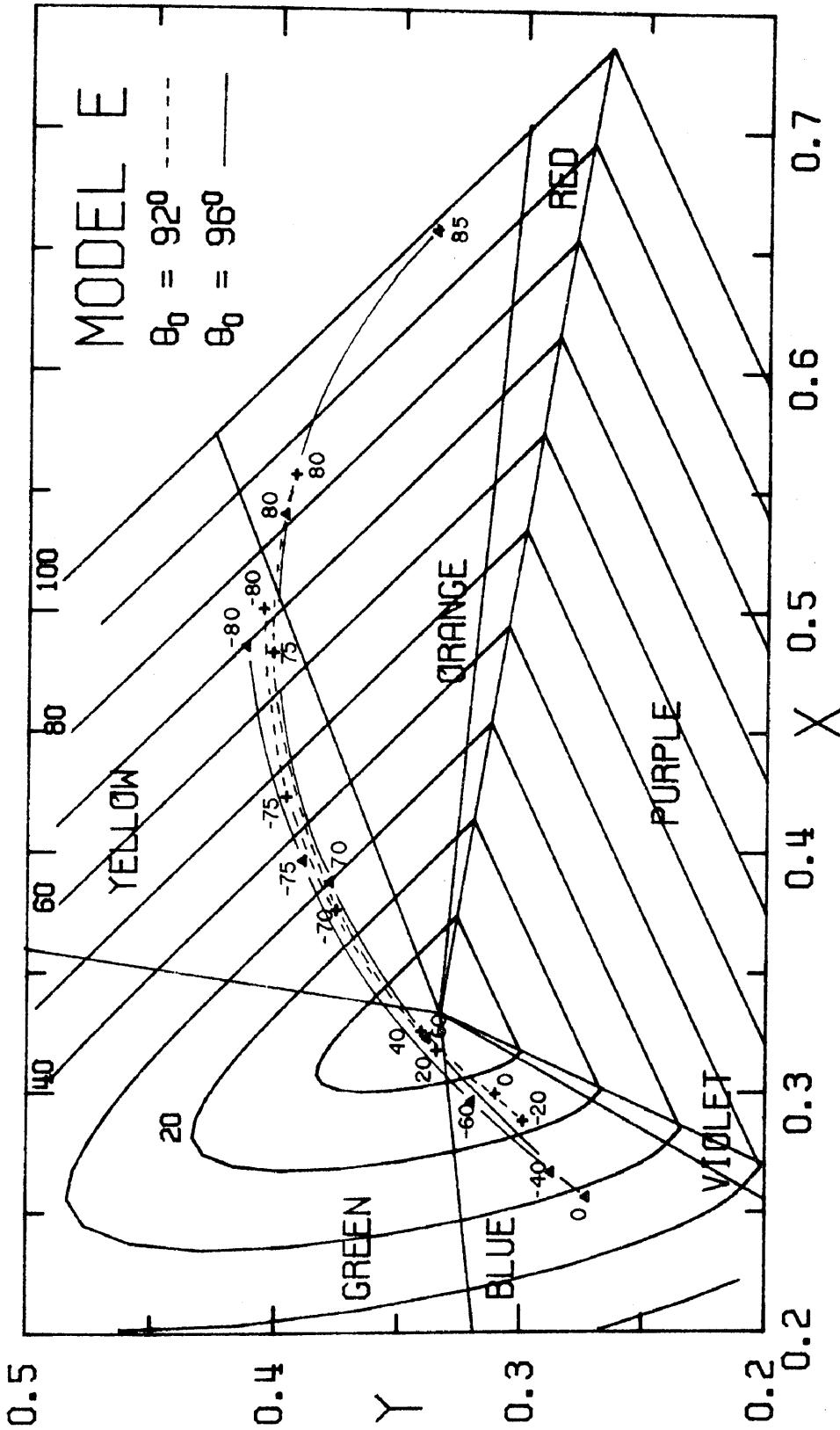


Figure 51 - Chromaticity diagram for Model E and $\theta_0=92^\circ$ and 96°

XIII. CONCLUSIONS

Molecular scattering alone cannot explain the colors of the twilight sky. The addition of ozone absorption is essential to a model in order to reproduce the blue of the zenith sky. Some purple colors of low spectral purity are also obtained from this mode. The deep blue of the zenith sky and the red and orange colors of high spectral purity in the region of the sky around the solar horizon are obtained only when a realistic model is used which combines molecular and aerosol scattering and ozone absorption. When the aerosol amount is three times normal the blue of the zenith sky becomes deeper and extends over a greater area. However, when the aerosol amount is ten times normal the spectral purity of the blue of the zenith sky decreases appreciably. Larger regions of red and yellow colors of higher spectral purity around the solar horizon are predicted when the aerosol amount is greater than normal.

Refraction effects have been included in the present calculations. The greatest limitation of the present results is that they include only single scattering effects. The use of Monte Carlo techniques to extend these results to include all orders of multiple scattering should be attempted in order to extend the theoretical calculations further.

BIBLIOGRAPHY

Adams, C. N. and Kattawar, G. W. 1970, J. Quant. Spect. Rad. Trans. 10, 341.

Anonymous, 1965: Handbook of Geophysics and Space Environments, United States Air Force, 653 pp.

Coffeen, D. L. and Gehrels, T. 1969, Astron. J. 74, 433 (Paper XV).

Coffeen, D. L. 1969, Astron. J. 74, 466 (Paper XVI).

Dave, J. V. and Mateer 1968, J. Geophy. Res. 73, 6897.

Deirmendjian, D. 1964, Appl. Opt. 3, 187.

Dollfus, A. 1955, Thesis, University of Paris.

_____, 1966 "Contribution au colloque Caltech-JPL sur la Lune".

Elterman, L. 1968, UV, Visible, and IR Attenuation for Altitudes to 50 km, 1968, AFCRL-68-0153, United States Air Force, 49 pp.

Goody, R. 1973, J. Atmos. Sci. 20, 502.

Hansen, J. H. and Arking, A. 1971, Science 171, 669.

Holland, A. C. and Gague, G. 1970, Appl. Opt. 9, 1113.

Hulburt, E. O. 1953, J. Opt. Soc. Amer. 43, 113.

Irvine, W. M. 1968, J. Atmos. Sci. 25, 610.

Johnson, F. S. 1968, J. Atmos. Sci. 25, 658.

Kattawar, G. W. and Plass, G. N. 1967a, Appl. Opt. 6, 1377.

_____, 1967b, Appl. Opt. 6, 1549.

_____, 1968, Appl. Opt. 7, 1519.

_____, 1971, Appl. Opt. 10, 74.

Kattawar, G. W. and Adams, C. N. 1971, Ap. J. 167, 183.

Knuckles, C. F., Sinton, M. F., and Sinton, W. M. 1961, Lowell Obs. Bull., No. 115, 153.

Kuiper, G. P. 1969, Comm. LPL, Nos. 100-104, 229.

Lyot, B. 1929, Ann. Obs. Mendon 8, 1 (NASA-TTF-187).

McLeod, A. R. 1919, Phil. Mag. 38, 546.

Plass, G. N. and Kattawar, G. W. 1969, Appl. Opt. 8, 2489.

_____, 1970, Appl. Opt. 9, 1122.

_____, 1971, Appl. Opt. 10, 1172.

Rozenberg, G. V. 1963, Twilight: A Study in Atmospheric Optics, State Press for Physicomathematical Literature, Moscow; translated by R. G. Rodman, Plenum Press, New York, 358 pp.

Thekaekara, M. P. 1972, Opt. Spectra 5, 32.

Wyszecki, G., and W. S. Stiles 1967, Color Science: Concepts and Methods, J. Wiley, New York, 628 pp.